Technical University of Munich

TUM School of Medicine and Health

Engineering vascular structures on-chip and within β-cell tissue cultures

Caroline Remmert

Complete reprint of the dissertation approved by the TUM School of Medicine and Health of the Technical University of Munich for the award of the

Doktorin der Naturwissenschaft (Dr. rer. nat).

Chair: Prof. Dr. Maximilian Reichert

Examiners:

1. Prof. Dr. Matthias Meier
2. Prof. Dr. Johannes Beckers
3. Prof. Dr. Manfred Claassen

The dissertation was submitted to the Technical University of Munich on 2 May 2024

and accepted by the TUM School of Medicine and Health on 9 October 2024.

Engineering vascular structures on-chip and within β-cell tissue cultures

Caroline Remmert

Supervisor: Prof. Dr. Matthias Meier

Publications

During the doctoral studies, the following papers have been published:

[1] Maren Marder[$], **Caroline Remmert[$]**, Julius A. Perschel, Munkhtur Otgonbayar, Christine von Toerne, Stefanie Hauck, Judith Bushe, Annette Feuchtinger, Bilal Sheikh, Michel Moussus, Matthias Meier: Stem Cell-Derived Vessels-on-Chip for Cardiovascular Disease Modeling. Cell Reports (2024), CELREP_114008, DOI: 10.1016/j.celrep.2024.114008

[2] Simon Rosowski[$], **Caroline Remmert**, Maren Marder, Misao Akishiba, Judith Bushe, Annette Feuchtinger, Alina Platen, Siegfried Ussar, Fabian Theis, Sandra Wiedenmann, Matthias Meier: Single-cell characterization of neovascularization using hiPSC-derived endothelial cells in a 3D microenvironment. Stem Cell Reports (2023). DOI: 10.1016/j.stemcr.2023.08.008

[3] **Caroline Remmert[$]**, Nicole Rogers, Sandra Wiedenmann, Henrik Semb, Heiko Lickert, Matthias Meier: Single-cell resolved cell communication between stem cell-derived vessels and islets. The manuscript is in preparation and is to be submitted.

[4] **Caroline Remmert[$]**, Munkhtur Otgonbayar[$], Maren Marder, Julius Perschel, Matthias Meier: Generation of stem cell-derived vessels-on-chip. Invited publication to Cell STAR Protocols. The manuscript is in preparation and will be submitted.

$ First author

All published paragraphs and own contributions are indicated at the beginning of each chapter.

Zusammenfassung

Endothelzellen (ECs) sind wichtige Bestandteile der Blutgefäße und ihre funktionelle Integrität ist für die Aufrechterhaltung der kardiovaskulären Homöostase und der Organfunktion von wesentlicher Bedeutung. So trägt die Beeinträchtigung der Endothelfunktion wesentlich zu pathophysiologischen Zuständen wie Atherosklerose, Diabetes und Adipositas bei. Um vaskuläre Dysfunktionen bei kardiovaskulären Erkrankungen (CVD) früher zu erkennen, ist es daher von zentraler Bedeutung, die Entwicklung, Anpassung und Reaktion von ECs auf Mikroumweltfaktoren besser zu verstehen. In diesem Zusammenhang können aus Stammzellen gewonnene *in-vitro*-Gewebsmodelle dazu beitragen, patientenspezifische Hintergründe zu rekapitulieren, das komplexe menschliche Gefäßsystem zu modellieren, die gewebespezifische Anpassung zu untersuchen und die frühe Entwicklung von CVD zu entschlüsseln. Da der Blutfluss für die Funktionalität von ECs wichtig ist, haben sich Organ-on-Chip-Systeme (OoC) als Schlüsseltechnologie erwiesen, um die physiologischen Bedingungen der Gefäße besser nachzubilden. Darüber hinaus können *in-vitro*-Modelle dazu beitragen, die Funktion des Gefäßsystems in der Bauchspeicheldrüse besser zu verstehen. Insbesondere die endokrinen Inseln sind stark vaskularisierte Organe, deren Funktionalität durch die Interaktion mit ECs beeinflusst wird, und eine endotheliale Dysfunktion steht in engem Zusammenhang mit der β-Zell-Dysfunktion bei Diabetes. Angesichts des weltweiten Anstiegs der Diabetesinzidenz besteht die Notwendigkeit, die Krankheit besser zu verstehen und die Behandlungsmöglichkeiten zu verbessern. Hier können aus Stammzellen abgeleitete Modellsysteme zu einem besseren Verständnis der β-Zell- und EC-Dysfunktion beitragen, Zell-Zell-Interaktionen aufdecken, die für die Inselfunktion wichtig sind, und neue therapeutische Maßnahmen wie die Transplantation von aus Stammzellen abgeleiteten Inselzellen (SC-ILC) ermöglichen. Insbesondere für die SC-ILC-Transplantation ist die Vaskularisierung ein aktueller Forschungsschwerpunkt, um die Reifung und Funktion der SC-ILC sowie das Überleben des Transplantats zu verbessern.

Diese Doktorarbeit umfasst drei miteinander verbundene Projekte, die sich auf die Untersuchung der Biologie von Inselzellen und Endothelzellen konzentrieren.

Die erste Studie konzentrierte sich auf die Entwicklung eines Blutgefäß-auf-Chip-Modells, welches eine multi-omische Analyse von Gefäßen in gesundem Zustand und unter metabolischem Stress ermöglicht. Der Chip ermöglichte die Kultivierung von hiPSC-generierten Endothelzellen (SC-ECs) in einem organotypischen Mikrokanal unter Schwerkraft-induziertem Scherstress. Ein Atherosklerosemodell wurde als Modell für endotheliale Dysfunktion entwickelt. Das Modell zeigte früh einsetzende

Atherosklerosemerkmale und deutliche Veränderungen im Proteom und Sekretom als Reaktion auf metabolischen Stress. Der Gefäßchip bietet eine umfassende Plattform zur Untersuchung der endothelialen Entwicklung und Fehlfunktion mit kleinem Probenvolumen und in hoher Auflösung.

Im zweiten Projekt wurde ein *in vitro*-Verkapselungsmodell für die Vaskularisierung von SC-ILC entwickelt, das die Mikroumgebung der Inseln nachahmt. In diesem Modell zeigten von Stammzellen abgeleitete β (SC-β) -Zellen eine erhöhte Insulinsekretion und SC-α-Zellen, der Glukagon produzierende Zelltyp der Inseln, eine verbesserte funktionelle Reifung. Einzelzell-RNA-Sequenzierung und die darauf aufbauende Analyse der Zell-Zell-Kommunikation zeigten spezifische und direkte Interaktionen zwischen SC-ECs und endokrinen Zellen, die die SC-ILC-Reifung und -Funktion beeinflussten. In Zukunft könnte das Modell dazu verwendet werden, physiologisch relevantere *in vitro*-Modelle für die Diabetesforschung zu entwickeln und dazu beizutragen, Diabetesstudien im Tierversuch zu reduzieren.

Im dritten Projekt wurde die Impedanzspektroskopie eingesetzt, um die Funktionalität der SC-ILC, gemessen an ihrer Fähigkeit Insulin zu sekretieren, zu untersuchen. Ein Mikrokavitäten-Array-Chip (MCA) ermöglichte die gleichzeitige Überwachung mehrerer SC-ILCs und bot eine schnelle, nicht-invasive Alternative zur herkömmlichen ELISA-Analyse (enzyme-linked immunosorbent assay). Diese Methode erwies sich beim Screening einzelner SC-ILCs als effektiv und zeigte ihr Potenzial für die Hochdurchsatzanalyse von *in vitro* erzeugten Inseln. Die verwendete Methode hat daher die Möglichkeit die Entwicklung von Medikamenten, die Diabetesforschung und die Therapie voranzutreiben.

Zusammenfassend werden in dieser Dissertation Ansätze für die Diabetes- und Endothelforschung vorgestellt, die eine Grundlage für die Entwicklung vaskularisierter menschlicher OoC-Plattformen, *in vitro*-Modelle für die Vaskularisierung von SC-ILC und das funktionelle Screening von SC-ILC bilden. Diese Fortschritte werden dazu beitragen, den Einsatz von Tieren in der Forschung zu reduzieren und wertvolle Erkenntnisse für die personalisierte Medizin und therapeutische Interventionen bei Diabetes zu liefern.

Abstract

Endothelial cells (ECs) are important components of blood vessels, and their functional integrity is essential for maintaining cardiovascular homeostasis and organ function. The impairment of endothelial function is a crucial contributor to various pathophysiological conditions, including atherosclerosis, diabetes, and obesity. Understanding EC development, adaption, and response to microenvironmental cues is, therefore, of central importance to reveal early vascular dysfunction in cardiovascular diseases (CVD). In this regard, stem cell-derived *in vitro* tissue models can help to recapitulate patient-specific backgrounds, model the complex human vascular system, investigate tissue-specific toning, and decipher the early development of CVD. As blood flow is important for EC functionality, organ-on-chip (OoC) systems have emerged as a key technology to better mimic the physiological conditions of vessels. Additionally, *in vitro* models can help to improve our understanding of the vascular system's role in the pancreas. Especially endocrine islets are highly vascularized organs, the interaction with ECs influences the islet´s functionality, and endothelial dysfunction is strongly associated with β-cell dysfunction in diabetes. With the global increase in diabetes incidences, there is a need to understand the disease better, detect disease onset, and advance treatment options. Here, stem cell-derived model systems can contribute to a better understanding of β-cell- and EC-dysfunction, reveal cell-cell interactions that are important for islet function, and develop new therapeutic interventions such as stem cell-derived islet (SC-ILC) transplantation. Especially for SC-ILC transplantation, vascularization is a current focus of research to enhance SC-ILC maturation, function, and graft survival.

This doctoral thesis comprises three interconnected projects focusing on islet and endothelial cell biology.

The first study focused on the development of a microfluidic vascular chip platform that allowed multi-omics analysis of vessels in a healthy state and under metabolic stress. The chip enabled the culture of hiPSC-derived endothelial cells (SC-ECs) in an organotypic microchannel under gravity-induced shear stress. An atherosclerosis model was developed as a model for endothelial dysfunction. The model showed early-onset atherosclerosis features and distinct changes in the proteome and secretome in response to metabolic stress. The vascular chip provides a comprehensive platform for studying endothelial development and dysfunction at a high resolution and single-cell level.

The second project introduced an *in vitro* encapsulation model for the vascularization of SC-ILC mimicking the islet microenvironment. In this model, stem cell-derived β-cells (SC-β) showed increased insulin secretion, and SC-α-cells, the islet´s glucagon-producing cell type,

showed enhanced functional maturation. Single-cell RNA sequencing and analysis of cell-cell communication revealed specific and direct interactions between SC-ECs and endocrine cells that affected SC-ILC maturation and function. In the future, the model could be used to generate more physiologically relevant *in vitro* models for diabetes research and help to reduce diabetes studies within animals.

In the third project, impedance spectroscopy was used to screen SC-ILC functionality as measured by their ability to secrete insulin. A microcavity array (MCA) chip enabled the simultaneous monitoring of multiple SC-ILCs and provided a rapid, non-invasive alternative to conventional enzyme-linked immunosorbent assay (ELISA) analysis. This method proved effective in screening single SC-ILCs and showed its potential for high-throughput analysis of *in vitro* generated islets, advancing drug development, diabetes research, and therapy.

In summary, this doctoral thesis presents approaches for diabetes and endothelial research that provide a basis for the development of vascularized human OoC platforms, *in vitro* models for SC-ILC vascularization, and functional screening of SC-ILC. These advances will help reduce the use of animals in research and provide valuable insights for personalized medicine and therapeutic interventions in diabetes.

Acknowledgment

I would like to thank the following people without whom I would not have been able to complete this work.

First of all, I want to thank my first supervisor Prof. Dr. Matthias Meier for giving me the opportunity to study islet and endothelial biology and follow my interest in tissue engineering and organ-on-chip development. Many thanks for the interesting scientific discussions, the good working atmosphere in which I was allowed to grow and enjoyed working scientifically, and the advancement of projects when I would have stopped. Thanks also go to my second supervisor, Prof. Dr. Johannes Beckers, for being my supervisor at TUM and for the fruitful discussions during my TAC meetings. A special thanks to Dr. Rosalia Fernández-Alonso for being my mentor and supporting me with regular meetings, especially in the first years of my doctoral studies. Your input and time meant a lot to me.

A special thanks goes to my colleagues at the AG Meier. Thanks for your support, encouragement, and friendship throughout the past years! You made every down a bit better and every up worth celebrating. Thanks to Julius and Daniel for being my boulder and climbing buddies. Thanks to the LumenCrew, Julius, Maren, and Munkhtur, for doing science and friendship together. Thanks to Johannes, Daniel, and Sandra for all the single-cell support and for helping me through the jungle of Python coding. A very special thanks goes to Maren alias “Maro and Caren”. Working with you has always been fun, and I enjoyed every discussion and LumenChip experiment we have conducted in the past few years! I would also like to thank Nina, Johannes, and Julius for climbing various mountains together and for culinary excursions in the Munich city center. Thanks to Nina for the discussions during my hospitation, which convinced me to do my doctoral thesis at AG Meier. Many thanks also to Nina and Sandra for proofreading my thesis, which helped me a lot! Thanks to Alina for all the support in the lab and to Giannis for the support with single-cell sequencing and 10x. Thanks also to Nicole for doing the SC-ILC differentiation, the nice cooperation, and the good lab floor talks. To this end, I also want to thank Prof. Dr. Heiko Lickert and Prof. Dr. Henrik Semb for the cooperation in the eIslet project. A warm thank you also to the HPC admin team and colleagues at the HPC for all the support and the nice scientific community I was allowed to grow in.

Most importantly, I want to thank my husband, Michi. Thank you for your encouragement and support throughout this journey. Thanks for believing in me and my research ideas, for every hug after a long, exhausting day, and for every celebration when an experiment worked out.

You have given me the necessary self-confidence and the courage to continue and enjoy what I do. I love you, and I´m excited about every journey that comes next for us.

Besonders möchte ich auch meiner Familie danken. Allen voran meinen Eltern. Danke, dass ihr mich immer in allem unterstützt, mich darin ermutigt habt eine Doktorarbeit zu machen, immer ein offenes Ohr für mich habt und versucht meine Forschungsprobleme und -erfolge zu verstehen, auch wenn es schwerfällt. Danke an meine Brüder, Fabian und Tim, für alle Unterstützung und Diskussionen. Danke Fabi, für das Teilen derselben wissenschaftlichen Leidenschaft und kritischen Nachfragen, die mir geholfen haben einen anderen Blick auf meine Daten zu werfen. Danke Tim, für dein Interesse an dem was ich tue und dein Zuhören. Danke auch an meine Oma und Opas, die mit mir auf meine Verteidigung hin fiebern oder mit mir mitleiden, wenn Forschungsdaten durch eine Cyberattacke verschwinden. Ich habe euch alle unfassbar lieb und bin stolz euch meine Familie nennen zu dürfen!

Table of Content

Publications I
Zusammenfassung II
Abstract IV
Acknowledgment VI
Table of Content VIII
Figure Directory XI
Extended Data Figure Directory XII
Abbreviations XIII
1 Scientific context 1
1.1 The vascular system 1
1.1.1 Vascular endothelial cell biology 1
1.1.2 Atherosclerosis 2
1.2 *In vitro* models for vascular research 3
1.2.1 From 2D to 3D cell cultures 3
1.2.2 2D and 3D cell culture models for vascular research 4
1.2.3 Organ-on-Chip technology 5
1.2.4 Organ-on-Chip systems for vascular research 6
1.3 Diabetes mellitus and pancreas biology 8
1.3.1 Pancreas biology 8
1.3.2 The islet of Langerhans 9
1.3.3 The islet endothelial cell 10
1.3.4 Diabetes mellitus 11
1.3.5 Stem cell-derived islets for cell replacement therapy for diabetes 12
1.3.6 Vascularization approaches for pancreatic islets 14
1.4 Methodic background – characterization of *in vitro* models 16
1.4.1 Monitoring of 3D cultures with impedance spectroscopy 17
1.4.2 Testing β-cell functionality 18
1.4.3 Single-cell RNA sequencing for transcriptome analysis 18
1.4.4 Mass spectrometry for the analysis of proteome and secretome 19
1.4.5 Immunofluorescence staining 19
1.5 Methodic background – 3D printing for microfluidic chip production 20
2 Aims of the thesis 21
2.1 Thesis background 21
2.2 Aims of the thesis 21
2.3 Structure of the thesis 23

3 Stem Cell-Derived Vessels-on-Chip for Cardiovascular Disease Modeling 24
3.1 Declaration of contribution 24
3.2 Introduction 24
3.3 Material and Methods 27
Generation and cultivation of SC-ECs 27
Chip manufacturing 27
Flow characterization 28
Cell seeding on chip 28
Whole mount immunofluorescence staining 29
Histology of lumen sections 30
Confocal imaging 30
Permeability analysis 30
Branching characterization and branch density analysis 31
Live dead cell analysis 31
NO assay 31
Sample preparation for single-cell RNA sequencing (scRNAseq) 32
Pre-processing of scRNAseq data 32
Clustering and cell type annotation 32
RNA velocity using basic modelling 32
Cell treatment for oxidative stress induction 33
Sample preparation and mass spectrometry measurements 33
Data processing - protein identification 34
Data processing - label-free quantification 34
Data analysis 34
Oxidative stress compound staining 35
Quantification and statistical analysis 35
3.4 Results 36
Design and characterization of the open organ-on-chip platform 36
Formation of the functional perfused endothelial vessel on chip 39
Single-cell transcriptomic and functional analysis of the SC-EC on-chip 41
Interfacing the vessel-on-chip platform for downstream analysis 45
Modeling the early-onset of atherosclerosis by oxidative stress under in vitro conditions on-chip 46
3.5 Discussion 51
3.6 Extended Data 54
4 Vascularization of stem cell-derived β-cells for diabetes research 55
4.1 Declaration of contribution 55
4.2 Introduction 55

4.3 Material and Methods ... 58
Resource table ... 58
HiPSC culture ... 58
Differentiation of stem cell-derived β-cells from hiPSCs and cell culture procedures ... 59
Generation of a vascularization model for SC-ILC ... 60
Hormone secretion assay ... 61
Microscopy and immunofluorescence ... 61
Whole mount immunofluorescence staining ... 63
Sample preparation for single-cell RNA sequencing ... 63
Pre-processing of scRNAseq data ... 63
Clustering and cell type annotation ... 63
Velocity analysis of the scRNAseq data ... 64
Pathway analysis ... 64
CellChat analysis ... 65
Statistical methods ... 65
4.4 Results ... 66
Formation of vascularized SC-ILC using a self-organized culture ... 66
vCo-culture leads to a transcriptomic change in the SC-α-cell population ... 68
Cell communication analysis reveals interaction pathways of SC-ECs & endocrine cells 72
Subtypes of SC-ECs from the vCo-culture express islet-EC-specific genes ... 76
SC-α-cells from the vCo-culture show increased sensitivity in glucagon secretion ... 79
4.5 Discussion ... 81
4.6 Extended Data ... 85
5 Direct monitoring of insulin secretion in stem cell-derived β-cells by impedance spectroscopy ... 90
5.1 Declaration of contribution ... 90
5.2 Introduction ... 90
5.3 Materials and Methods ... 92
Differentiation and culture of stem-cell derived β-cells ... 92
Microcavity fabrication ... 92
Hormone secretion assay measured with impedance spectroscopy. ... 92
Microscopy and immunofluorescence ... 93
5.4 Results ... 94
Impedimetric analysis allows monitoring of insulin secretion by stem-cell derived β-cells 94
Impedimetric screening of SC-ILC response to Ca^{2+}-influx inhibitor diazoxide ... 96
5.5 Discussion ... 98
6 Conclusion and Outlook ... 100
7 References ... 104

Figure Directory

Figure 1 | Artery vessel in health and after atherosclerosis progression. 3
Figure 2 | Organ-on-chip systems for vascular research 7
Figure 3 | Pancreas anatomy and development 9
Figure 4 | Human Islets of Langerhans *in vivo* compared to stem cell-derived islets *in vitro* 14
Figure 5 | Approaches for islet vascularization. 16
Figure 6 | The open microfluidic chip platform for organotypic cell cultures.. 38
Figure 7 | Formation of a functional perfused endothelial vessel on-chip displaying barrier integrity and sprouting angiogenesis 40
Figure 8 | Single-cell transcriptomics reveal specified flow-induced cell clusters reflected by enhanced nitric oxide synthesis in *in vitro* conditions 44
Figure 9 | Whole mount and paraffin-section immunofluorescence stainings allow for detailed morphological analysis of endothelial tissue 46
Figure 10 | Oxidative stress induction of vessel formed on-chip 49
Figure 11 | Secretome analysis of oxLDL and FFA treated SC-ECs on-chip 50
Figure 12 | Establishment of a stem-cell derived vascularization model of β-cells that enables increase in insulin secretion 67
Figure 13 | Single-cell transcriptomic analysis of vCo-culture shows a transcriptomic change in the α-cell population 71
Figure 14 | Subcluster of SC-β- and SC-α-cells indicates SC-α-cell maturation in vCo- and Co-culture. 72
Figure 15 | Cell communication analysis reveals SC-EC to endocrine-specific signaling pathways 75
Figure 16 | SC-ECs express EC-islet-specific genes in the vCo-culture.. 78
Figure 17 | Alpha cells from the vCo- and Co-culture show increased sensitivity in glucagon secretion. 80
Figure 18 | Microcavity array for impedance analysis of stem-cell derived β-cells 95
Figure 19 | Glucose stimulated insulin secretion assay measured by impedance spectroscopy 96
Figure 20 | Determination of SC-ILC response to Ca^{2+}-influx inhibitor diazoxide 97

Extended Data Figure Directory

Extended Data Figure 1 | Optimization of culture conditions and characterization of vCo-culture 85
Extended Data Figure 2 | Quality control of the single-cell RNA sequencing data of integrated vCo-culture and SC-ILC dataset. 86
Extended Data Figure 3 | Characterization of the vCo-culture by single-cell RNA sequencing (scRNAseq) 87
Extended Data Figure 4 | Cell-cell communication analysis reveals differences in vCo- and Co-culture signaling 88
Extended Data Figure 5 | Cell-cell communication marker expressed in vCo- and Co-culture 89

Abbreviations

2D	Two-Dimensional
3D	Three-Dimensional
ACKR3	Atypical Chemokine Receptor 3
ADGRG1	Adhesion G Protein-Coupled Receptor G1
ADP	Adenosine diphosphate
ANGPT	Angiopoietin
APO	Apolipoprotein
ARP	Actin Related Protein
ARX	Aristaless-Related Homeobox
ATP	Adenosine triphosphate
BMP	Bone morphogenic protein
BSA	Bovine Serum Albumin
CALCR	Calcitonin Receptor
CALM1	Calmodulin 1
CAMK2D	Calcium/Calmodulin Dependent Protein Kinase II Delta
CAV1	Caveolin 1
CDC42	Cell division control protein 42 homolog
CDH1	E-Cadherin
cDNA	Complementary deoxyribonucleic acid
CFTR	CF Transmembrane Conductance Regulator
CHGA	Chromogranin A
CI	Confidence Interval
CLDN	Claudin
COL1	Collagen Type 1
CPA1	Carboxypeptidase A1
CTGF	Connective tissue growth factor
CVD	Cardiovascular Disease
CYBG	Cytoglobin
DAPI	4´,6-Diamidino-2-Phenylindole
DDA	Data-dependent acquisition
DE	Definitive Endoderm
DEG	Differential Expressed Genes
DEP	Differential Expressed Proteins

DLK1	Delta-like 1 homolog
DLL4	Delta Like canonical notch Ligand 4
DPP4	Dipeptidyl Peptidase 4
EC	Endothelial Cells
ECM	Extracellular Matrix
EDN	Endothelin
EGF	Epidermal Growth Factor
ELISA	Enzyme-Linked Immunosorbent Assay
ENO1	Enolase 1
EP	Endocrine Progenitors
ER	Endoplasmic Reticulum
ERO1B	Endoplasmic Reticulum Oxidoreductase 1 Beta
EtOH	Ethanol
FACS	Fluorescence Activated Cell Sorting
FBS	Fetal Bovine Serum
FFA	Free Fatty Acids
FGF	Fibroblast Growth Factor
FITC	Fluorescein Isothiocyanate
FLT1	Fms Related Receptor Tyrosine Kinase 1
FN1	Fibronectin
FOXA2	Forkhead Box A2
FZD3	Frizzled Class Receptor 3
GATA	GATA Binding Protein
GCG	Glucagon
GCK	Glucokinase
GFP	Green Fluorescence Protein
GHRL	Ghrelin
GJA	Gap Junction protein Alpha
GK	Glukokinase
GLUT	Glucose transporter
GMP	Good Manufacturing Practice
GO	Gene Ontology
GSIS	Glucose Stimulated Insulin Secretion
hASC	Human Adipose derived Stem Cells
HDL	High-density lipid particle

hESC	Human Embryonal Stem Cells
HEY1	Hairy/Enhancer-of-split related with YRPW motive-protein 1
HGF	Hepatocyte Growth Factor
HHEX	Haematopoietically Expressed Homeobox
hiPSC	Human induced Pluripotent Stem Cells
HMOX1	Heme oxygenase 1
HSPG	Heparan sulfate proteoglycans
HUVEC	Human Umbilical Vein Endothelial Cells
IAPP	Islet Amyloid Polypeptide
INS	Insulin
IRX	Iroquois Homeobox
K_{ATP}	ATP-sensitive potassium channels
KDR	Kinase Insert Domain Receptor
KEGG	Kyoto Encyclopedia of Genes and Genomes
KGF	Keratinocyte growth factor
KLF	Krüppel-Like Factor
KRB	Krebs Ringer Buffer
KRT	Keratin
LC-MS/MS	Liquid chromatography-tandem mass spectrometry
LDL	Low Density Lipoprotein
LED	Light-emitting diode
LOXL4	Lysyl Oxidase Like 4
MAFA/B	MAF BZIP Transcription Factor A/B
MCA	Microcavity arrays
MCAM	Melanoma Cell Adhesion Molecule
MDK	Midkine
MECOM	MDS1 And EVI1 Complex Locus
MIF	Macrophage Migration Inhibitory Factor
MMP	Matrix Metalloproteinase
MODY	Maturity onset diabetes of the young
mRNA	Messenger RNA
MSC	Mesenchymal Stem Cells
MV	Microvessels isolated from adipose tissue
NaOH	Natriumhydroxid
NCAM	Neural cell adhesion molecule

NEUROG3	Neurogenin 3
NKX6.1	Homeobox protein NKX6.1
NO	Nitric Oxide
NOS	Nitric Oxide Synthase
NOSIP	Nitric Oxide Synthase Interacting Protein
NOSTRIN	Nitric Oxide Synthase Trafficking
NPHS1	Nephrin
OCT3/4	Octamer-binding transcription factor 3/4
OoC	Organ-on-Chip
oxLDL	Oxidized Low density lipoparticles
P/S	Penicillin and Streptomycin
PBS	Phosphate-Buffered Saline
PCA	Principal Component Analysis
PDGFR	Platelet-Derived Growth Factor Receptor
PDMS	Polydimethylsiloxane
PDX1	Pancreatic And Duodenal Homeobox 1
PECAM	Platelet and Endothelial Adhesion Molecule
PFA	Paraformaldehyde
PGK1	Phosphoglycerate Kinase 1
Pi3K	Phosphoinositid-3-Kinasen
PP	Pancreatic Progenitor
PP cells	Pancreatic Polypeptide secreting cells
RA	Retinoic acid
RLU	Relative Light Units
ROBO	Roundabout Guidance Receptor 1
ROCK	Rho-associated protein kinase
ROS	Reactive Oxygen Species
RT	Room Temperature
S6	Stage 6 of β-cell differentiation
S6M	β-cell medium from stage 6
SC-	Stem cell
SC-EC	Stem Cell derived Endothelial Cells
SC-ILC	Stem Cell-derived Islet-Like Cluster
scRNAseq	Single-cell Ribonucleic Acid sequencing
SEMAi	Semaphorin iA

SERPINA1	Serpin Family A Member 1
SHH	Sonic hedgehog
SLE	Selective laser-induced etching
SORCS2	Sortilin Related VPS10 Domain Containing Receptor 2
SORT1	Sortilin 1
SOX	SRY-Box Transcription Factor
SST	Somatostatin
T1DM	Type 1 Diabetes Mellitus
T2DM	Type 2 Diabetes Mellitus
TAGLN	Transgelin
TBHP	Tert-Butyl Hydroperoxide
TCA	Tricarboxylic acid cycle
TEER	Transepithelial electrical resistance
TGF	Transforming growth factor
THBS	Thrombospondin
THSD	Thrombospondin Type 1 Domain Containing 1
ULA	Ultra-Low Attachment
UMAP	Uniform Manifold Approximation and Projection
UMI	Unique molecular identifiers
UV	Ultraviolet
vCo-culture	Vascularized co-culture
VE	Vascular Endothelial
VEGF	Vascular Endothelial Growth Factor
VSMC	Vascular Smooth Muscle Cells
VTN	Vitronectin
VWF	Von Willebrand Factor
WHO	World health organization
WSS	Wall Sheer Stress

1 Scientific context

1.1 The vascular system

1.1.1 Vascular endothelial cell biology

The human vascular system is a highly organized and dynamic cellular network that maintains homeostasis in all organs and functions through a complex network of arteries, capillaries, and veins[1]. The endothelial cell (EC) is the central cell type of the vascular system, which forms the inner wall layer of blood and lymphatic vessels and thus regulates blood flow, immune cell trafficking, oxygen, and nutrient delivery[2]. To comply with the multiple functions in the different organs ECs are highly plastic and heterogeneous[3]. In the human body, ECs face constant shear stress from blood flow, which regulates endothelial barrier function and influences EC health. ECs use multiple sensing mechanisms to detect mechanical stimuli and changes in hemodynamics have been associated with vascular dysfunction and diseases[4]. Shear rates vary depending on organ function, vessel size, or viscoelastic parameters of the blood and can range for example from 2 dyn/cm^2 in capillaries and lymphatic vessels to 10-70 dyn/cm^2 in larger arteries[5]. Further, ECs interact with different cell types such as vascular smooth muscle cells (VSMC) that line the blood vessel wall, except for capillaries. VSMCs are critical for regulating transendothelial transport[6], vascular contractility, and protect and stabilize the vessel[7]. In the human body, blood vessels can be classified according to their function. Arteries are the vessels that carry blood away from the heart, whereas veins carry blood towards the heart. Capillaries are the smallest blood vessels whose main function is the exchange of substances between blood and tissue. Arteries consist of three layers. The tunica intima comprises a single endothelial layer with a basement membrane and a subendothelial extracellular matrix (ECM)[8]. In the adult, the vascular basement membrane consists mainly of laminins, collagen type IV, nidogens, and the heparan sulfate proteoglycan perlecan[9]. VSMCs and ECM form the tunica media, while the tunica adventitia is the outermost layer and consists of connective tissue (**Figure 1**, a). Compared to arteries, veins also consist of three layers but contain less smooth muscle and connective tissue[8].

The process in which ECs assemble into tube-like structures and a new blood vessel is formed, is called vasculogenesis. During embryonic development, vessel formation is initiated where ECs differentiate from angioblasts into an arterial or venous lineage. Later, lymphatic ECs derive from already established veins. Specification to an arterial or venous EC type is highly controlled by growth factors like the vascular endothelial growth factor (VEGF) and Notch signaling[3]. The vascular network is further remodeled by angiogenesis, where a new

blood vessel develops from preexisting vasculature. Angiogenesis plays a crucial role in embryonic development but is also necessary in the adult organism for processes like wound healing or growth[10]. Angiogenesis can be divided into two pathways: splitting and sprouting angiogenesis. Sprouting angiogenesis can be initiated in response to angiogenic cytokines such as VEGFA. Thus, other cell types can initiate the formation of new capillaries in poorly perfused tissues by secreting proangiogenic growth factors[11]. During sprouting angiogenesis, the vascular basement membrane is degraded, and activated ECs begin to sprout and proliferate. The sprouting process includes tip cell formation of ECs exposed to high cytokine concentrations and the elongation of the sprout by proliferating stalk cells. Filopodia of tip cells are endowed with VEGFA receptors to navigate along the VEGFA gradient. Eventually, a lumen forms within the vascular sprouts, creating vascular tubes that are further stabilized by supporting mural cells. In contrast, splitting angiogenesis describes a process where a single existing vessel splits into two to form new capillaries. It plays a prominent role during embryonic development[11].

1.1.2 Atherosclerosis

Atherosclerosis is an inflammatory, vascular disease and gives rise to coronary artery disease, the most common form of cardiovascular diseases (CVD) [12]. According to the World Health Organization (WHO), CVD are the leading cause of death and morbidity worldwide, and risk factors include diabetes, obesity, smoking, an unhealthy diet, physical inactivity, genetic predisposition, and aging [13,14]. Major players in atherosclerosis progression are ECs, VSMCs of the vessel intima, and immune cells, leading to an immunoinflammatory disease and atherosclerotic plaque formation. The fatal consequence of atherosclerosis is thrombosis happening on an eroded or ruptured atherosclerotic lesion, which leads to life-threatening events such as heart attack or stroke[15]. The pathogenesis of atherosclerosis is characterized by an initial dysfunction of ECs and structural alterations such as disturbed flow and the accumulation of lipids. In an initial process, plasma lipoproteins such as low-density lipoprotein (LDL) accumulate in the intima of an artery, where they are oxidized by reactive oxygen species (ROS) or enzymes[12]. Oxidized LDL (oxLDL), among others, causes endothelial dysfunction, driving immune cell infiltration into the intima. In this process, blood monocytes bind to EC adhesion molecules and differentiate into macrophages. Lesional macrophages take up lipoproteins and give rise to foam cells, which often become apoptotic or necrotic initiating a necrotic core (**Figure 1**, b). The necrotic core consists of cholesterol esters, cholesterol crystals, and cell debris that increase the risk of rupture of the lesion. During atherosclerosis progression, VSMCs proliferate and migrate into the intima, where they build a fibrous cap by secreting ECM. Dysfunctional VSMCs also give rise to foam cells and bone-

like cells that secrete calcium phosphate minerals[16]. Results from animal studies suggest that up to 50% of lesional foam-cells are VSCM-derived[16].

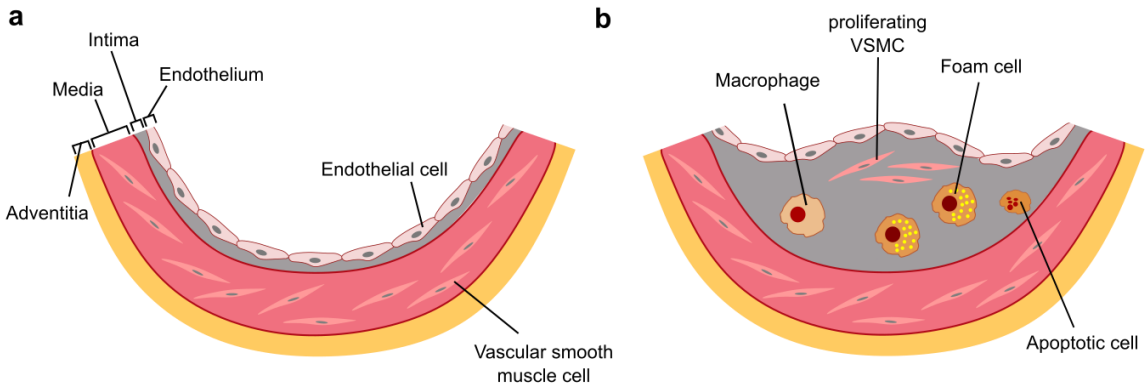

Figure 1: Artery vessel in health and after atherosclerosis progression. a An artery consists of three layers: i) The tunica intima that consists of a single layer endothelium, a basement membrane and extracellular matrix (ECM), ii) the tunica media composed of vascular smooth muscle cells (VSMC) and ECM and iii) the tunica adventitia which contains connective tissue. **b** When atherosclerosis progresses, macrophages and VSMCs start to migrate into the intima and proliferate. Macrophages take up lipoproteins and give rise to foam cells which often become apoptotic or necrotic. An atherosclerotic plaque is formed.

1.2 *In vitro* models for vascular research

Understanding EC development, adaptation, and response to microenvironmental cues is of central importance for revealing dysfunctions in the vascular network, for example, in chronic metabolic syndromes such as obesity, diabetes, and aging[17,18]. *In vitro* tissue models for human vascular systems have become indispensable for endothelial research because of the complexity of the human vascular system, the long-term development of vascular diseases particularly when cause by metabolic syndromes, and the distance of current rodent *in vivo* models to humans[19]. The crucial importance of the vascular system for all organ functions also means that *in vitro* vascularization models are becoming increasingly important to build physiological and functional tissue models *in vitro*. This subchapter, therefore, presents the principles of different *in vitro* models and their application in vascular research.

1.2.1 From 2D to 3D cell cultures

For decades, cell cultures have been used for the study of human biology, disease, therapy, and drug discovery. Traditional two-dimensional (2D) cell cultures have been used for

preclinical studies together with *in vivo* animal models to develop new therapeutic interventions. However, there has been a high failure rate of drugs that enter clinical trials as traditional *in vitro* and *in vivo* models often fail to recapitulate the human organ system[20]. In particular, 2D cell cultures cannot display the three-dimensional (3D) physiologic environment of human organs including mechanical and chemical stimuli and multi-layer of different cell types. These limitations have led to increased interest in alternative 3D cell culture models, which better represent the spatial and chemical complexity of living tissues. 3D cell cultures can be mainly divided into scaffold-free and scaffold-based approaches[21]. In scaffold-free cultures, cells cluster in self-assembling cellular microstructures known as spheroids or multicellular, mainly stem-cell-derived, organoids[22]. Scaffold-based approaches usually rely on a hydrogel matrix to introduce an ECM that enables cells to arrange in a spatial environment. The hydrogel matrices can be composed of natural materials, like collagen[23] or fibrin[24], or synthetic polymers[25]. Nonetheless, 3D cell cultures also have limitations. Among others, 3D cultures often lack mechanical cues including fluid shear stress, tension, and compression, which influence organ development and function. Further, organoids often face variabilities in size, shape, and maturation and are difficult to maintain in a constant position for long-term analysis[26]. The cultures also often lack vascularization, which is crucial for almost all organ functions. The lack of a perfusable vasculature in 3D organoid models can also lead to the formation of a necrotic core, caused in particular by the lack of oxygen and nutrients. Therefore, the integration of vasculature in organoid models is key for long-term *in vitro* cultures, to mimic *in vivo* physiology and functionality, and to study EC-cell interactions.[27].

1.2.2 2D and 3D cell culture models for vascular research

In vascular research 2D and 3D *in vitro* models are used to study vascular function, vascular diseases, endothelial development, or angiogenesis. The simplest approach is the culture of ECs on a 2D matrix-coated surface which will self-assemble into luminal tube-like structures. Those tube formation assays can be easily quantified and the effect of certain compounds on the tube formation capabilities can be evaluated[28]. However, to study the complex cell interactions in vascular diseases, like atherosclerosis, 2D cell cultures reach a certain limit. Although studies like Noonan et al [29] try to study the interaction of ECs, VSMCs, and monocytes in 2D layered compartments, those models lack the complex vascular geometries and 3D information seen *in vivo*[30]. In recent years, vascular organoids have become of interest in modeling human vasculature more closely and recapitulating the mechanisms underlying vascular diseases [31]. Vascular organoids have been used to study vascular development and angiogenesis within a hydrogel[31], or organoids with multiple cell types like ECs and VSMCs have been developed[32]. The incorporation of multiple cell types into vascular organoids opens

up new avenues for investigating the complex interplay of different cell types, for example in CVD. For example, Wimmer et al[33] published a blood vessel organoid model with ECs and VSMCs to study their interaction in diabetic vasculopathy *in vitro* and *vivo*. Despite their advantages over 2D models, vascular organoid models also reach their limits as they cannot mimic luminal structures of larger blood vessels. They also lack perfusion, which is essential for EC function. Here, organ-on-Chip (OoC) models enable the simulation of more complex geometries, including fluid flow[30].

While primary cell lines such as human umbilical vein ECs (HUVEC) are the most common cell type for vascular models, human stem cell-derived ECs (SC-ECs) are increasingly being used. SC-ECs can be differentiated from pluripotent stem cells[34], such as embryonic stem cells (hESCs) and human induced pluripotent stem cells (hiPSCs). Human ESCs derive from the inner cell mass of blastocysts and are pluripotent, meaning that all three germ layers can be derived from the hESCs. In contrast, hiPSCs are reprogrammed human somatic cells and can be generated by the ectopic expression of the transcription factors OCT3/4, KLF4, SOX2 and c-MYC. They share similarities with hESCs in morphology, transcriptome, and epigenome, are also pluripotent but have less ethical concerns[35]. Especially vascular organoid models increasingly use SC-ECs as they offer several advantages compared to primary cell lines. SC-ECs can be used to recapitulate vascular development *in vitro*[36], and differentiation protocols offer the opportunity to differentiate not only SC-EC but also other cell types such as VSMCs[28]. Additionally, SC-ECs can represent patient-specific backgrounds, which is especially interesting for the modeling of CVD.

1.2.3 Organ-on-Chip technology

Organ-on-Chip (OoC) models are biomimetic systems reflecting structural and functional characteristics of human tissue using microfluidic devices. OoCs allow the culture of engineered or miniature tissues on a small scale while enabling the control of the cellular microenvironment. The main parts of the chips include: i) a microfluidic system to induce media flow, ii) channels or chambers for the culture of cells (including commercial cell lines, primary cells, stem-cell derived cells or organoids) or tissue segments and iii) optionally a scaffold or hydrogel mimicking a 3D environment and ECM. Like this, OoC systems can recapitulate multicellular architectures, tissue-tissue interfaces, physicochemical microenvironments, and vascular perfusion of the body[26]. Compared to other culture systems, it has been shown that OoCs are effective models of human physiology and disease overcoming some limitations of traditional 2D or 3D cell cultures. Especially the fluid flow allows for longer culture times and reduced apoptosis as nutrients, oxygen, and waste can be

transported in and out of the culture system. In addition, fluidic shear stress can increase cellular maturation and differentiation, especially of stem-cell derived cell types, as has been shown for multiple organs[37–40]. OoC models can also include ECs for vascularization, showing improvements such as cell maturation and function[39,41,42] or mimicking tumor vascularization[43,44]. Further, OoCs provide control over many system parameters that are often missing in 2D and 3D systems. Integration of microsensors that report on cultured cells and control over fluid flow and cell patterning have proven advantageous for the culture of different cell types[26]. Thus, OoCs may be regarded as a bridging technology between easy 2D *in vitro* culture and complex *in vivo* model organisms, offering more complex and physiological *in vitro* culture systems with better engineered microenvironments[45,46]. Nevertheless, current OoC systems also face challenges and need to be further adapted. One major challenge (also true for multicellular organoids) is that the integration of multiple cell types requires the use of a culture medium that is suitable for the culture of different cell types. This demands the systematic testing of different medium conditions and is highly dependent on the cell types involved[47]. In addition, OoC models are evolving into increasingly complex systems, especially when multiple cell types are cultured together. This requires appropriate analytical methods to analyze the cell types involved, their function and changes, and to decipher their interactions. So far, however, most OoC models are hampered by limited cell material for downstream analysis or a laborious extraction process of the cell material. Another challenge is the standardization of the production process of OoC models. Many systems are custom-made products and the lack of standardized procedures prevents the reproducibility of experiments and their upscaling[47].

1.2.4 Organ-on-Chip systems for vascular research

In recent years, OoC systems have been used to model vascular systems, CVD, mechanical cues, shear forces, and EC-cell interactions[4,30]. Starting from shear flow on 2D EC monolayers, vascular OoC systems have become more complex and can be categorized into two broad groups (**Figure 2**). The first group includes model systems with pre-patterned hydrogels for EC seeding and culture, often using soft lithography techniques, including polydimethylsiloxane (PDMS) molding[6,48]. These devices are often elaborate in production and involve complex pumping systems to induce flow. However, the use of pump systems enables the generation of higher shear stresses that can also mimic the flow rates of larger vessels. On the other hand, pump systems require the handling of tubing and bubble traps, which is prone to handling errors. One advantage of pre-patterned OoC systems is their reproducibility. Due to the predetermined structure, microphysiological parameters can be better controlled, and samples with the same geometries can be generated. The second group includes self-

organized EC networks by seeding single cells into a hydrogel[49,50]. Established vascular networks can be perfused mainly by gravity-driven flow. Gravity-driven flow can be induced using rock shakers or the leveling of media reservoirs. This reduces the complex handling procedures. However, it also reduces the shear rate that can be introduced. In addition, the random arrangement of the vessels cannot be controlled, which makes reproducibility more difficult. Both OoC groups are used for vascular research to investigate the biology of ECs and the vascularization of organoid models. To name a few, Lee et al[51] used a combination of both to engineer a self-organized system perfused by gravity-driven flow to study angiogenic sprout biology and autophagy. Arslan et al[50] utilized a self-organized model system with ECs and fibroblasts to vascularize cardiac microtissues and Palikuqi et al[52] used engineered ECs to vascularize different organoids such as islets. Maurissen et al[53] generated a self-organized vascular network on-chip to study diabetic retinopathy. Polacheck et al[6] published the characterization of a pre-patterned lumen seeded with ECs and Kim et al[48] used a three-channel patterned chip to engineer a vascularized lung cancer model. Further, OoC models have been used to study atherosclerosis, trying to recapitulate the complex interplay between disturbed flow, inflammation, and EC and VSMC dysfunction. Here, Su et al[54] published an arterial wall-on-chip model to study VSMC migration and inflammation, and Zhang et al[55] engineered a complex blood vessel-on-chip to study early atherosclerosis events like inflammation. Although SC-ECs are widely used in vascular organoids, most OoC models still use primary cell lines such as HUVEC.

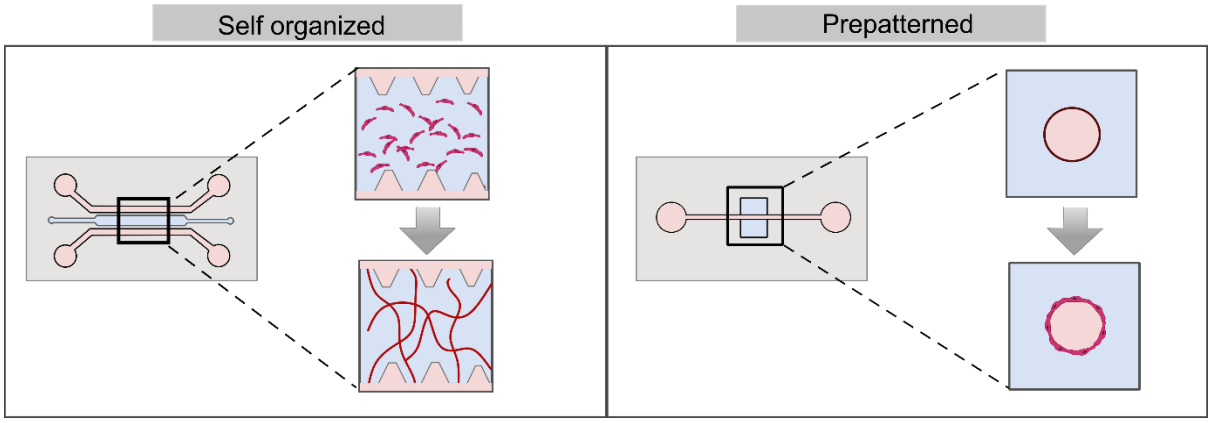

Figure 2: Organ-on-chip systems for vascular research can be divided into self-organized or prepatterned systems. In self-organized systems flow is mainly induced by gravity-driven flow and endothelial cells self-organize in a hydrogel channel forming perfusable vessels. Prepatterned systems create a channel in a hydrogel that can be seeded with endothelial cells, forming a perfusable lumen. Those systems mainly run with pump systems to induce hemodynamic flow but are often elaborate in use and production.

1.3 Diabetes mellitus and pancreas biology

The vascular system is also of crucial importance in the pancreas. Particularly the endocrine pancreas is a highly vascularized organ and ECs play an important role in its functionality. In addition, endothelial dysfunction is associated with diabetes mellitus, and CVD are the major cause of morbidity and mortality in diabetes[56]. This subchapter introduces pancreas biology, its dysfunction in diabetes mellitus, treatment options for diabetes with a focus on cell replacement therapy, and the role of the vascular system.

1.3.1 Pancreas biology

The pancreas is an endoderm-derived organ that consists of two compartments, the exocrine and the endocrine gland. In the exocrine tissue, acinar cells secrete digestive fluid containing inactive enzymes such as proteases, pancreatic lipases, and amylase[57]. Through the ductal system of the exocrine pancreas, the digestive fluid drains into the intestine, and ducal cells secrete bicarbonate and water to neutralize the pH of the gastric acid[58]. The inactive pro-enzymes in the digestive fluid get activated in the intestine, where they play a central role in digestion[57]. The endocrine part of the pancreas is composed of the islet of Langerhans that contain multiple hormone-producing cells (**Figure 3**, a-c).

Most of our knowledge about pancreas development is derived from animal studies, especially mouse models. Understanding human pancreas development relies on limited access to human samples like embryonic and fetal tissues. Although the micro- and macro-architectures of human and mouse pancreas differ[59], early pancreas development and marker expression are thought to be comparable between the species. Nevertheless, information on human pancreas development remains incomplete[60]. The human pancreas develops from the definitive endoderm (DE), which is one of the three germ layers formed during gastrulation. The DE population expresses markers like FOXA2 and SOX17[58]. After gastrulation, the endoderm gives rise to the primitive gut tube that is divided into foregut, midgut, and hindgut[61]. The foregut endoderm gives rise to pancreatic buds, positive for transcription factors like pancreatic/duodenal homeobox 1 (PDX1). Pancreatic buds contain multipotent pancreatic progenitor cells and can differentiate into all three pancreatic lineages: acinar, ductal, and endocrine cells[58]. From the pancreatic buds, a highly branched, tubular epithelia tree-like network is formed. This pancreatic epithelium segregates into a tip and trunk domain. Cells of the tip domain develop into acinar cells and express markers like PTF1a, CPA1, or c-Myc[62]. In contrast, the trunk domain is characterized by the expression of transcription factors like PDX1, homeobox protein NKX6.1, and SOX9 and can differentiate into duct and endocrine

cells (**Figure 3**, d)[63]. For the endocrine differentiation, the expression of the transcription factor neurogenin 3 (NEUROG3) is transiently required. Endocrine cells assemble into islets and are apparent 12-13 weeks post coitus[58].

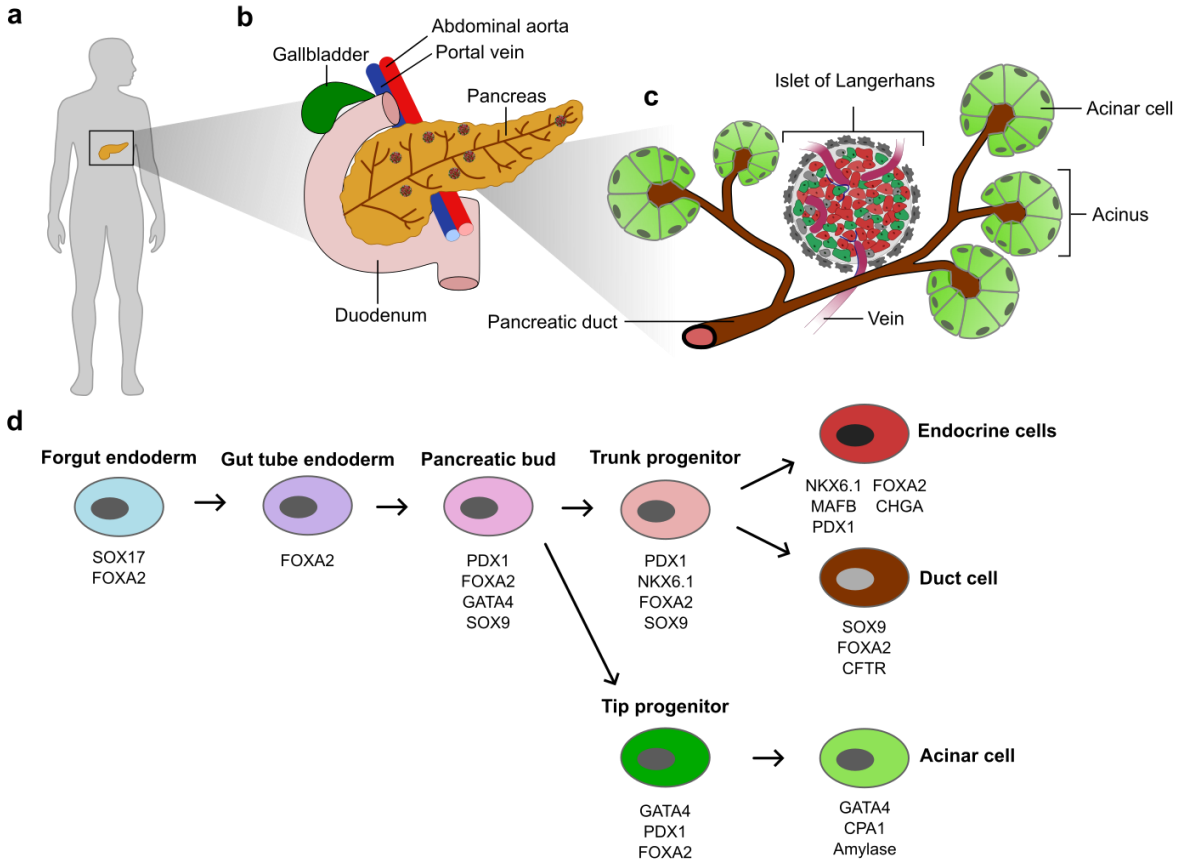

Figure 3: Pancreas anatomy and development. a The pancreas is a glandular organ of the human body. **b** Schematic location of the pancreas and neighboring tissue. **c** The pancreas consists of an exocrine and an endocrine part. The exocrine part consists of acinar cells that secrete digestive enzymes into the network of pancreatic ducts that secrete bicarbonate and water. The endocrine part of the pancreas is composed of highly vascularized islets of Langerhans, which include several hormone-producing cells such as insulin-producing β-cells, glucagon producing α-cells, somatostatin producing δ-cells, ghrelin-producing ε-cells and pancreatic polypeptide-secreting cells. **d** Scheme of human pancreas development. Important gene expression of the different stages is indicated. The differentiated endocrine cells include mainly β- and α-cells. Figure partly adopted from Ref[64].

1.3.2 The islet of Langerhans

The endocrine part of the human pancreas consists of approximately 3.2 million islets of Langerhans. Cells within the islets secrete hormones like insulin, glucagon, and somatostatin into the blood to regulate blood glucose levels. The islets are composed of insulin-producing β-cells (50–75%), glucagon-secreting α-cells (25-35%), somatostatin-secreting δ-cells (10%),

pancreatic polypeptide-secreting cells (PP cells, <5%), and ghrelin-producing ε-cells (<1%). In addition, islets are highly vascularized to measure nutrient concentrations and release hormones into the blood circulation. (**Figure 4**). Further, islets are innervated with neurons, contain mesenchymal stromal cells, and ECM[65].

In the β-cells, insulin secretion is primarily stimulated by increased blood glucose concentration. Glucose uptake into the β-cell is mediated by glucose transporters, mainly GLUT1 in humans. The glucose is then metabolized within the cell, with glycokinase (GK) controlling the entry of glucose into the glycolytic pathway. This is followed by glucose oxidation via the tricarboxylic acid cycle (TCA) and the production of adenosin triphosphate (ATP), which increases the ratio of ATP to ADP (adenosin diphosphate) in the cell. This leads to the closure of ATP-sensitive potassium channels (K_{ATP}), which results in depolarization of the membrane and the opening of voltage-dependent calcium channels. This increases the intracellular Ca^{2+} concentration and triggers the exocytosis of insulin granules: the β-cell secrets insulin. This so-called triggering pathway is responsible for the first phase of insulin secretion. It is characterized by a sharp increase in insulin secretion within the first 10 to 20 minutes after glucose intake. A second pathway of insulin secretion is the amplifying pathway or second phase, which allows the sustained release of more insulin in the post-absorptive phase of ingested food. This pathway is mainly independent of the K_{ATP} channels and leads to the release and recruitment of more granules[66].

Glucagon release by α-cells is regulated by intrinsic and paracrine mechanisms, mainly by hypoglycemia. Comparable to β-cells, α-cells sense extracellular glucose by its uptake into the cell (mainly GLUT1), followed by glycolysis and the increase of ATP. Consequently, hypoglycemia results in low intracellular ATP levels. In contrast to β-cells, this leads to the closure of K_{ATP} channels, followed by membrane depolarization and the influx of Ca^{2+} into the cell. The increase in intracellular Ca^{2+} triggers the exocytosis of glucagon granules. Conversely, hyperglycemia leads to the increase in intracellular ATP levels, the opening of K_{ATP}-channels, and the prevention of glucagon secretion. Both, insulin and glucagon secretion can be controlled by various other factors. One of these is somatostatin, which, when secreted by δ-cells, inhibits the secretion of both hormones[67].

1.3.3 The islet endothelial cell

Although islets of Langerhans account for only 1-2% of pancreatic volume, they receive about 15% of the blood supply[68]. The islet capillaries are important for the exchange of nutrients and hormones between blood and islet cells. Within the islet, the interaction of islet-ECs and endocrine cells is crucial, regulating endocrine formation, development, β-cell maturation, and

function[65]. Islet-ECs express unique surface markers, produce growth factors[69], and secrete the islet ECM and basement membrane, composed of collagen type IV and VI and laminins, important for islet function. The communication of islet-ECs and endocrine cells, especially β-cell, is important for both cell types. For instance, β-cells secrete VEGFA, improving EC viability and migration, and insulin secretion by β-cells is required for the phosphorylation of the nitric oxide synthase (NOS3) leading to the production of nitric oxide (NO), thus increasing EC function[68]. In addition to the expression of known EC markers (for example CD31 or von Willebrand factor), islet-ECs express specific surface markers that are characteristic for the islet vasculature. Thus, the expression profiles of islet-ECs differ from those in the surrounding exocrine tissue and illustrate how heterogeneous the microvasculature can be even within an organ[69]. Besides the expression of islet ECM components, the expression of thrombospondins (TSP-1 and TSP-2), hepatocyte growth factor (HGF) or connective tissue growth factor (CTGF) are among the characteristics of islet-ECs[70]. In addition to their important role in healthy islets, accumulating evidence suggests that the islet endothelium is involved and affected by pancreatic diseases, in particular diabetes mellitus[68].

1.3.4 Diabetes mellitus

Diabetes mellitus is a complex and multifactorial disease characterized by insufficient levels of insulin and triggered by genetic and/or environmental factors. Over 500 million people are suffering from diabetes worldwide and incidences are rising[71]. The vast majority of those patients suffer from Type II diabetes (T2DM) (over 90%) which is caused by an acquired insulin resistance resulting in β-cell dysfunction. T2DM develops as a cause of environmental and genetic factors and is strongly linked to overweight and obesity. T2DM therapy involves lifestyle changes, including a healthy diet, physical activity, and maintenance of healthy body weight that can also include weight-loss surgery. In addition, medication is initiated if the blood glucose levels cannot be controlled sufficiently. As traditional monotherapies often prove unsuccessful in managing blood glucose levels, research on better treatment options, e.g. dual agonists, is ongoing[72,73].

In contrast to T2DM, Type I diabetes (T1DM) is caused by an autoimmune destruction of the insulin-producing β-cells through T-cell mediated inflammatory and a humoral (B cell) response[74]. In 2022, around 9 million people suffered from T1DM of whom 80 to 90% are children and young adults. The cause of the disease is poorly understood, but a combination of genetic predisposition and environmental triggers is most likely. Patients with T1DM depend on daily insulin injections to lower their blood glucose levels. Despite improvements in insulin delivery by insulin pumps or artificial pancreas, patients still suffer from poor glycemic control,

which can result in life-threatening complications from hypoglycemia, diabetic ketoacidosis, and vascular complications. Thus, even with access to multiple insulin injections per day or insulin pumps, glucose monitoring, and proper medical education and care, living with T1DM remains challenging[73].

Next to the two main types of diabetes, some patients suffer from other diabetes forms, including monogenic diabetes. Monogenic diabetes is less common and results from mutations in a specific gene rather than multiple genes and environmental factors. One form of monogenic diabetes is maturity-onset diabetes of the young (MODY). In addition, the WHO published a report on the classification of diabetes mellitus, including diabetes caused by diseases of the pancreas, endocrine disorders, or drug/chemical induced diabetes[73].

1.3.5 Stem cell-derived islets for cell replacement therapy for diabetes

Although insulin replacement is lifesaving for patients with T1DM, the disease is not cured, and complications in glycemic control and secondary complications, such as CVD, can occur. In addition, most recent insulin replacement therapies like artificial pancreas can fail in patients with unawareness of hypoglycemic events such as brittle T1DM[75]. Recent advances in β-cell research and technology have led to new approaches including β-cell replacement[65] or the protection and regeneration of β-cells, including immunotherapy[76,77] or pharmacological intervention[78] .

Cell replacement therapies have the potential to re-establish glycemic control, decreasing the risk of hypoglycemic events, and preventing life-threatening complications associated with diabetes[75]. Currently, approved replacement therapies for T1DM include transplantation of cadaveric islets or whole pancreas. The landmark for clinical islet transplantation was the establishment of the Edmonton protocol in 2000, where cadaveric islets are infused into the hepatic portal vein. The transplantation requires heavy immunosuppression in the first days but also chronic treatment to prevent the rejection and destruction of the allogeneic islets[79]. Since the first transplantation trials, follow-up studies have shown improved graft survival of over 10 years[80,81], as well as increased transplantation safety[82]. In recent years, pre-clinical and clinical studies have also reported other transplantation sites like the kidney capsule or subcutaneous space[79]. However, the limitation of islet transplantation is the shortage of donor material and the reliance on immunosuppressive drugs, which inhibit the widespread adoption of pancreatic or islet transplantation therapies in T1DM.

Here, differentiation of human pluripotent stem cells, such as hESCs and hiPSCs, hold great promise for T1DM islet transplantation as they can serve as an unlimited source of stem cell-derived β-cells (SC-β-cells). First *in vitro* protocols for generating stem cell-derived islet-like

clusters (SC-ILC) were done with hESCs[83–86]. But by now, those protocols are adapted for the differentiation of hiPSCs, which have less ethical concerns and have the potential for autologous transplantation[35]. Differentiation protocols try to mimic the embryonic pancreas and islet development in a stepwise protocol, starting with DE induction, followed by the pancreatic progenitor stage, continuing to endocrine progenitors, and ending with islet cells (**Figure 4**). Beginning with the pluripotent stem cells, the cells are stepwise supplemented with small molecules and growth factors that are known to drive pancreas development. Most of our knowledge about pancreas development is derived from animal studies, especially mice, and differentiation protocols and applied supplements largely depend on mouse developmental biology[60]. Thus, different human differentiation protocols and strategies are available, which are still being further developed to generate mature, insulin-producing SC-β-cells. Initial differentiation protocols have been performed in 2D monolayers [86], which have been further developed to dynamic 3D cultures such as cultures in spinner flasks. This will allow to scale-up SC-β-cell differentiation in the future[85]. The differentiation protocol [85] used in this dissertation follows the pancreatic differentiation in a 3D protocol starting with DE induction by targeting the WNT pathway and addition of TGFβ receptor ligand activin A. Induction of primitive gut tube and the further development to pancreatic buds can be resembled *in vitro* by exposure to keratinocyte growth factor (KGF)[35] followed by addition of retinoic acid (RA), bone morphogenic protein (BMP) antagonist LDN193189 and sonic hedgehog (SHH) inhibitor SANT-1[85]. Pancreatic progenitor expansion requires EGF and Notch signaling targeted by betacellulin and γ-Secretase inhibitor, respectively. Next, the endocrine lineage is induced by the targeting of several pathways including TGFβ inhibition by Alk5i[85]. Addition of several factors, including antioxidants like N-acetylcysteine or vitamin C have been reported to promote SC-ILC maturation[85,86]. So far, the *in vitro* generated SC-ILC are still of unmature, embryonal character and the differentiated population is heterogeneous, consisting not only of the endocrine cells but also of off-target cells like enterochromaffin cells and polyhormonal cells, double positive for glucagon and insulin[65]. However, SC-ILC can mature when exposed to an *in vivo* environment by transplantation[87,88].

Importantly, SC-ILC still require immunoprotection when transplanted into patients. To this end, researchers have focused on studying immune β-cell crosstalk [89], alloimmunity and autoimmunity after transplantation[90] as well as patient-specific diabetes research [91] . Further, research on genetically modified SC-ILC[92,93] or co-transplantation with immune-regulatory cells[94] is ongoing to prevent rejection by the patient's immune system without the need of immunosuppressors. Another promising strategy for islet immune protection is islet encapsulation into biomaterials. The encapsulation should protect the islets from the host´s immune system, limit hypoxia and at the same time allow for the exchange of oxygen, glucose,

and insulin[79]. There are different strategies published ranging from nano-encapsulation with a thickness of <100nm to macro-encapsulation where multiple islets are encapsulated in a device of > 1mm[79]. Despite the difficulties that still exist, the company Vertex published their first trial[95] in transplanting allogeneic SC-ILC into the first patient in 2022. And the company ViaCyte transplanted SC-pancreatic progenitors in a subcutaneous encapsulation device[96].

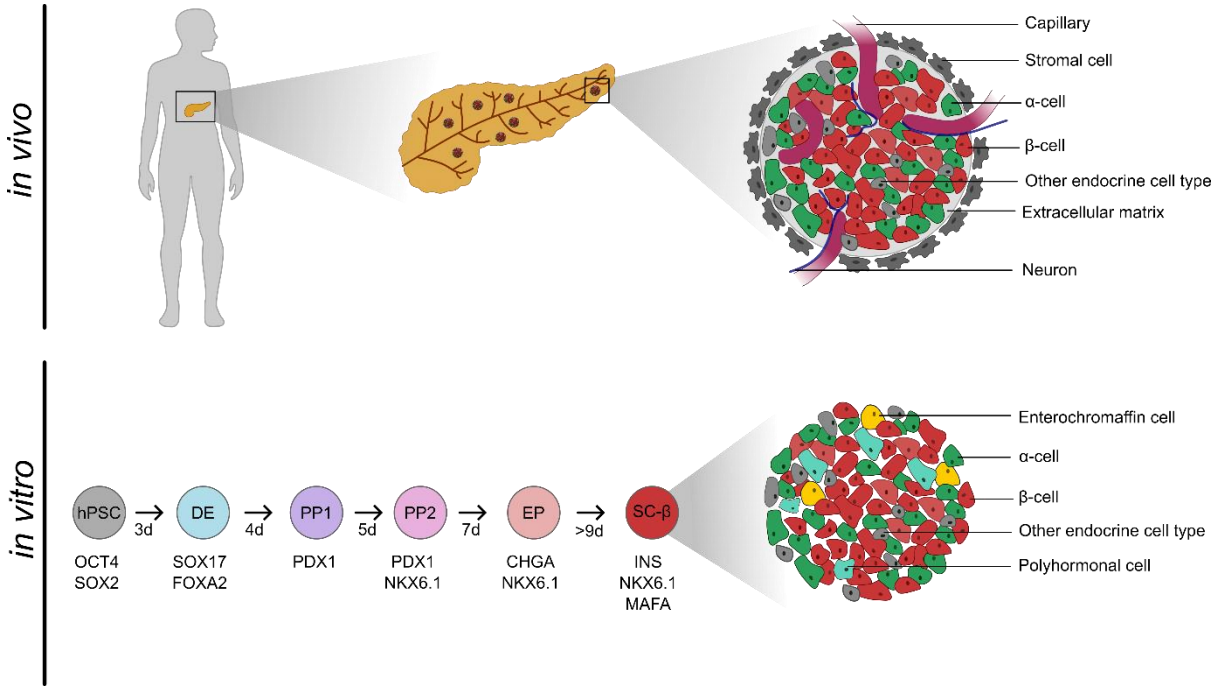

Figure 4: Human islets of Langerhans *in vivo* compared to stem cell-derived islets *in vitro*. Native islets of Langerhans are complex micro-organs composed not only of endocrine cells, but also of extracellular matrix (ECM), stromal cells, nerves and capillaries. The endocrine cells include glucagon-producing α-cells, insulin-secreting β-cells, somatostatin-secreting δ-cells, pancreatic polypeptide-secreting cells and ghrelin-producing ε-cells. For the *in vitro* differentiation of β-cells, human pluripotent stem cells can differentiate into stem cell-derived islet-like clusters (SC-ILC). The differentiation protocol follows the pancreas development in an elaborate protocol[85], taking several weeks (days and marker expression are indicated for each stage). SC-ILC are composed of immature SC-β-cells, SC-α-cells and off-target products like serotonin-producing enterochromaffin cells, and insulin and glucagon double-positive polyhormonal cells. Further, SC-ILC lack a vascular system, ECM, and supporting stromal cells. hPSC, human pluripotent stem cells; DE, definitive endoderm; PP, pancreatic progenitors; EP, endocrine progenitors; SC-β, stem cell-derived β-cells. Figure partly adapted from Ref[65].

1.3.6 Vascularization approaches for pancreatic islets

While the primary pathologic feature of diabetes is β-cell dysfunction, other pathologic abnormalities have been described in association with the disease[97]. In particular, the vascular system shows alterations, and vascular complications are the main cause of morbidity and

mortality in diabetic patients. The metabolic changes mainly lead to endothelial dysfunction and atherosclerosis and can affect both the macro- and microvascular system[56]. In addition, an altered morphology and function of the microvasculature within the islets have been reported. These include changes in vessel diameter, capillary density, ECM composition, increased vascular leakage, and abnormal flow dynamics[97]. Besides, there is evidence that the islet endothelium is involved in generating inflammatory responses during the development of T1DM by allowing immune cells to invade the endocrine tissue [69].

Most of our knowledge about the vascular changes in diabetes comes from rodent models and clinical data[69]. However, clinical data often only reflect end-states in patients and the elucidation of early, asymptomatic phases is difficult. Additionally, when comparing the vessels in human islets with those of rodents, significant differences can be observed. In rodents, the islets have a fine network of capillaries, whereas humans have significantly fewer but larger vessels[68]. In addition, rodents are metabolically different from humans[19]. This emphasizes that rodents can only partially reflect the biology of human islet cells and vascular dysfunction and that human research models are needed to clarify the complex interactions between ECs and endocrine cells.

Despite the existing gap of *in vivo* models and clinical studies for the investigation of vascular dysfunction in diabetes, most *in vitro* vascularization models for islets focus on a different problem. Islet vascularization also plays an important role in islet transplantation for T1DM therapy. SC-ILC lack any vascularization and cadaveric islets lose most of their vasculature during isolation[98]. The poor vascular density leads to poor engraftment, resulting in delayed and sub-optimal glycemic control. As a dense vascularization of the islets is important for islet function and survival, a prevascularization of the transplant can have a positive impact on β-cell maturation and holds promise to decrease the loss of transplant material and to advance revascularization. Therefore, researchers have worked on the vascularization of islet cells in recent years. To name some, Aghazadeh et al[99] and Wrublewsky et al[100] showed improved β-cell survival and glucose response when co-transplanted with ready-made microvessels from adipose tissue (MV); Takahashi et al[101] reported a “self-condensation” culture for the self-organization of islets with ECs and the benefit of the vascularization for transplantation outcome and graft survival; Nguyen-Ngoc et al[37] and Bender et al[41] showed that the efficient vascularization of islets *in vitro* increased β-cell functionality and glucose response. In addition, other methods like encapsulation devices and scaffolds[102], OoC systems[52,103], or adding supporting cell types like mesenchymal stromal cells[104–106] have been reported to improve islet vascularization *in vitro* and *vivo* (**Figure 5**). Current protocols have focused on the use of HUVEC or MVs for islet vascularization, whereas stem cell-derived ECs (SC-ECs)

have not been reported. Although, scientists have made great progress in islet vascularization, the vascularization of the islet core is still very challenging and has only been achieved *in vivo*.

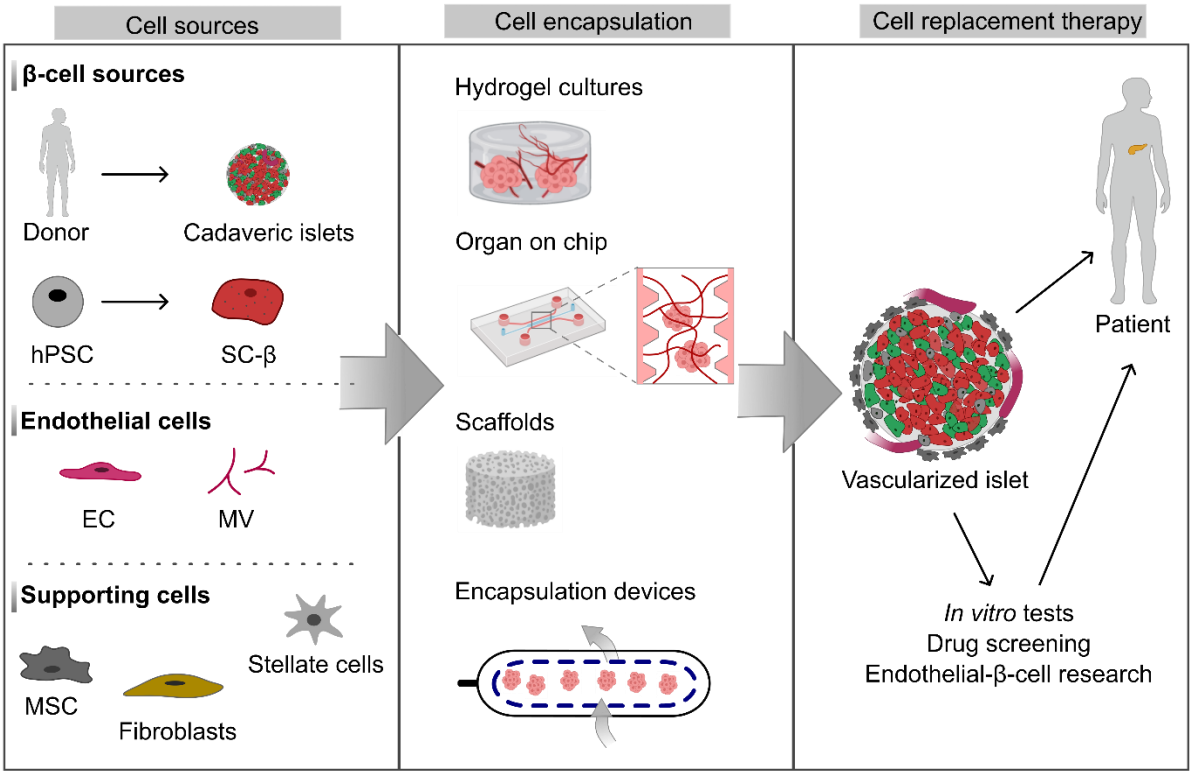

Figure 5: Approaches for islet vascularization. Current research has focused on two building blocks for islet vascularization. First, islets are either isolated from human donors or differentiated from human pluripotent stem cells (hPSC) and co-cultured with endothelial cells (EC) or microvessels isolated from adipose tissue (MV). In addition, supporting cell types were added in some approaches to increase β-cell functionality or for immunomodulatory effects. The second building block concentrates on cell encapsulation strategies ranging from hydrogel cultures to organ-on-chip platforms or encapsulation devices. All together those strategies showed improvement of islet vascularization and glucose response *in vitro* or in *in vivo* mouse models. Vascularized islets can be used for *in vitro* characterization and research of endothelial β-cell crosstalk and hold great promise for cell replacement therapies. hPSC, human pluripotent stem cells; SC-β, stem cell derived β-like cells; MSC, mesenchymal stem cells. Figure partly generated with BioRender.

1.4 Methodic background – characterization of *in vitro* models

To better mimic the *in vivo* situation and the physiological environment of different organs such as islets or the vascular system, *in vitro* models are becoming increasingly complex. Cultures of multiple cell types or OoC technologies emerge to model the tissues as closely as possible and to generate culture systems that can replace animal models. This complexity requires

analytical approaches to decipher e.g. cell-cell interactions, maturation profiles, proteomic and transcriptomic cell states, cellular function, or differentiation pathways. In this doctoral thesis, different analytical approaches were used and are addressed in the following subchapters.

1.4.1 Monitoring of 3D cultures with impedance spectroscopy

As *in vitro* models develop to more complex 3D systems, adequate monitoring techniques are of need. Especially when culturing and differentiating organoids over several weeks, cell growth and cell health monitoring is necessary. Currently, most monitoring techniques are end-point techniques like histology, immunofluorescent staining, or flow cytometry. However, this often requires the destruction of the *in vitro* tissue for analysis. Live cell approaches like reporter constructs are time-consuming to develop and have limited light penetration within a 3D culture. Impedance spectroscopy has become of more interest in recent years as an automation-compatible technique for the real-time, label-free monitoring of 2D and 3D cultures. In impedance spectroscopy, changes in current/voltage through the cells are measured while a frequency shift is performed. Like this, electric resistance and capacitance of cells can be monitored[107]. Traditionally, this method has been used, for example, to analyze cell proliferation, integrity, barrier function, or cellular degradation of adherent 2D cells[108–110]. In combination with microcavity arrays (MCA), impedance spectroscopy is suitable for 3D cell culture monitoring, such as analyzing changes in morphology, drug penetration, and cytotoxicity test[111] or the electrophysiological properties of cardiomyocytes[112]. Important for the impedance measurement is that the electromagnetic fields should not significantly affect the cells. Especially nerve and muscle cell membranes are sensitive and can be damaged with electrical fields as small as 60 V/cm [113]. Thus, the applied voltage or current strongly depends on the monitored cell type, number of cells, resistance of culture medium, and the special arrangement of electrodes and cells. For 3D cultures, the applied voltage typically ranges from 10 to 100 mV [113]. When measuring a 3D culture, the impedance is influenced by all cells within the electric field, including the membrane capacity, the membrane resistance of each cell, and the extracellular resistance[111]. Additionally, the cell culture medium or buffer influences the measurement, which is why appropriate controls must be carried along[113]. Impedance spectroscopy is suitable for high-throughput, non-invasive, and real-time monitoring of 3D cell culture systems. However, appropriate controls need to be considered to interpret the results correctly. Especially in 3D cell models the understanding of the parameters and their effect on the impedance is still imperfect.

1.4.2 Testing β-cell functionality

The primary function of islet cells is their ability to secrete hormones. Functional assays of human isolated islets and SC-ILC therefore aim to evaluate this ability with hormone secretion assays. The preferred test for β-cell function *in vitro* is a glucose-stimulated insulin secretion assay (GSIS). This can be performed either in static incubation or dynamically via perfusion. While static incubation provides information on the accumulated insulin release over time in response to insulin secretagogues, perfusion of islets can be used to study the kinetics of insulin secretion in a temporally resolved manner[114]. While in static GSIS about 10-20 islets are incubated in a well, in dynamic GSIS a larger number of islets (~100) is used. At the end of stimulation with a secretagogue or at specific time points, the supernatants are collected, and the released hormones are analyzed. Enzyme-linked immunosorbent assays (ELISAs) are used here as a standard to detect the hormones using an antibody-enzyme-based detection method. Although ELISAs have a high specificity and sensitivity[115], they are elaborate in time and cost (>$2/well[116]). Further, islet function can be evaluated by fluorescence microscopy, which provides insights into the spatial and temporal characteristics of hormone release. Here, the primary approach is Ca^{2+} imaging, which gives insights into Ca^{2+} influx and efflux, an important messenger in insulin secretion[114]. To test the function of SC-ILC in restoring normoglycemia, transplantation studies in mice are common. Islets are often transplanted into diabetic mouse models, and the glucose concentration is monitored in blood samples taken at regular intervals. In addition, glucose tolerance tests are performed in which the mice are first fasted and then injected with high glucose solutions[117].

1.4.3 Single-cell RNA sequencing for transcriptome analysis

Transcriptome analyses have been used to decipher the transcriptomic characteristics of different cells and thus gain deeper insights into complex biological systems. In the human body, there are many different cell types with a unique transcriptomic profile, and even similar cell types have been found to have differences in gene expression. This limits the power of conventional bulk sequencing, necessitating a more precise analysis of transcriptional changes at the single-cell level[118]. Since the first published single-cell RNA sequencing (scRNAseq) study in 2009[119], the number of publications on single-cell resolved transcriptomes has increased enormously. For scRNAseq, single cells need to be isolated to obtain transcriptome information from individual cells. Here, a microdroplet-based microfluidic technique[120] can be used, which embeds single cells into aqueous droplets in a continuous oil phase. This technique requires low sample volume and enables the screening of thousands to millions of cells[118]. As dead cells might bias the data and cause a high noise, a viability of 90% is recommended and cell suspensions can be filtered for live cells, if needed. Within the

generated water-oil droplets, cells are lysed, and unique molecular identifiers (UMI) are added to the mRNA. In a next step, captured mRNA transcripts from the droplets get reverse transcribed and amplified. Here, poly[T]-primers are commonly used to avoid the capture of ribosomal RNAs. The amplified cDNA is used for library preparation where cDNA molecules are tagged with sample-specific indexes to allow multiplexing. The generated libraries can be sequenced afterwards with a next generation sequencing platform. In the computational demultiplexing after successful sequencing, the UMIs and indices will be used to sort samples, cells, and transcripts[121]. The computational analysis of the scRNAseq data further includes alignment of the reads to a reference genome, quality filtering of the cells, normalization of count reads and feature selection (identifies genes with relevant biological information). A principal component analysis (PCA) is used to lower data dimensionality and cells are clustered and visualized based on their PCA scores[121].

1.4.4 Mass spectrometry for the analysis of proteome and secretome

In comparison to scRNAseq, proteome analysis deciphers cellular functionality on the protein level. While the proteomic approach focuses on cell or tissue lysates, secretome analysis examines the secretion of proteins by cells. Liquid chromatography-tandem mass spectrometry (LC-MS/MS) can be used to study complex proteome and secretome samples. During LC-MS/MS analysis the analyte molecules get converted into gas-phase ions and their mass-to-charge ratio (*m/z*) is being detected[122]. Like this, different molecules can be separated, identified, and quantified with high specificity and sensitivity, offering new possibilities for the deep analysis of samples in clinic and research. The most common MS-based proteomic approach is an untargeted bottom-up experiment using data-dependent acquisition (DDA)[123]. Here, proteins are harvested from biological samples and digested into peptides. LC-MS/MS analysis includes the separation of peptides by liquid chromatography and the measurement of ionized peptides by MS. In DDA the detected peptides get selected, isolated, and fragmented inside the mass spectrometer. The resulting data can be analyzed, including identifying the peptides' amino acid sequences and measuring their relative abundance. In this way, proteins and their relative abundances can be indiscriminately identified[123].

1.4.5 Immunofluorescence staining

ScRNAseq, as well as proteome and secretome studies, can resolve cell states in depth in *in vitro* models. However, they cannot reveal the spatial information within tissues. Therefore, immunofluorescence staining is often used to detect proteins by the binding of specific

antibodies to their antigen. By using fluorescently labeled antibodies, the expression of proteins can be detected by imaging[124]. Applied to tissue sections or whole cell cultures, immunofluorescence staining can be used to locally resolve protein expression, detect known cell markers, analyze the spatial distribution of different cell types, or detect morphological changes[64].

1.5 Methodic background – 3D printing for microfluidic chip production

Traditionally, microfluidic chips have been produced with PDMS by a technique called soft lithography. In soft lithography, microfluidic channels, membranes, or stamps are produced by making negative copies on a master mold with elastomeric polymers, for example PDMS[125]. PDMS offers various advantages such as biocompatibility, gas-permeability, and low cost. However, fabrication of PDMS devices is time-consuming and elaborate in production, hindering commercial translation[126]. 3D-printing is a technique that produces 3D objects layer-by-layer offering precise control over the fabrication process, fast adaptable prototyping, enabling high throughput, and an assembly-free, automated fabrication process[127]. In this thesis, stereolithography 3D printing was used, a process in which 3D objects are produced from a photoresin that gets selectively cured by a focused laser or LED light source. The minimal resolution of the 3D objects is thereby determined by the laser spot size and the photoresin used[127]. In recent years, 3D printing has become a powerful manufacturing tool with applications for medical engineering and the generation of customized biomedical products[128]. However, 3D printing faces limitations regarding surface properties, biocompatibility, or optical transparency. Among other things, the 3D printing process can lead to rough surfaces, which in the worst case can affect flow behavior or cell viability. In addition, the biocompatibility of many polymers is still unknown, so comprehensive cytotoxicity studies should be carried out before their use in cell culture[129].

2 Aims of the thesis

2.1 Thesis background

The vascular system is of central importance for all organ functions and endothelial dysfunction is associated with many diseases, such as diabetes[56]. Within the endocrine pancreas, islets are highly vascularized, islet-endothelial cells (ECs) effect endocrine function and maturation, and the vascularization of stem cell-derived islet-like clusters (SC-ILC) is important for their transplantation in diabetic patients[65]. In addition, the vasculature within islets is altered in diabetes[97], and cardiovascular diseases (CVD) are the major cause of morbidity and mortality in diabetic patients[56]. With the global increase in metabolic diseases, such as diabetes, research models for islet and vascular research are needed to improve our knowledge about disease onset, progression, and treatment options. Since animal models such as rodents are metabolically and biologically different from humans[19] and simple *in vitro* models cannot reflect the complexity of the human body[20], advanced human *in vitro* models are required to answer these questions. This doctoral thesis aimed to study EC and islet biology in such *in vitro* models with three interconnected projects.

2.2 Aims of the thesis

i. To study EC dysfunction in CVD, the application of Organ-on-Chip (OoC) systems offers the possibility to mimic vascular blood flow, thus creating a more physiologic environment than other 3D models. Additionally, combining OoC platforms with stem cell-derived ECs (SC-ECs) could offer the possibility to mimic patient-specific backgrounds, including those in CVD. However, SC-ECs have hardly been used in existing OoC models and it is still unclear how they develop and behave when cultured on-chip. In addition, existing OoC models are limited by the lack of scalability of the manufacturing and cultivation process. Furthermore, the increasing complexity of cell models and scientific questions requires the extraction of cells for in-depth biological studies. This is a problem that current OoC models cannot solve due to the complex manufacturing processes, small sample sizes and inaccessibility of the samples.

   Therefore, the aims of this thesis were to engineer a scalable OoC platform for endothelial vessels that allows i) the culture of SC-ECs under healthy conditions

and flow; ii) the investigation of SC-EC function on-chip; iii) the modeling of vascular dysfunction due to metabolic stress; and iv) the extraction of the vessels for deep biological and multiomics characterization.

ii. Vascularization is crucial for islet function, maturation, and transplantation. Especially the use of SC-ILC offers hope for cell replacement therapy in diabetes. However, SC-ILC lack any vascular system and are still of an immature phenotype *in vitro*. The development of vascularization strategies for islets is therefore of crucial importance to i) improve islet transplantation outcome; ii) to further mature SC-ILC *in vitro*; and iii) to gain insight into the complex interactions between endocrine cells and ECs in human *in vitro* models, which play a crucial role not only in the healthy but also in the diseased diabetic state.

Therefore, this thesis aimed to develop a stem cell-derived *in vitro* model of SC-ECs and endocrine SC-β-cells to i) vascularize SC-ILC *in vitro*; ii) investigate how vascularization affects the maturation of SC-β-cells; and iii) study the interaction of SC-ECs and SC-β-cells *in vitro* to gain more information about their crosstalk in the islet niche.

iii. Existing functional *in vitro* tests of human islets and SC-ILCs mostly rely on secretion studies and their evaluation with ELISAs. These tests reach their limits with regard to the use of cell material, high costs, and scalability. Therefore, scalable and cost-effective screening assays are needed to develop better differentiation protocols, screen SC-ILCs for maturation and function, and test diabetes drugs.

Therefore, the aim of this thesis was to establish a non-invasive, high-throughput and cost-effective method for testing β-cell functionality to i) replace expensive ELISAs; ii) screen SC-ILC; and iii) establish an alternative method for future drug screening in diabetes research.

2.3 Structure of the thesis

Given the aims of this doctoral thesis, the chapters are organized as follows: Chapter 3 focuses on the characterization of SC-ECs and their use in a vessel-on-chip model that enables deep, multiomics characterization in health and disease. In this context, SC-EC-derived vessels were cultured under shear stress using a microfluidic chip system and were characterized by functional assays and single-cell RNA sequencing (scRNAseq). Next, an atherosclerosis disease model was established on chip and characterized by proteomic and secretome analysis and functional assays. In Chapter 4, a 3D *in vitro* model was established for the vascularization of SC-ILC. Thus, a model system for the islet microenvironment was generated, including SC-ECs, extracellular matrix (ECM), and stromal cells. Within the establishment vascularized co-culture model, the influence of the islet microenvironment on all cell types was investigated. In the vascularization model, cell-cell interaction could be studied, and endocrine functionality and transcriptomic changes were evaluated. Next, chapter 5 focuses on a high-throughput screening platform for SC-ILC to evaluate their function. Here, impedance spectroscopy was used as a method for non-invasive analysis of insulin secretion by stem cell-derived β-cells (SC-β) in single SC-ILC. The approach was tested for its use in drug screening on SC-ILC for diabetes research.

3 Stem Cell-Derived Vessels-on-Chip for Cardiovascular Disease Modeling

This chapter is cited from the publication: Marder, M.[$], **Remmert, C.[$]**, Perschel, J. A., Otgonbayar, M., von Toerne, C., Hauck, S., Bushe, J., Feuchtinger, A., Sheikh, B., Moussus, M. and Meier, M. (2024). Stem Cell-Derived Vessels-on-Chip for Cardiovascular Disease Modeling. Cell Reports. Volume 43, Issue 4, 23 April 2024, 114008.

$ Authors contributed equally. Author order was decided randomly.

3.1 Declaration of contribution

Experiments, analysis, and results in the following chapter were obtained equally by me and Maren Marder. This included: differentiation of hiPSCs to endothelial cells, their sorting and culture; seeding and culture of the chip; the functional analysis such as FITC-dextran assay, NO assay, ROS analysis and whole mount immunofluorescent staining; the scRNAseq experiment; the sample preparation for the proteome and secretome analysis. Further, we equally performed the analysis of the sequencing and mass spectrometry data. The chip presented in Figure 6 was prepared by Julius Perschel, Munkhtur Otgonbayar and Michel Moussus, where design elements were adopted in feedback iteration based on my and Maren Marder's experimental results. Christine von Toerne performed the mass spectrometry measurement. The study was designed by me, Maren Marder, and Matthias Meier in equal parts. Bilal Sheikh advised the study design for FFA treatment. The manuscript was written by me, Maren Marder and Matthias Meier. Author contributions are also stated in the publication in Cell Reports.

3.2 Introduction

The human vascular system is a highly organized and dynamic cellular network responsible for maintaining homeostasis in all organs. Endothelial cells (EC) are the central cell type of the vascular system, which form the inner wall layer of the blood and lymphatic vessels and thus regulate blood flow, immune cell trafficking, oxygen, and nutrient delivery[2]. To comply with the multiple functions in the different organs ECs are highly plastic and heterogeneous. Single-cell transcriptomics has confirmed the trans- and intra-tissue EC heterogeneity[3],

however, how they evolve and which microenvironmental factors shape EC states remain unclear. Understanding EC development, adaptation, and response to microenvironmental cues is of central importance for revealing dysfunctions in the vascular network, for example, in chronic metabolic syndromes such as obesity, diabetes, and aging[17].

In vitro tissue models for human vascular systems have become indispensable for endothelial research because of the complexity of the human vascular system, the long-term development of vascular diseases due to metabolic syndrome in patients, and the metabolic distance of rodent *in vivo* models to human biology[19]. Engineered, stable cell types that carry genetic predispositions to vascular diseases are hence best suited to recapitulate human vessels *in vitro*. Human inducible pluripotent stem cells (hiPSCs) are an almost unlimited EC source, where phenotypes are highly reproducible within the same hiPSC line[130]. Various differentiation protocols have been developed to engineer hiPSC-derived ECs (SC-EC)[131]. Upon culturing SC-EC in a hydrogel environment, tubular microvessel structures are formed, and single-cell transcriptomic analysis resolved transcriptional changes during their formation, including sprouting, coalescence, and tubulogenic cell states[31]. However, SC-ECs within microvessels exhibit immature, nonspecialized character[132–134]. While mechanical properties of SC-ECs within organoid and hydrogel cultures can be modulated, the shear flow cannot due to missing accessibility of the microvessel luminal site. However, shear flow regulates various EC functions, such as proliferation and differentiation, through transcriptomic and epigenomic changes[135,136]. The role of shear flow in the development of SC-EC is not completely explored. Under physiological conditions, blood flow occurs unidirectional, where the wall shear stresses vary largely depending on organ function, vessel size, or viscoelastic parameters of the blood. For example, shear rates in capillaries or lymphatic vessel are in the order of 2 dyn/cm^2, whereas in larger arteries the shear stress ranges from 10 as high as 70 dyn/cm^2 [5].

Generally, *in vitro* ECs are exposed to flow shear forces by engineering microfluidic cell culture systems in which ECs are either cultured on two-dimensional (2D) surfaces of a microchannel[137], allowed to self-assemble into microvasculature in hydrogel microchambers[138], or formed upon assembly onto hydrogel-patterned microchannel walls[139]. The latter organotypic vessel-on-chip systems have the advantage of being reproducible and robust because microchannel geometry determines the form factor of the vessel size. Concomitantly, the mechanical microenvironments are adjustable through the hydrogel matrix composition used to form the microchannels. However, miniaturized vessel-on-chip systems inevitably have a low cell sample availability for downstream analysis, which is a challenge for all organ-on-chip (OoC) approaches. Furthermore, large chip footprints hamper higher parallelization degrees under standard cell culture laboratory environments but are required

to obtain sufficient statistical repeats for disease condition testing. To date, vessel-on-chip platforms have mainly been generated using primary and immortal endothelial cells[140]. The next step in building human vascular disease models is integrating SC-ECs. Additionally, stem cell systems enable genetic engineering of predispositions or access to the early onset of vessel dysfunction.

Functionally, on-chip vascular disease models have been used to recapitulate the onset of atherosclerotic development. Atherosclerosis pathogenesis involves the accumulation of lipids, mainly cholesterol-containing low-density lipoproteins (LDL), in the arterial ECs. Subsequently, the generation of reactive oxygen species (ROS) leads to the formation of lesions within the vessels, where the oxidative environment leads to EC dysfunction, impairs vasodilation through the reduction of nitric oxide (NO) synthesis, induces disturbed flow, and stimulates inflammatory responses[141]. Oxidized LDL particles (oxLDL) are involved in the induction of the early characteristic events of atherosclerosis. In addition to oxLDL, excess free fatty acids (FFA) are present in patients with atherosclerosis. FFA pathomechanisms are not well-known; however, a decrease in vasodilating NO and increased ROS production have been reported[142,143].

We here report the development of a human stem cell-based blood vessel-on-chip model. The open design of the 3D-printed microfluidic chip platform enables multiomics downstream cell analysis with a low sample volume and cell number. Gravity-driven flow on-chip induced barrier function, sprouting, and arterial toning of SC-ECs as shown by single-cell transcriptomics and high-resolution imaging. Upon individual stimulation of SC-ECs with oxLDL and FFA, early-onset of atherosclerosis hallmarks were monitored. Proteomic and secretome changes in the vessel-on-chip system due to oxLDL or FFA stimulation under flow revealed distinctive ROS and NO synthesis responses. Taken together, we provide a fully integrated stem cell-based vessel model for multiomics cell analyses that can readily integrate with epithelial tissues of distinct origins.

3.3 Material and Methods

Antibodies and chemicals used for this chapter can be found in the text or in **Table 2**.

Generation and cultivation of SC-ECs

HiPSCs (HMGUi001-A) were differentiated to SC-ECs in a 3D shaking culture approach as described before[31,144]. Successful differentiation was determined by flow cytometry analysis and staining for the EC marker CD31-FITC (BD, Cat#555445) and the smooth muscle cell marker CD140b-PE (BD, Cat#558821). For purification, SC-ECs were either FACS sorted (MACSTyto Cell Sorter, Miltenyi Biotec, according to manufactures protocol) or cultured on fibronectin-coated plates (Thermo Fisher, Cat#33010018, 5 µg/ml final concentration) leading to a SC-EC population of >90%. SC-ECs were cultured on fibronectin-coated plates in StemPro-34 complete medium (LIFE Technologies, see **Table 1**), with 15% FBS, VEGFA (PeproTech, Cat#10-20-100) and FGF2 (Miltenyi Biotech, Cat#130-093-838) (100 ng/ml each) with medium change every other day.

Table 1: StemPro-34 complete medium

REAGENT	FINAL CONCENTRATION	VOLUME
StemPro-34 medium	n/a	236 mL
StemPro-34 supplement	n/a	6.5 mL
L-Glutamine 200 mM	2 mM	2.5 mL
Penicillin-Streptomycin	1%	2.5 ml
Glutamax 100x	1x	2.5ml
Total	n/a	**250 mL**

Chip manufacturing

For the OoC production, chips were printed using an Asiga Pico 2 HD 3D printer and Pro3dure GR-10 resin (clear, transparent, Litholabs, Cat#HX10031). Slice thickness was set to 50 µm. As described before[145], the anti-aliasing method was used to compensate for errors in the 3D printed part by smoothening the chips channels to a round shape. After printing, channels were flushed with Isopropanol and chips were washed and ultrasonicated for 15 min in Isopropanol. After removing all uncured resin, chips were dried at 80°C for 30 mins and UV-flashed in an N_2 atmosphere with 2000 flashes on each side. For biocompatibility treatment, chips were incubated in 99% EtOH for 24 h and transferred to MilliQ water for 24 h. For the chip assembly, polyamide monofilaments (Cat#1005215; efco creative GmbH, Germany) were cut with a sharp scalpel and fed through the medium reservoirs and the gel chamber. The chip was bonded to a glass slide with a double-sided adhesive foil (ARcare, Cat#90445Q). To seal the chip, polydimethylsiloxan (PDMS, Mavom, Sylgard 184) was casted into the outer

chambers and cured for 15 min at 80°C. For sterilization, the chips were placed for 30 min under UV light prior to hydrogel filling.

Flow characterization

Microchannels were created in the OoC with a polypropylene filament of diameter 50 µm (Cat#CP05341A; SERAG-WIESSNER GmbH) and polyamide filament of diameter 150 µm and 250 µm (Cat#1005215, Cat#1005225; efco creative GmbH). 80 µL PBS were placed on top of the gels. 100 µL PBS with 0.1% 2.55 µm polystyrene particles (Cat#PS-F-B237-1; microParticles GmbH) were added to both sides of the chip. Chips were placed on a Zeiss AxioObserver at angles of 7°, 13°, and 25° to induce gravity-driven flow. Particle flow rates were recorded with a frame rate of 700 fps and exposure time of 1/20000 s for 5 seconds at 5, 30, 60, 120, 180 and 240 seconds after tilting. Buffer was allowed to level out on both sides before subsequent recordings. For cyclic measurements, chips were rotated every 2 minutes and particles were recorded 5, 30, 60 and 120 seconds after the start of every cycle. Recorded videos were analyzed in Fiji (ImageJ) using the TrackMate plugin[146] (v6.0.1) and flow rate measurements were exported to R (v4.2.0) for further analysis. Wall shear stress values (τ_w) were calculated using a derivation of the Hagen-Poiseuille equation, where µ is the dynamic viscosity of serum-free media (0.73 mPa.s[147]), U is the mean flow velocity and R is the radius of the lumen.

$$\tau_w = \frac{4\mu U}{R}$$

Cell seeding on chip

For cell seeding on chip, a collagen type I hydrogel (Corning, Cat#354236) was neutralized for pH=7.0 with the appropriate proportions of 10xPBS,1 mM NaOH and H_20 to obtain 2.5 mg ml^{-1}, mixed thoroughly and placed for 1 h on ice. Meanwhile, sterile chips were cooled down to -20°C. The collagen gel was filled into the gel chamber (40 µl/chamber) and polymerized for 40 min at 37°C. SC-ECs were detached with Accutase (Sigma, Cat#A6964) and concentrated to 4x 10^6 cells per ml for seeding. Cells were resuspended thoroughly and 30 µl were added to the inlet and outlet chambers. The filament was pulled out of the outlet chamber using forceps to introduce a gravitation-driven flow of cell suspension into the generated lumen. Chips were placed on a rocking shaker (OrganoFlow L, Mimetas) at a 10° angle and 6 rpm for 15 min. After initial seeding, EGM-2 (Sigma Aldrich, Cat#C-22011) medium with 1% penicillin/streptomycin (P/S) was added to all chambers (30 µl/chamber) (in the following EGM2 medium with 1% P/S is referred to as EGM-2). Chips for the flow condition were placed back on the shaker at a 25° angle and 2 min intervals. Chips were cultured under normal cell culture conditions at 37°C, 5% CO_2. Complete medium change was performed after 2 h and then every day (70 µl/chamber). The open microfluidic system allowed for high throughput

handling as the medium change takes less than 1 min per chip using a multistep pipette and using a cell culture pump for aspiration through a filter-less 100 µl tip.

Whole mount immunofluorescence staining

For whole mount staining on chip, cells were fixed with 4% paraformaldehyde (PFA) for 15 min at RT and washed with PBS afterwards. Samples were permeabilized with PBS + 0.1% Triton X-100 for 30 min at RT, washed with PBS-T (PBS + 0.1% Tween) and blocked for 2 h with blocking buffer (PBS-T, 10% FBS, 1% BSA, 0.1M glycine, 3% donkey serum). Chips were stained in blocking buffer without glycine for 2 days at 4°C (1:100). Primary antibodies were washed out thoroughly with PBS-T for 1 h before secondary antibodies were added (dilution 1:500). Secondary antibodies were incubated overnight at 4°C. Next, samples were washed with PBS-T and mounted in Vectashield (Biozol Diagnostica, Cat# VEC-H-1900-10) for imaging. Antibodies can be found in **Table 2**.

Table 2: Antibodies and chemicals used for the publication Stem-Cell Derived Vessels-on-Chip for Cardiovascular Research.

REAGENT or RESOURCE	SOURCE	IDENTIFIER
Antibodies		
AlexaFluor-488, donkey anti-mouse	Thermo Fisher Scientific	RRID: 141607
AlexaFluor-555, donkey anti-rabbit	Thermo Fisher Scientific	RRID: 162543
AlexaFluor-647, goat anti-mouse	Thermo Fisher Scientific	RRID: 2535809
Angiopoietin2, rabbit	Thermo Fisher Scientific	RRID: 2544773
ARP3, mouse	Sigma Aldrich	RRID: 476749
CD140b-PE	BD	RRID: 397132
CD31-FITC	BD	RRID: 395838
Claudin5, rabbit	Thermo Fisher Scientific	RRID: 2809891
Collagen IV, rabbit	abcam	RRID: 305584
DLL4, rabbit	Cell Signaling	RRID: 2800263
KLF4, rabbit	Thermo Fisher Scientific	RRID: 2898967
PECAM-1, mouse	Cell Signaling	RRID: 2160882
PECAM-1, rabbit	Thermo Fisher Scientific	RRID: 10981955
VE-Cadherin, rabbit	Cell Signaling	RRID: 2077970
ZO-1, mouse	Thermo Fisher Scientific	RRID: 2533147
Chemicals, recombinant proteins		
Accutase	Sigma Aldrich	A6964
BODIPY	Thermo Fisher Scientific	D3922
BSA 10%	Thermo Fisher Scientific	37525
Collagenase P	Roche	11213857001
DAPI	Sigma Aldrich	D9542
DiI-oxLDL	Thermo Fisher Scientific	L34358
DMEM/F12	Thermo Fisher Scientific	12634010
EGM-2	Sigma Aldrich	C-22011
FBS	Pan Biotech	P40-37500
FGF2	Miltenyi Biotec	130-093-838

Fibronectin	Thermo Fisher Scientific	33010018
FITC-dextran 2000 kDa	Sigma Aldrich	FD2000S
FITC-dextran 40 kDa	Sigma Aldrich	FD40S
GlutaMAX	Thermo Fisher Scientific	35050038
Hoechst33342	Thermo Fisher Scientific	62249
Live/Dead Viability/Toxicity Kit	Thermo Fisher Scientific	L3224
oxLDL	Thermo Fisher Scientific	L34357
Phalloidin-Atto-647	Abcam	ab176759
Pro3dure GR-10 resin	Litholabs	HX10031
StemPro-34	Thermo Fisher Scientific	10639011
TBHP	abcam	ab113851
TY52156	Sigma Aldrich	5330620001
VEGFA	Peprotech	100-20-250
Other		
Double-sided adhesive foil	ARcare	90445Q
Polypropylene filament	SERAG-WIESSNER GmbH	CP05341A
Polystyrene particles	microParticles GmbH	PS-F-B237-1

Histology of lumen sections

Generated vessels could be retrieved from the chip body by breaking the connecting structures of the insert with a scalpel. The hydrogel block was transferred to a well plate with tweezers, washed with PBS and fixed with 4% PFA. Paraffin embedding was initiated the same day according to standard procedures. 3 µm thick sections were stained with primary and secondary antibodies found in **Table 2**. Nuclei were identified with Hoechst 33342 (Thermo, Cat#62249). Fluorescence stainings were digitalized with an AxioImager 7 (Zeiss, Oberkochen, Germany) equipped with a 20x objective, and visualized with the Zeiss Zen Blue Software.

Confocal imaging

Wholemount stained vessels were imaged on a confocal microscope (Zeiss Axio Observer LSM 880, Zeiss Zen black software). For the sprouting analysis, images of VE-Cadherin and DAPI staining and brightfield PMT of the whole vessel including outgrowing branches were taken (20x magnification, 0,26 µm per pixel, 10 µm z-stacks). For visualization of COL1 fibers, blank microchannels were prepared, fixed, and imaged, profiting from label-free imaging via confocal reflection microscopy.

Permeability analysis

To test for endothelial barrier function, the vessels were perfused with 50 µl FITC-Dextran (500 µg/ml stock diluted 1:10 in PBS, 2000 kDa (Cat#FD2000S) and 40 kDa (Cat#FD40S), Sigma Aldrich) in the inlet chamber. Images were taken every 3 min for 20 min with an epi-fluorescent microscope (Zeiss Axio Observer Z1) using an automated imaging template for

the chip designed with the Zeiss Zen Blue software. For analysis, 3 lines transverse to the lumen were set through each captured image (**Figure 7**, h). Those lines were measured for signal intensity from left to right. Next, the signal intensities from left to right were plotted in a Jupyter notebook script. To consider for the vessel not being exactly centered in the middle of the image, the maximum of each curve was set as x=0. Then, all FITC-dextran intensities of all vessels from one condition could be mean-plotted into one curve.

Branching characterization and branch density analysis

For branch analysis, z-stacks from VE-Cadherin-stained confocal images defined as "only covering lumen bottom" were converged to a 3D-projection in Fiji. 3D-stacked images were batch-filtered in Fiji (i.e. CLAHE, Otsudark auto-threshold, median filter, binarized). For branching characterization, Fiji's "skeletonize 2D/3D" and "Analyze skeleton 2D/3D" tools were applied on filtered and binarized images (Figure S2b). For density analysis, filtered and binarized images were measured for signal density (as a percentage of black over white signal) using a MATLAB script. Signal intensities of longitudinal lines were measured, which were directing with a distance of 1 µm from each other from the central lumen towards the periphery branches. For each parallel line a mean signal intensity was measured, and those mean intensities could then be plotted in dependence on their distance from the central lumen resulting in the signal density plot. The output data of skeleton and density analysis were further processed in Python.

Live dead cell analysis

SC-ECs cultivated under flow were stained on day 2 with Live/Dead Viability/Toxicity Kit (LIFE Technologies, Cat#L3224) as described in the manufacturer's protocol. Stained vessels were imaged on an epi-fluorescence microscope (Zeiss, Zen software). For image analysis, signal intensities were normalized to an auto-threshold and a StarDist segmentation FIJI plug-in[148] was applied to detect live and dead cells. The mean signal threshold for both markers were set to 3000 and the mean area threshold to 50 µm².

NO assay

For measuring the NO production in SC-ECs, the fluorometric Nitric Oxide Assay Kit (Sigma, Cat#482655) was used according to the manufacturer protocol. The assay is based on the enzymatic conversion of nitrate to nitrite so that the total amount of nitric oxide in the supernatant can be analyzed. For each condition a respective background control was carried along and background fluorescence was subtracted after measurement. For normalization, cells were extracted from the chip and counted as described in the following paragraph.

Sample preparation for single-cell RNA sequencing (scRNAseq)

For scRNAseq, chips were washed with PBS. To ensure that only cells growing in the hydrogel were collected, inlet and outlet ports were blocked with 3% agarose. After solidification of the agarose, cells were treated with a 1:1 mix of Collagenase P (18 U final concentration, Roche Cat#11213857001) and Accutase and incubated for 30 min at 37°C. Pipette tips and tubes were washed with PBS + 2% BSA (Thermo Scientific, Cat#37525) before usage to reduce cell loss. Successfully dissolved hydrogels and a single cell suspension was confirmed under the microscope before harvesting the cells in PBS + 10% FBS. The cells were centrifuged at 300 x g for 3 min, washed with PBS + 2% BSA and filtered with a 20 µm cell Pluristrainer (pluriSelect, Cat#43-50020-023). Cells were counted with TrypanBlue (Sigma, Cat#T8154) and a cell vitality of over 70% was confirmed. RNA libraries were generated using Chromium Single Cell 3' library and gel bead kit v3.1 (10x Genomics, Cat#1000269 and #1000127). The amplified cDNA library was sequenced on a NovaSeq SP flow cell from Illumina.

Pre-processing of scRNAseq data

Raw sequencing data files were demultiplexed, aligned (reference genome hg38_ensrel96), filtered, barcodes and UMIs counted, and subjected to a quality filter with CellRanger (10xGenomics). The pre-processing and downstream analysis were performed with the package Scanpy[149] in python with default parameters, if not stated differently. Cell-ranger processed data from static and flow conditions were first concatenated. Next, dead or stressed cells, identified by a percentage of mitochondrial genes higher than 15%, were filtered out. Cells with less than 3000 or more than $6x10^4$ total counts or cells with less than 200 expressed genes were excluded. Also, genes expressed in less than 10 cells were rejected. Afterwards, gene counts were normalized to 10^4 per cell and log transformed. Additionally, cell cycle genes and mitochondrial genes were regressed out. Doublets were detected with the Scrublet package[150] and filtered.

Clustering and cell type annotation

The single-cell neighborhoods were calculated with the first 30 principal components and 10 nearest neighbours and the cells were clustered with the Leiden algorithm[151] at a resolution of 0.5. For visualization, UMAP[152] was used to reduce dimensionality of the data. Cell types were annotated by ranking the top 25 marker genes of each of the 7 Leiden sub-cluster based on literature research. Correlation plots confirmed similarity of subclusters. Cell type proportions and gene expression analysis were performed based on the defined categorical clusters.

RNA velocity using basic modelling

To investigate developmental trajectories in the flow sample, we analyzed the RNA velocity by recovering directed dynamic gene information through splicing kinetics in basic mode

following the scVelo[153] standard pipeline. Variables and observations, like cluster annotation and UMAP coordinates were accessed from the Scanpy analysis as described above. The splicing matrix was generated by default settings of the velocyto[154] pipeline. After concatenating splice matrix and scanpy information, splice variants and cells were filtered, normalized, and logarithmized with the function scv.pp.filter_and_normalize (shared_counts=20, n_top_genes=2000). In a next step, the moments, based on the connectivities, were calculated with 30 PCAs and 30 neighbors. Then, velocities and the based root cell were assessed by the sc.velo algorithm and represented in an UMAP embedding stream projection.

Cell treatment for oxidative stress induction

ECs were seeded and cultured under flow for 1 day as described above. For oxidative stress induction, either 50 µg ml^{-1} oxLDL (life technologies, Cat# L34357) or 800 µM FFA-BSA mixture was added to EGM2 medium from day 1 to day 2. A FFA stock was prepared in advance consisting of a mixture of different fatty acids dissolved in ethanol: c14:0 (1.05%), c16:0 (26.75%), c18:0 (8.04%), c18:2 (36.63%), c18:1 (21.09%) and c20:4 (6.44%); all from Sigma) as described in Bondareva, et al.[155]. These candidates are a selection of the most common FFA in human serum and the chosen percentual combination was measured in human serum[156]. For FFA-BSA treatment solution, an 8 mM stock solution was generated by conjugating the fatty acids to fatty acid-free BSA (Sigma). Therefore, a mixture of BSA, FFA and high-grade Ethanol (9: 0.8: 0.2) was incubated for 2h at 37°C and 1500 rpm. On day 2, the EGM2 was replaced by serum free medium (DMEM/F12 + Glutamax +1% P/S) and the treatment was continued until day 3. On day 3, supernatants were collected for secretome analysis and immediately frozen and stored at -80°C. Afterwards the chips were washed four times for 1h with PBS, inlet and outlet ports were blocked with 3% agarose and hydrogels were digested in a 1:1 mix of Collagenase P and Accutase. Cells were collected, washed three times with PBS and pelleted. Lysates were stored at -80°C until mass spectrometry preparation. Medium and untreated cell samples were carried along as controls. As the FFA treated sample contained BSA, the control was treated with a BSA-Ethanol-vehicle control.

Sample preparation and mass spectrometry measurements

Lysate pellets were prepared for mass spectrometry (MS) measurement as described in Compera et al.[157]. Supernatants were digested enzymatically using the PreOmics' iST Kit (Preomics GmbH, Martinsried, Germany) including the SP3 add-on kit according to manufacturers' specifications with adjustment of volumes for the SP3-lyse and -binding buffers to fulfill 1x concentration of buffers. After drying, the peptides were resuspended in 2% acetonitrile (ACN) and 0.5% trifluoroacetic acid. The HRM Calibration Kit (Biognosys, Schlieren, Switzerland) was added to all the samples according to the manufacturer's

instructions. MS measurement was performed in data dependent (DDA) mode. MS data were acquired on a Q Exactive (QE) high field (HF) mass spectrometer (Thermo Fisher Scientific Inc.) as described in Hladik et al[158].

Data processing - protein identification

Proteome Discoverer 2.5 software (Thermo Fisher Scientific; version 2.5.0.400) was used for peptide and protein identification via a database search (Sequest HT search engine) against Swissprot human data base (Release 2020_02, 20432 sequences), considering full tryptic specificity, allowing for one missed tryptic cleavage sites, precursor mass tolerance 10 ppm, fragment mass tolerance 0.02 Da. Carbamidomethylation of Cys was set as a static modification. Dynamic modifications included deamidation of Asn, Gln, oxidation of Met; and a combination of Met loss with acetylation on protein N-terminus. Percolator was used for validating peptide spectrum matches and peptides, accepting only the top-scoring hit for each spectrum, and satisfying the cutoff values for FDR <1%, and posterior error probability <0.05. The Sequest HT Xcorr filter was set to 1.6 removing identifications below this threshold. The final list of proteins complied with the strict parsimony principle.

Data processing - label-free quantification

Proteins were quantified based on abundance values for unique peptides. Abundance values were first normalized to the total amount of peptides in each sample to account for sample loading errors. The protein abundances were calculated summing up the abundance values for admissible peptides. The final protein ratio between experimental groups was calculated using median values of single peptide ratios per comparison. The statistical significance of the ratio change was ascertained employing the t-test method described in Navarro et al[159]. Adjusted p-values are calculated according to Benjamini-Hochberg.

Data analysis

In the following downstream analysis, only proteins with more than one unique peptide hit were used. Differential protein expression (DEP) analysis was performed with customized Python (version 3.10) scripts using the adjusted p-values (p.adj < 0.05) and normalized abundance ratios (ratio > 1.5). Differently expressed proteins were only taken into account, when abundances were measured in at least 75% of the replicates within their group. In addition, the secretome data was filtered for actively secreted proteins matching the DEP against the refined human secretome[160]. Only proteins with the labels “blood secretion” were used. Enrichment analysis and Go term identification was performed using the STRING[161], gprofiler[162] and Enrichr[163] databases and customized Python scripts from GitHub repository xDbit[164] (https://github.com/MeierLabMiBioEng/xDbit_toolbox).

Oxidative stress compound staining

For staining of FFA accumulation, vessels were fixed on day 3 as described above, washed with PBS and incubated with BODIPY (4,4-difluoro-1,3,5,7,8- pentamethyl-4-bora-3a, 4a-diaza-s-indacene, Thermo, Cat#D3922) in a final concentration of 10 µg ml^{-1} in PBS, together with DAPI (Thermo, Cat#D9542, 1:100) and Phalloidin-Atto-647(Cat#ab176759, 1:200). For staining of oxLDL accumulation, vessels were treated as described for the oxLDL treatment with Dil-labelled oxLDL (Thermo, Cat#L34358) for 3 days. After fixation, vessels were stained with DAPI and Phalloidin-Atto-647 as described above. For detection of oxidative stress in cells, lumens were stained with green fluorescent CellROX (Sigma, Cat#C10444). Vessels were washed 3 times in PBS, before CellROX was added in a final concentration of 5 µM in PBS together with Hoechst33342 (Thermo, Cat#62249, 10 µg ml^{-1}) and incubated for 1h at 37°C in an incubator. After staining has been completed, vessels were fixed as described above and imaged with a confocal microscope under the same settings for all conditions. For a positive control, vessels were treated with 100 µM TBHP (abcam, Cat#ab113851). For image analysis of CellROX signal, for each capture a z-stack consisting of 6 slices with distance of 6 µm was converted to one stacked image by 3D projection in FIJI. Then, Stardist[148] segmentation program was applied comparable to the live-dead staining. The mean signal intensity was set to 5 and the mean area threshold were set to 5 $µm^2$ for both the DAPI and CellROX channel. For later analysis in a Python script, fragmented, apoptotic, and highly bright nuclei were further filtered, setting an area threshold of 60 $µm^2$. Due to technical-related differences in DAPI and CellROX staining intensities, for each image the CellROX signal intensity was normalized to its corresponding DAPI signal intensity, resulting in a normalized CellROX/DAPI intensity ratio for each image.

Quantification and statistical analysis

Statistical analysis was performed using the scipy.stats[165] function with custom-written python code. Statistical details of experiments and numbers of replicates can be found in the figure legends. Data was tested for normal distribution with the Shapiro test and for homogenous variances with the Levene or Bartlett test. Statistical significance between groups was tested with a pairwise t-test for two conditions and with a one-way ANOVA for multiple sample groups followed by a Tukey's post-hoc test.

3.4 Results

Design and characterization of the open organ-on-chip platform

The main body of the open organ-on-chip (OoC) platform was produced using 3D stereolithography printing and bonded to an adhesive foil on a glass substrate (**Figure 6**, a). Each chip exhibited 6 arrayed unit cells, where each unit cell contained a hydrogel chamber and two fluid reservoirs, each holding an adjustable volume between 30–150 µL. Relevant chip dimensions are shown in Figure S1a. The gel chamber was connected to the fluid reservoirs using short microfluidic channels with a diameter of 350 µm on each side. Through the connecting channel, a nylon filament with a diameter between 50 and 250 µm can be introduced. The hydrogel chamber was filled with hydrogel prepolymers to encapsulate the nylon filaments. Upon removing the nylon filament through one of the fluid reservoirs, the hydrogel was patterned with a straight microfluidic channel (**Figure 6**, b and c). The resulting microchannel width in the hydrogel slightly differed from the nominal diameters of the nylon filaments. However, the microchannels were robustly patterned for nylon filaments with diameters of 50, 150, and 250 µm (Figure S1b). The gel chamber contained a scaffolding structure with four poles connected by a top ring to stabilize the hydrogel over longer culture times. The pole structure is connected to the main body of the chip using rated breakpoints. Upon detaching the pole structure from the main chip body, the hydrogel with the embedded tissue can be retrieved for downstream analytical sample preparation, such as histology. The two outer reservoirs fluidically communicate through the microchannel; thus, the addition of fluids within one reservoir leads to gravity-driven flow and fluid leveling through the communicating channel. However, the two outer fluid reservoirs not only equalize the hydrostatic pressure, but the hydrogel chamber also contributes to filling height homeostasis owing to the open microfluidic design. One consequence is that the hydrostatic pressure difference resulting from non-equalized fluid volumes in the reservoirs and hydrogel chamber leads to the dilation of the microfluidic channel because the hydrostatic pressure acts on the gel phase (**Figure 6**, d-f). The dilation of the microchannel depends on the mechanical properties of the hydrogel. Representatively, we show the dilation of a 150 µm microchannel used by default within a collagen-I (COL1) hydrogel with increasing COL1 concentration. While imbalances of fluid filling heights between the reservoir and the gel chamber have a strong effect on the microchannel width in the low concentrated COL1 hydrogel (1.25 mg ml^{-1}), imbalances of the fluid filling heights within the higher concentrated COL1 hydrogel (5 mg ml^{-1}) have lower effects on the microchannel width (**Figure 6**, g). The chip can be placed on a rocking shaker to induce gravitational flow on it; thus, no active pump system is required to maintain the cell cultures under flow conditions (**Figure 6**, h). To quantify the wall shear stress

(WSS), we assessed the flow velocity as a function of the tilt angle of the chip by tracking the motion of microbeads within video frames (**Figure 6**, i and see Methods). The determined WSS for a nominal 150 µm channel within 2.5 mg ml^{-1} COL1 hydrogel with tilting angles of 7°/13°/25° are exemplarily shown in Figure S1c. As expected, the WSS increased with higher tilt angles, and the flow rates decreased over time because of the leveling of the filling heights between the reservoirs. As the maximum flow rate of 15 µl min^{-1} on-chip was achieved at a tilting angle of 25°, this tilting angle was set as the default for all experiments. After tilt initiation, half of the maximum WSS was observed after 2 min (**Figure 6**, j). This time was used as the frequency for changing the tilt direction and maintaining the bidirectional flow. Using three different nylon filaments with diameters of 50 µm, 150 µm, and 250 µm, the effect of the microchannel diameter on the flow rates and WSS was subsequently investigated (Figure S1d, e). A maximum volumetric discharge of 15 µL min^{-1} was calculated at 150 µm diameter in the center of the microchannel at a 25° tilt (Figure S1d). Increased microchannel diameters resulted in a greater maximum WSS but a faster reduction in WSS over time (Figure S1e). Microchannel diameters of 150 and 250 µm produced shear forces in the range of 1 to 3 dyn cm^{-2}, whereas a microchannel diameter of 50 µm produced negligible shear forces. In the following experiments, we used only chips with a 150 µm diameter and a maximum tilt of 25° inducing a shear force of 3 dyn cm^{-2}, which is at the lower end of the shear force microvessel experience *in vivo*[166].

.

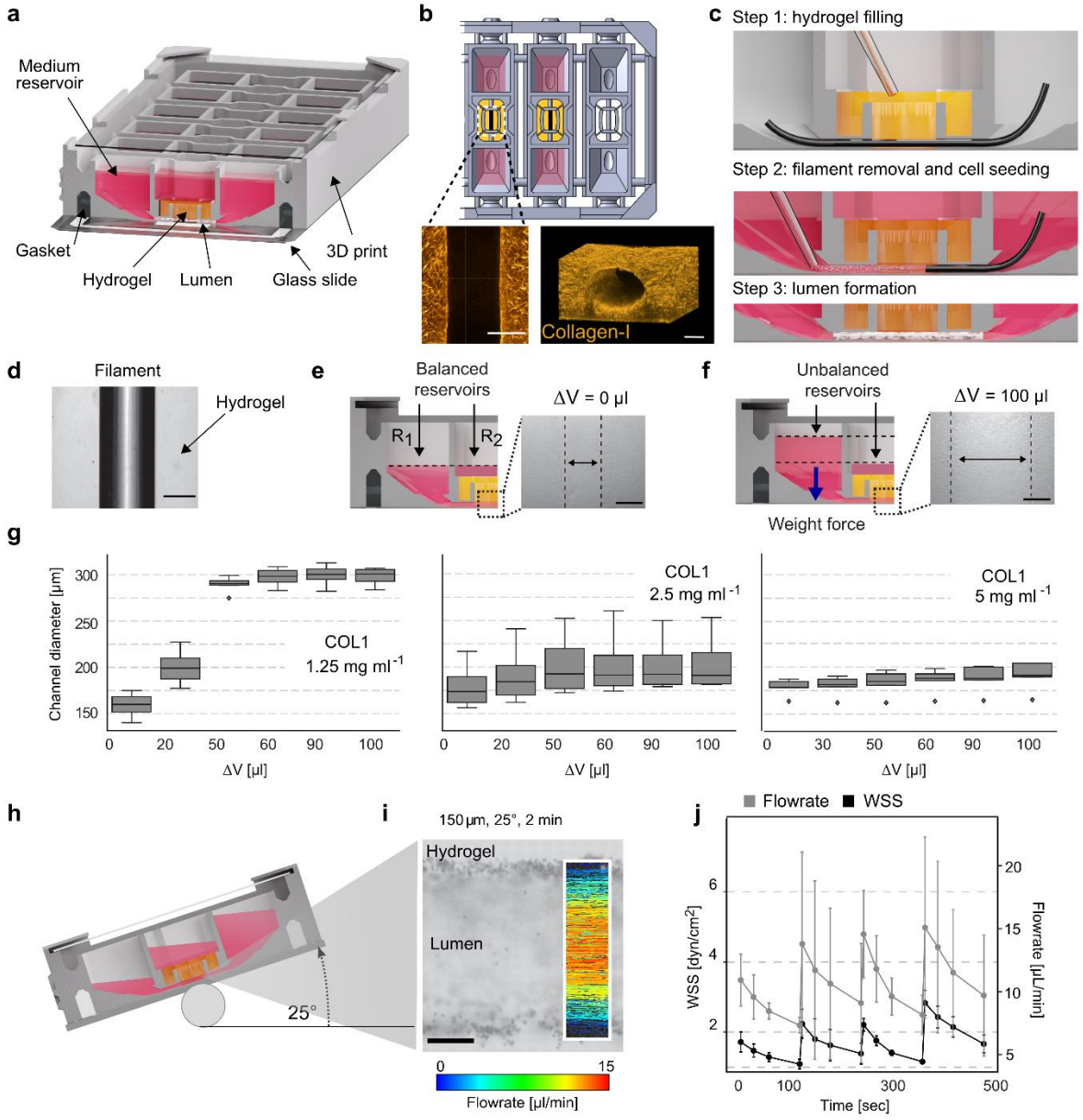

Figure 6: The open microfluidic chip platform for organotypic cell cultures. a Cross-sectional view of the 3D-printed chip. The chip holds six identical unit cells, where each unit cell has two reservoirs connected by a hydrogel chamber for tissue culture formation. **b** Top view of the chip. Zoom-in images show confocal laser reflection images (488 nm) of the Collagen I (COL1) hydrogel chamber (5 mg ml^{-1}) with the patterned microfluidic channel. The microchannel runs 100 ± 10 µm above the glass substrate and connects the two fluid reservoirs. Scale bar, 150 µm. **c** Manufacturing steps of the microchannel. Step 1: A nylon filament is introduced to the chip before filling and polymerization of the hydrogel solution in the middle chamber. Step 2: A cell suspension is pipetted into the reservoirs. Upon mechanical removal of the filament through the reservoir, cells are dragged into the microchannel. Step 3: Cells are cultivated and allowed to form tight endothelial structures. **d** Image of a nylon filament with a diameter of 150 µm in a 2.5 mg ml^{-1} COL1 hydrogel. Scale bar, 100 µm. **e** and **f** images of reservoirs and hydrogel chamber with balanced and unbalanced fluid volume. Within the open microfluidic chip design, the microfluidic channel in the hydrogel widens depending on the hydrostatic pressure acting on the microchannel. Scale bar, 100 µm. **g** Box plots show the dilation of the microfluidic channel depending on the COL-1 concentration and volume differences in the reservoirs and hydrogel chamber. Error bars indicate confidence intervals of

95%. **h** Gravity-driven flow is enabled by tilting the chip platform. **i** Flow rates within a microchannel with a nominal diameter of 150 µm were determined by video tracking the microbeads. The representative velocity profile within the microchannel is provided for the maximum tilting angle of 25°. Scale bar, 50 µm. **j** Flow rates on the chip are not constant due to fluid leveling over the reservoirs. The graph shows the time-dependent changes in the flow rates and mean wall shear stress (WSS) inside the microchannel at tilt angles of 25°. The tilting angle was reversed every 2 minutes to maintain a bidirectional gravity-driven flow. Error bars indicate standard deviation.

Formation of the functional perfused endothelial vessel on chip

Next, we applied the chip for the formation of SC-EC *in vitro* vessel structures. Using a two-step induction protocol for ECs, hiPSCs were differentiated in 3D shaking culture[31]. SC-ECs were expanded and seeded at high density (4 Mio. cells ml^{-1}) into the chip with a pre-formed microchannel in a 2.5 mg ml^{-1} COL1 hydrogel (**Figure 7**, a). The cells began to adhere to the channel walls within the first hour. Within the following two days, cells were cultivated under either static or bidirectional flow conditions. In both cases, SC-ECs formed a luminal vessel structure adopting the shape of the microchannel, with sprouts developing towards the hydrogel periphery after 2 days of cultivation (**Figure 7**, b and Figure S2a).

We analyzed the sprouting network parameters within 3D-stacked confocal images in which VE-cadherin was immunohistochemically stained to quantify the differences in endothelial sprouting capability under static or flow conditions (Figure S2b). Notably, SC-ECs under flow conditions formed more branches protruding from the lumen regarding the total number, junctions per branch, and total network length (**Figure 7**, c-e) than under static conditions. This higher sprouting behavior was further confirmed by fluorescence signal analysis using VE-cadherin staining (**Figure 7**, f). The VE-cadherin signal along the perpendicular axis of the microchannel showed a higher amplitude and length, which represented a higher number and longer sprouts within the samples cultured under flow conditions.

Sprouting analysis indicated that ECs interacted with the extracellular matrix (ECM) and started to remodel the surrounding hydrogel via sprouting angiogenesis. COL1 is one of the most abundant ECM proteins and is a favorable hydrogel for constructing *in vitro* blood vessels[167]. We demonstrated the extent to which the hydrogel formula influenced cellular hydrogel remodeling and sprouting by seeding SC-ECs on a chip at different COL1 concentrations. At the lowest COL1 concentration (1.25 mg ml^{-1}), the cells visibly remodeled the microchannel by sprouting out of the lumen towards the ECM periphery, leading to significant lumen enlargement. By contrast, at higher concentrations (2.5 and 5 mg ml^{-1}) the lumen diameter was less impaired (Figure S2c). At a collagen concentration of 5 mg ml^{-1}, only a few sprout tips were observed. This suggests that denser collagen networks promote lumen stability while impeding the growth of the SC-EC branches. Hereafter, all experiments were

performed with a COL1 concentration of 2.5 mg ml^{-1} to maintain the lumen structure and sprouting capability of the SC-ECs. A FITC-dextran assay was performed to test the barrier function of the endothelial lumen. The SC-EC lumen engineered under flow conditions showed higher resistance to FITC-dextran diffusion (40 and 2000 kDa) over the endothelial barrier into the COL1 hydrogel matrix than the SC-EC lumen engineered under static conditions over three days (**Figure 7**, g and h and Figure S2d).

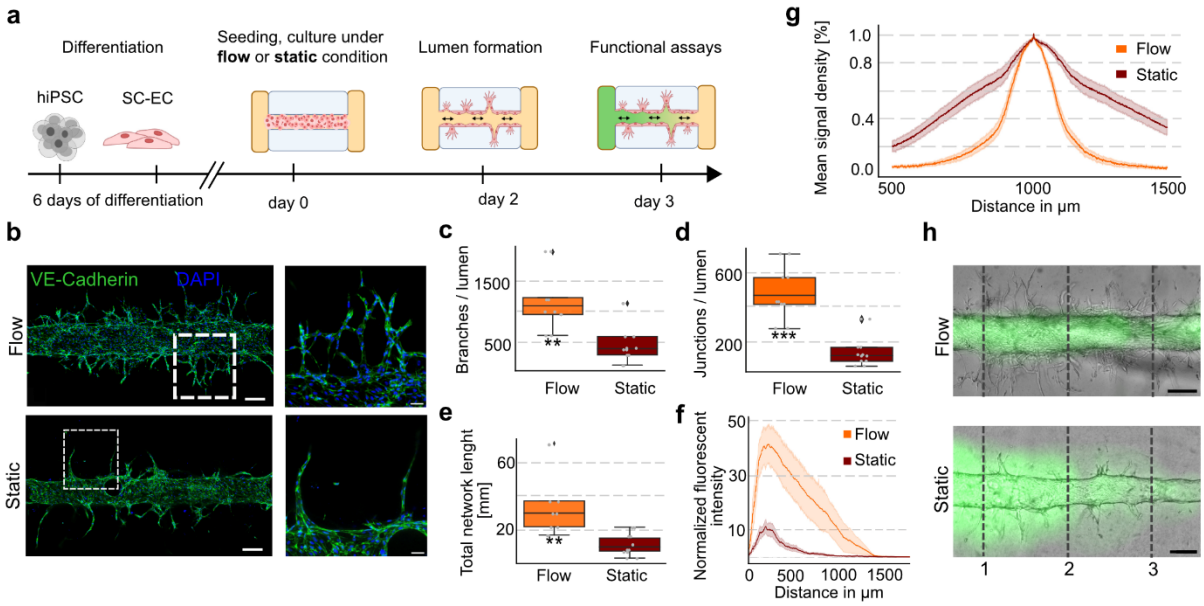

Figure 7: Formation of a functional perfused endothelial vessel on-chip displaying barrier integrity and sprouting angiogenesis. a Experimental outline: stem cell-derived endothelial cells (SC-ECs) were differentiated from human induced pluripotent stem cells (hiPSCs) and seeded in the chip. Functional tests such as *in vitro* vessel integrity test by infusing the lumen with fluorescently labeled fluorescein isothiocyanate (FITC)-dextran were performed after 2 days. **b** Immunofluorescence images of vascular endothelial (VE)-cadherin (EC contact integrity) of 2 days cultured SC-EC under bidirectional flow or static conditions on-chip. Scale bar, 200 µm left and 100 µm right. **c-e** Sprouting network analysis of the SC-EC under bidirectional flow and static conditions showing branches (**c**) and junctions (**d**) per lumen and total vascular network length (**e**) (n=6 from 2 independent experiments; *p* values were calculated using a two-sided t-test and indicated in the figure; error bars indicate a confidence interval (CI) of 95%). **f** Sprout density was measured using the mean intensity of the VE-cadherin signal on multiple longitudinal axes directing from the outer wall of the microchannel towards the hydrogel area (n=6 from 2 independent experiments, CI=68%). **g** FITC-Dextran assay to evaluate the barrier function of SC-EC vessels. The mean fluorescence intensity signal of FITC-dextran was measured on 3 traverse lines scans per lumen (dotted lines in **h**) (n=8 from 3 independent experiments, CI: 68%). **h** Images are fluorescence and brightfield overlays, where green denotes the FITC-Dextran signal. Scale bar, 200 µm.

Single-cell transcriptomic and functional analysis of the SC-EC on-chip

Next, we performed single-cell transcriptomic analysis (scRNAseq) of SC-EC cultured on-chip under shear flow and static conditions to reveal the heterogeneity of cell stages associated with possible maturation, sprouting, or barrier function (**Figure 8**, a). We obtained sufficient SC-EC for the scRNAseq protocol by pooling the SC-EC from one chip, which are 6 functional lumens with approximately 3000 cells each. The live cell recovery rates from the chip were >70% for SC-ECs cultured under flow conditions, demonstrating that the retrieval process was robust. For SC-ECs cultured under static conditions, the live cell recovery rates were lower, indicating a lower viability or higher stress state of these cells (Figure S3a, b). Cells retrieved from the chip were used as inputs for scRNAseq. The quality parameters of the sequencing run are shown in Figure S3c-g. After high-quality scRNAseq data filtering, we obtained single-cell transcriptomes of >17k genes from approximately 2000 cells (Figure S3d) under both conditions. Seven cell clusters were identified using Leiden[168] clustering (resolution = 0.5) and two-dimensional data reduction (UMAP[169]) of the single-cell transcriptome data (Figure S4a). The Leiden clusters were annotated as flow, static, intermediate, barrier, filopodia-like 1/2, and mural cell-like transcriptomic states based on the marker genes (**Figure 8**, b, c and e; Figure S4b, c). Notably, only the mural cell-like cell cluster did not express the EC markers and showed typical vascular smooth muscle cell marker expression, including that of *PDGFRB, CSPG4, TAGLN*, and *ACTA2*[170]. Others and we have previously shown that ECs and mural-like cells co-evolve during the applied stem cell differentiation protocol[31,171] and that progenitors are still present on day 6 of differentiation. A low fraction of mural-like cells may have resulted from incomplete sorting. The differentially expressed genes (DEGs) for SC-EC cultured under static conditions included the EC markers, such as *EDN1* or *ANGPT2*, which are specific for static SC-EC culture conditions since shear flow stress leads to their downregulation[135,172]. Furthermore, cells from the static cell cluster shared the expression of stress marker genes, including *ROMO1* and *NQO1*, indicating oxidative stress and cell death[173]. Contrastingly, only 19% of the single-cell reads found in the SC-ECs exposed to wall shear stress were allocated to the static cluster, whereas 39% of the statically cultured SC-ECs were allocated to the static cluster (**Figure 8**, d). SC-EC distribution cultured under flow and static conditions within annotated cell clusters is shown in **Figure 8**, d. Under flow culture conditions, half the SC-EC population exhibited transcriptomic states of either intermediate (23%) or flow (25%) cell clusters. Furthermore, cells from the flow cluster showed upregulated expression of shear stress markers, including *KLF2, KLF4*[135], or *VWF*[174]. Notably, *GJA4* is a shear stress-upregulated gene that enables arterial specification together with the downstream cell cycle inhibitor *CDKN1B*[175], which is also specifically upregulated in the flow cell cluster. This is in line with *MECOM* upregulation in the flow cluster, a regulator of human arterial gene expression[176].

Intermediate clustered cells upregulated the expression of *MMP9*, which is a shear stress-sensitive gene[177] and central for the initiation of angiogenesis in the endothelial progenitors[178]. Cells of the intermediate cluster also express the pro-oncogene *JUN*, which is upregulated in the ECs as an immediate response to shear stress[179]. Approximately 7% of the SC-EC in both static and flow culture conditions were assigned to one of two filopodia-like transcriptomic cell states. Filopodia cluster 1 was positive for VEGF/calcium signaling, and filopodia cluster 2 was correlated with NOTCH and ECM-receptor interaction as revealed by a Kyoto Encyclopedia of Genes (KEGG) pathway analysis (Figure S4c). A representative selected DEG for filopodia cluster 1 was transforming growth factor beta 1 (*TGFB1*), which is known to induce angiogenesis[180]. Coherently, *PEAK1*[181] was a unique marker for filopodia-like 2. SC-EC within the barrier cluster upregulated the expression of cell–cell interaction genes (*CLDN5* and *ENG*) as well as gap and tight junction genes (*GJA1* or *JAM3*), which indicated the formation of a cell–cell interaction required for intact lumens[182,183]. Cells from static and flow culture conditions were found in the barrier cluster, suggesting that the prepatterned luminal shape of the hydrogel alone was sufficient for the formation of the transcriptomic cell state. KEGG pathway analysis and Pearson correlation plots supported the annotation and differences in all transcriptomic states, respectively (**Figure 8**, f and Figure S4c).

RNA velocity[184] was calculated using the scRNAseq flow data to resolve the dynamic changes and interconnectivity of cell clusters (**Figure 8**, g). The flow velocity lines point from the static cluster towards the intermediate, barrier, flow, and filopodia-like clusters. Next, we investigated whether the velocity lines indicated SC-EC maturation under flow culture conditions. To this end, we calculated the gene enrichment scores for DEGs obtained from embryonal and adult human endothelial single-cell datasets within the SC-EC single-cell transcriptome data. Strikingly, the DEGs of the embryonic early arterial (Carnegie stage 10 and 11)[185] and the adult artery ECs (human sc-RNA atlas)[186] considerably increased along the velocity lines (**Figure 8**, h), thus supporting the maturation effect of SC-ECs under shear flow culture conditions. The gene enrichment score for DEGs of adult lymphatic ECs also increased within SC-EC cultured under shear flow conditions, however to a lower degree arguing that the on-chip conditions drive cell type maturation towards an arterial-like cell type. Similarly, cells of the mural cell cluster correlated with the transcriptomes assigned to the adult smooth muscle cells. Contrarily, the enrichment analysis showed that SC-EC on-chip did not resemble embryonic cardiac ECs.

Moreover, in the flow, intermediate, barrier, or filopodia clusters the expression profile of ECM proteins changed compared to cells cultured under static conditions (Figure S4d). For example, barrier cells increased the expression of the basal membrane protein Collagen IV also found by IF stained lumen sections (Figure S4e).

Shear stress is known to be a positive regulator of endothelial NO-synthesis[172]. Genes involved in NO signaling belonged to the DEG of the single-cell flow clusters. Vascular cells synthesize NO to maintain healthy tissue function and to control vasodilation[187]. Nitric oxide synthase (*NOS3*) and the NOS3 activating Ca-dependent protein kinase (*CAMK2D*) are upregulated in ECs cultured under flow conditions[188]. Contrastingly, under static cell culture conditions, ECs upregulated genes, such as eNOS interacting proteins (*NOSIP*), eNOS traffic inducer (*NOSTRIN*), and Caveolin-1 (*CAV1*), which form a ternary complex inhibiting eNOS activity[187] (**Figure 8**, i). We determined NO concentrations in the supernatants of the perfused lumens cultured under flow and static conditions using a fluorometric assay to validate the gene expression changes at the functional level. Indeed, NO production was significantly increased in the ECs cultured under flow conditions, whereas NO concentrations in the EC cultured under static conditions were comparable to those in cells grown in a 2D monolayer (**Figure 8**, j).

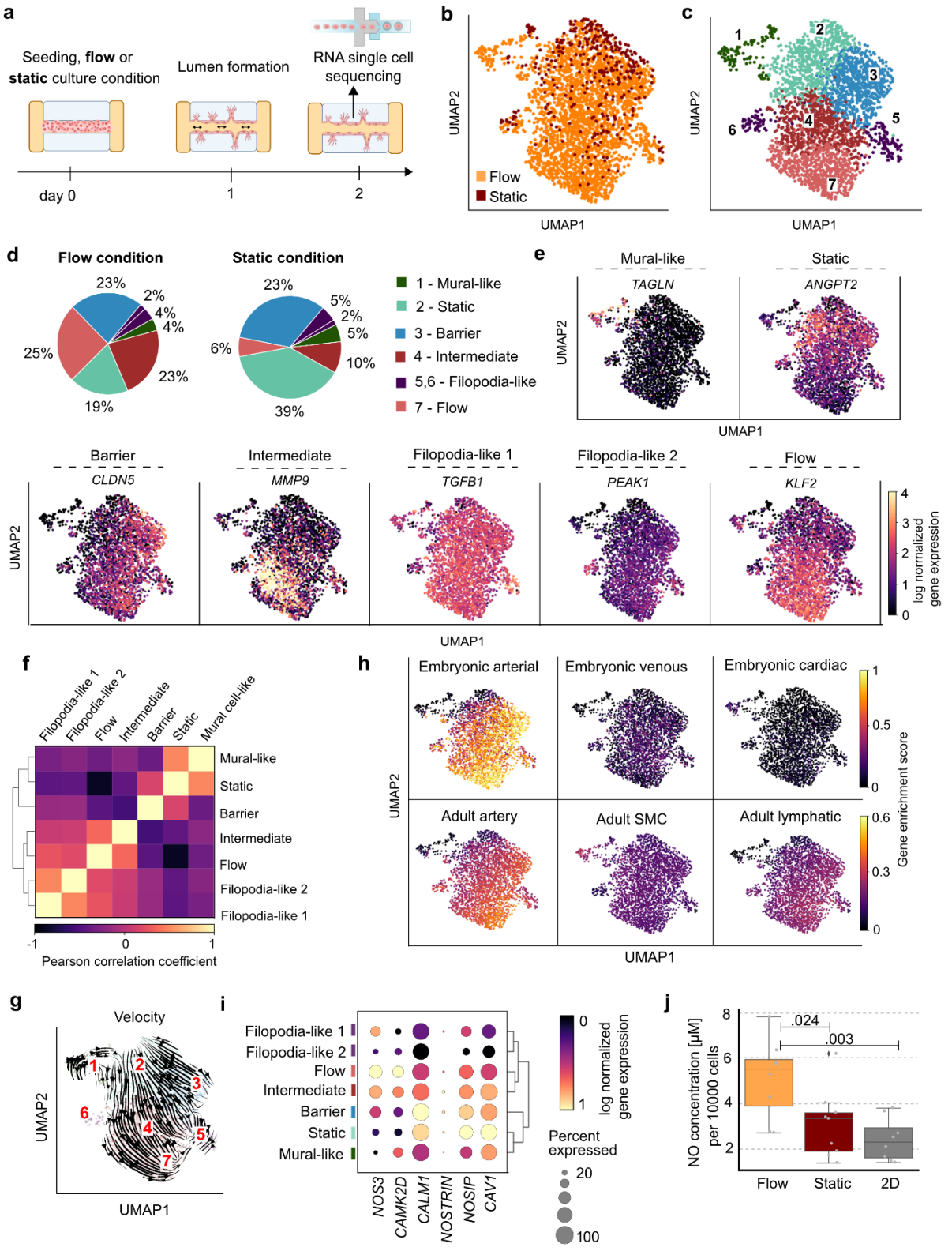

Figure 8: Single-cell transcriptomics reveal specified flow-induced cell clusters reflected by enhanced nitric oxide synthesis in *in vitro* conditions. **a** Experimental outline: stem cell-derived endothelial cells (SC-ECs) cultured for 2 days under bidirectional flow or static culture conditions on-chip. Cells were retrieved from the chip and used for 10x genomics single-cell RNA sequencing. **b** Uniform manifold approximation and projection

(UMAP) plot of the two acquired single-cell transcriptomic data sets. **c** UMAP plot illustrating the seven unique found transcriptomic cell clusters for the SC-EC cultured on-chip. **d** Cell distribution according to the identified cell clusters. **e** Gene expression patterns of the selected cell marker genes used for cell cluster assignments. **f** Pearson correlation plot of the annotated cell clusters. **g** Single-cell transcriptomic velocity analysis. Velocity streamlines showed the transcriptomic state progression of SC-ECs cultured for 2 days under bidirectional flow on-chip. **h** Enrichment score of DEGs from embryonic arterial, venous, and cardiac ECs (human embryonic dataset at Carnegie stage 10 and 11) and of adult artery ECs, smooth muscle cells, and adult lymphatic ECs (Tabula Sapiens organ type vasculature dataset) within the on-chip scRNA dataset. **i** Dot plots show expression levels of genes required for endothelial nitric oxide (NO) synthesis (*NOS3, CAMK2D, CALM1*) and inhibition of the NO synthesis (*NOSTRIN, NOSIP, CAV1*). **j** NO concentrations within the luminal cell culture media of the chip from cells cultured under flow or static conditions. NO concentrations are compared to supernatants of cells grown on a 2D monolayer (n=8-9 repeats from 3 independent experiments; error bars indicate CI of 95%). NO concentrations were normalized to the total cell count per sample. *P* values were calculated with a one-way ANOVA and Tukey's post-hoc test and are indicated in the figure.

Interfacing the vessel-on-chip platform for downstream analysis

The open OoC platform was designed to enable high-resolution imaging. A working distance of 100 µm between the microchannel and the glass substrate allowed whole-mount imaging of the SC-EC vessel structure (**Figure 9**, a, b). Therefore, immunofluorescence staining can be performed with a low antibody consumption. We stained for the sprouting marker DLL4 and lamellipodia marker ARP3. Lamellipodia appeared at plasma membrane sites free of VE-cadherin as reported before[189] and ARP3 expression was observed in the cell membrane regions next to newly formed sprouts. Alternatively to the whole mount staining, sample sections can be prepared for multiple protein detections in a single lumen. For this, the COL1 hydrogel was retrieved in an unscathed manner by lifting the hydrogel-embedded 3D printed support structures (**Figure 9**, c, d). Hydrogel blocks with intact lumens were then subsequently used for downstream histological analyses. Representative immunofluorescence-stained sections are shown in **Figure 9**, d, where we stained selected DEGs, such as Angiopoietin-2, Claudin-5, and KLF4, found in the scRNAseq dataset. Approximately 25 sections were obtained from each lumen.

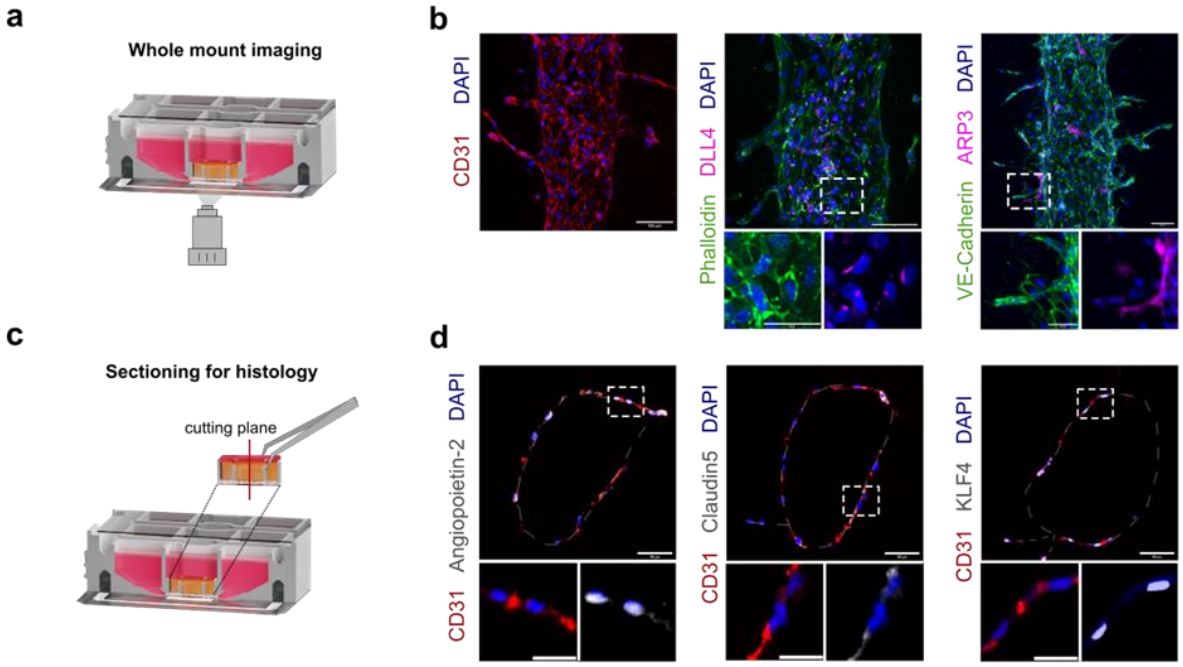

Figure 9: Whole mount and paraffin-section immunofluorescence stainings allow for detailed morphological analysis of endothelial tissue. a On-chip whole mount immunofluorescence staining can be directly performed, where concomitantly, the 100 µm distance of the lumen to the glass bottom allows high-resolution imaging. **b** Whole-mount staining of differentially expressed genes (DEGs) expressed in stem cell-derived endothelial cells (SC-ECs) cultivated under bidirectional flow on-chip. EC marker CD31 (scale bar 100 µm), flow-induced marker DLL4 (scale bar 50 µm), endothelial adherence junction marker CDH5, and branching marker ARP3 (scale bar 50 µm) with zoom-in images (scale bar 20 µm). **c** For performing multiple IF stainings from a single sample, the printed scaffold with the hydrogel-embedded vessels is removed using a tweezer. **d** Stainings of static cell marker ANPT2, barrier marker CLDN5, and flow-induced marker KLF4. The scale bar denotes 50 µm and 20 µm for the zoom-in images. See also Supplementary video 1.

Modeling the early-onset of atherosclerosis by oxidative stress under in vitro conditions on-chip

Elevated blood levels of oxLDL and FFA are crucial drivers of atherosclerosis plaque formation[190,191]. To model the early onset of atherosclerosis on-chip, we treated SC-EC vessels under flow conditions with either FFA or oxLDL (**Figure 10**, a) for 48 h. Both FFA and oxLDL accumulated within the SC-ECs, which was verified using BODIPY staining for all cytoplasmic lipids or using fluorescently labeled Dil-oxLDL (**Figure 10**, c and d). A FITC-dextran membrane permeability assay was performed to assess the barrier function of the vessels-on-chip after 24h and 48h oxLDL and FFA treatment. While vessels treated with FFA showed no difference in barrier function, vessels treated longer than 24h with oxLDL indicated a small increase in FITC-dextran leakage (Figure S5a, b). Further, IF stainings showed that the expression pattern of ZO1 changed from a plasma membrane to cytoplasmic location in

SC-EC after 2 days of oxLDL treatment but not after FFA treatment or control samples (Figure S5c). A cytoplasmatic location of ZO-1 has been reported upon hypoxia stress induction in ECs[192].

The stimulation responses of SC-ECs were quantified by measuring the proteomic changes using mass spectrometry (LC-MS/MS). Cells from three lumens were retrieved and pooled to obtain approximately 9000 cells. Protein counts and the dynamic range of proteomic data were comparable for all samples (Figure S6a-c). FFA formulation required BSA in the medium, and thus, the buffer conditions between the samples differed. Principal component analysis (PCA) and heatmaps showed differences in protein expression between the treatments and respective media controls, as well as coherence between repeats (**Figure 10**, b, Figure S6d, e). Differentially expressed proteins (DEPs) from both stimulation experiments were resolved using volcano plots (Figure S6f, g). Gene Ontology (GO) term analysis of the DEPs from both treatments showed enrichment of oxidative stress terms and included terms indicating the activation of protective oxidative reagents via the heme-oxygenase system[193] (**Figure 10**, e, f). GO terms for the FFA-treated samples included additional terms related to shunting overload of fatty acid activity or obesity-related inflammation, e.g. by the upregulation of toll-like receptor 4 (TLR4) signaling[194]. DEPs found within both treatments and unique to one treatment are shown in the Venn diagram in **Figure 10**, g. Both treatments led to the upregulation of heme oxygenase 1 (HMOX1), which is expressed as a protective response to ROS stress[195]. We live-stained the SC-ECs on-chip with a fluorescence indicator (CellROX) for ROS species to test whether oxidative stress was induced by FFA and oxLDL treatment. The normalized mean intensity signal of the CellROX fluorophore (**Figure 10**, h) increased in oxLDL-treated SC-ECs with a signal intensity comparable to that of the positive control treatment of the cells with tert-butyl hydroperoxide (TBHP). We did not detect an increase in the CellROX signal for FFA treatment compared with the respective medium control.

Next, we investigated whether adding the sortilin inhibitor TY52156 could lower oxidative stress in SC-EC. Proteomic analysis showed that a sortilin family member (SORCS2) was upregulated in SC-EC upon FFA (1.56-fold; p-adj=0.03) and oxLDL (1.40-fold; p-val=0.02) treatment. Sortilin was previously found to be positively correlated with atherosclerosis and cardiovascular disease[196]. TY52156 co-treatment did not lead to a visibly altered FFA or oxLDL accumulation (Figure S6h). Notably, in the oxLDL + TY52156 treated samples, the CellROX signal was significantly lower than that in the samples treated with oxLDL alone (**Figure 10**, h). In the FFA-treated SC-EC, TY52156 had no significant influence on CellROX signaling.

Considering the enrichment of proteins related to eNOS function (ENG, CYBG, and HMOX1) in the proteome analysis of both conditions, we quantitatively measured NO production by SC-ECs on the OoC after oxLDL and FFA treatments. Indeed, NO concentrations in the oxLDL-treated SC-EC vessels were significantly reduced compared to those in the respective medium controls (**Figure 10**, i). Here, the sortilin inhibitor TY52156, applied to oxLDL-treated SC-ECs, did not rescue the NO production. The NO assay on the FFA-treated samples showed no difference compared to the medium control, which aligns with the non-significant CellROX staining. Thus, when compared to oxLDL, SC-EC treatment with FFA leads to different molecular response mechanisms.

To further investigate the oxidative stress response of the SC-EC, we measured the secretome of the cells. For this purpose, we used the flow-through volume in the chip reservoirs for LC-MS/MS analysis (**Figure 11**, a). 1,939 secreted proteins with high confidence level, retrieved over a time interval of 24h from SC-EC treated with oxLDL, were identified by mass spectrometry. 152 proteins of the secretome were up- or downregulated by a 1.5 fold change in comparison to the control, from which 45 contained a signal peptide for active secretion into the blood[197]. A GO term analysis of DEPs of the secretome with active secretion signals showed enrichment of proteins for HDL and chylomicron remodeling (**Figure 11**, b). Among the upregulated proteins in the secretome were members of the apolipoprotein family (**Figure 11**, c). For example, the secreted APOC3 and APOA1 are known to change the NO synthesis of ECs and are linked to pathophysiological processes leading to cardiovascular disease (CVD).

Within the secretome of SC-EC treated with FFA 693 proteins were determined, where only 18 were differentially regulated in comparison to the control sample (**Figure 11**, b). SC-EC secretomes in response to FFA and oxLDL treatment have no overlap showing once more the differently induced stress. Notably, in agreement with the proteome measurements the FFA treatment led to an increased secretion of the SORCS2 (**Figure 11**, d).

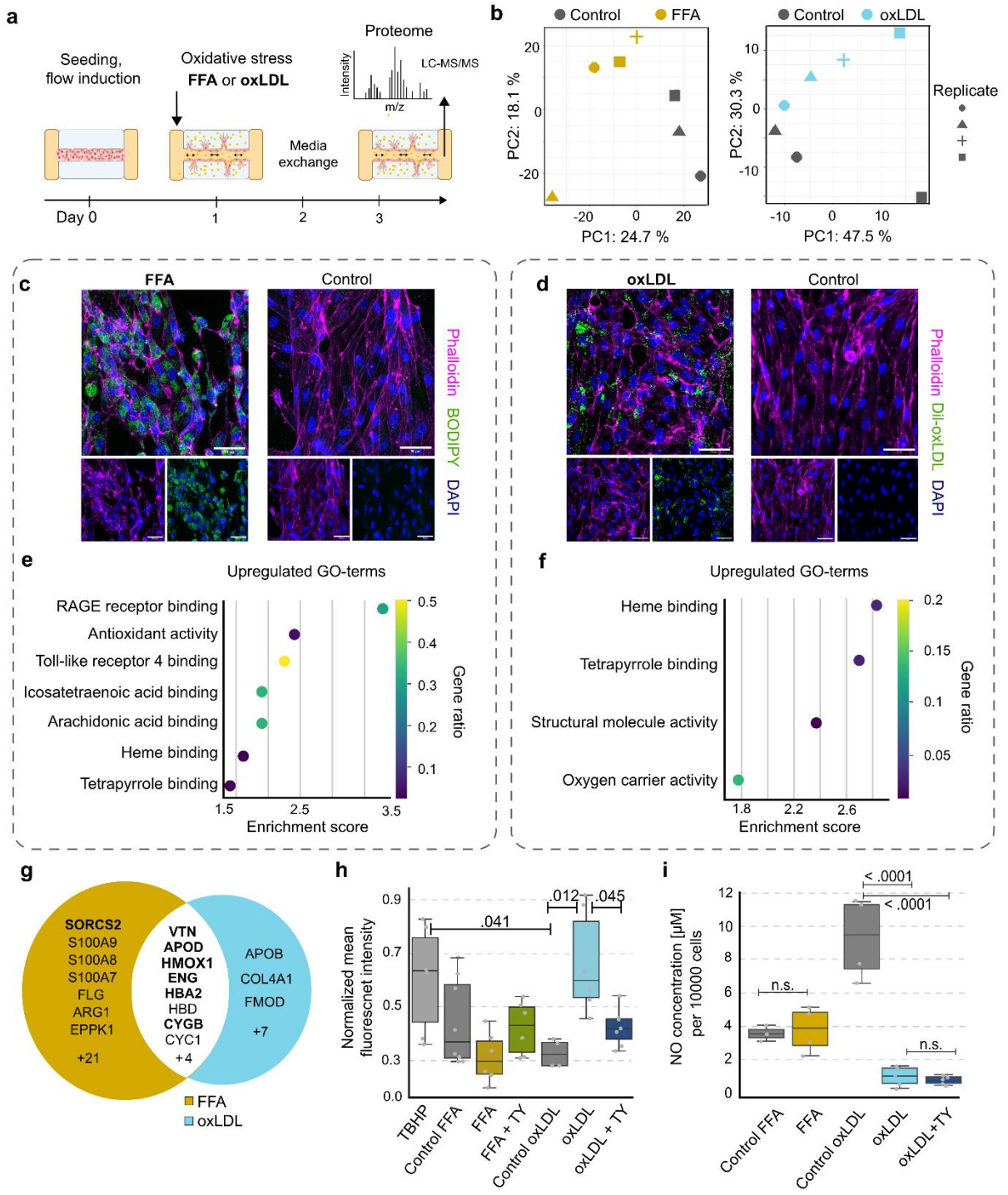

Figure 10: Oxidative stress induction of vessel formed on-chip. a Experimental outline. On day 1, stem cell-derived endothelial cells (SC-ECs) were treated with free fatty acids (FFA) or oxidized low-density lipoproteins (oxLDL). On day 3, proteome and secretome data were acquired using mass spectrometry. **b** Principal component analysis of the proteome data after FFA (n=4) or oxLDL (n=4) treatment and their respective medium controls (n=3). **c** Immunofluorescent images of fatty acids with BODIPY in FFA treated samples vs control. Scale bar, 50 µm. **d** Immunofluorescent images of fluorescence labeled Dil-ox-LDL treated samples vs control. Scale bar, 50 µm. **e** Top 8 upregulated Gene Ontology (GO) terms in the FFA condition compared to the untreated control. **f** Top 4 upregulated GO terms in the ox-LDL condition compared to the untreated control. **g** The Venn diagram highlights the selected

proteins upregulated in the FFA and oxLDL conditions and their overlap. **h** Analysis of the reactive oxygen species in the treated samples versus control. Samples were live-stained for Hoechst and CellROX reagent (Thermo) and imaged, and the CellROX signal intensity was normalized to the Hoechst intensity. ECs were treated with TBHP as a positive control. Data are presented with a confidence interval (CI) of 95% for the error bars, and n ≥ 12, except for TBHP with n = 3. Boxplot outliers were removed when indicated in the python package seaborn. **i** Cell count-normalized NO concentration (µM) in supernatants of treated samples vs their respective control on day 3. Error bars indicate a CI of 95%, and n = 3–5. *p* values of **h** and **i** were calculated with a parametric one-way ANOVA and Tukeys post-hoc test and are indicated in the figures.

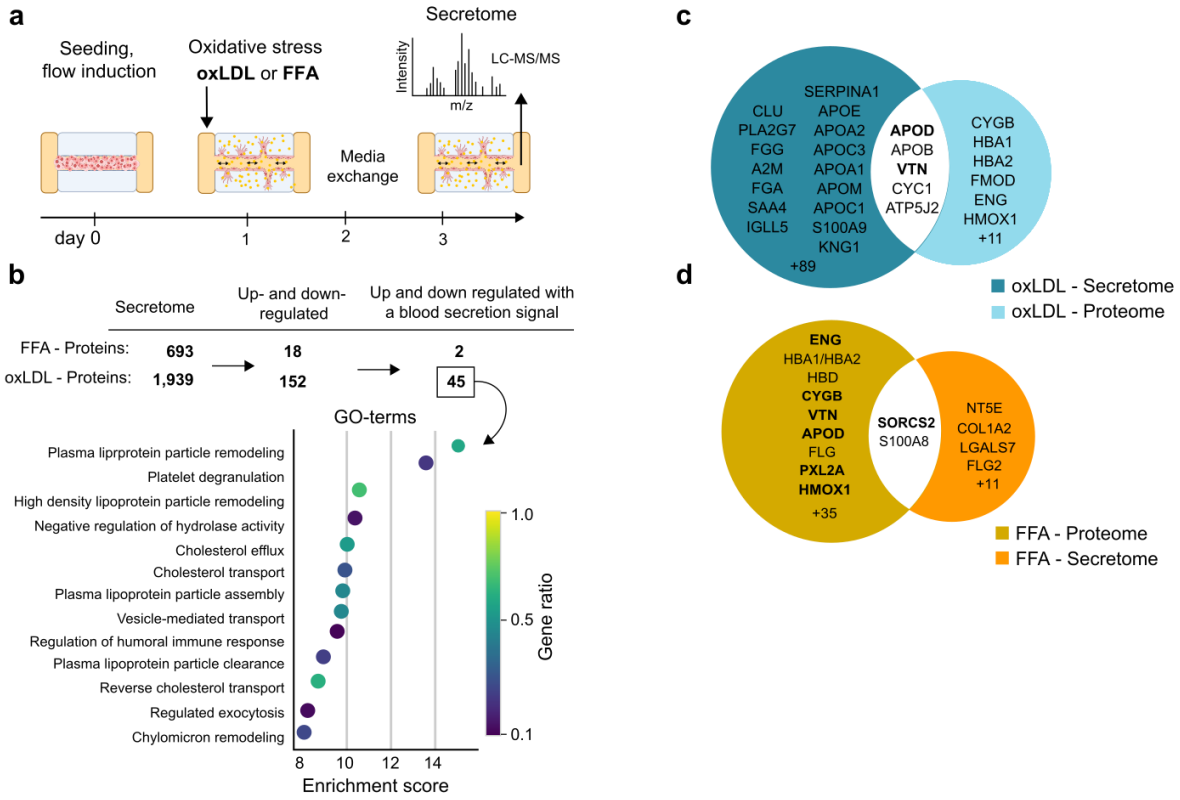

Figure 11: Secretome analysis of oxLDL and FFA treated SC-ECs on-chip. a Experimental outline: SC-ECs were treated with oxLDL and FFA on day 1. Supernatants were collected from the chip reservoirs on day 3 for a LC-MS/MS analysis. **b** oxLDL treatment resulted in up- and downregulation of secreted proteins with and without export signal compared to a control sample without cells. GO term analysis of the differentially secreted proteins with blood secretion signal revealed a response of the cholesterol metabolism to the oxLDL treatment. **c** and **d** Venn diagram highlights proteins upregulated in the secretome and matched proteome of SC-EC treated by oxLDL and FFA.

3.5 Discussion

In this study, we manufactured an open microfluidic platform for engineering organotypic endothelial vessel structures. The open microfluidic design enables the platform to interface with all state-of-the-art analytical technologies, including single-cell RNA sequencing, proteomics by LC-MS, and high-resolution imaging. Concomitantly, engineered endothelial tissues can be functionally assessed under mechanical- and fluid-controlled culture conditions. The manufacturing of the chip platform was robust, as validated by more than 500 lumens in the presented dataset. Although we only functionally analyzed lumens using COL1 hydrogels, microchannel formation was also positively confirmed for Matrigel or fibrin hydrogels (data not shown), in support of general applicability of our OoC platform for all commonly used tissue microenvironments.

After on-chip adjustment, our gravity-driven flow culture resulted in a wall shear stress of up to 3 dyn cm^{-2}. This value correlates with physiological flow in microcapillaries but, unsurprisingly, is lower compared to flow in larger vessels [166]. In contrast to physiological flow, the shear stress on our chip platform was generated with a rock shaker and is therefore bidirectional. Nevertheless, functional validation showed that our SC-EC vessels recapitulate vascular barrier integrity and physiological processes such as sprouting.

We previously resolved the transcriptomic trajectory of SC-ECs during microvessel formation in a hydrogel microenvironment[31]. In this study, we used the same SC-EC for the luminal vessel structure. Single-cell transcriptomic data, particularly velocity analysis, revealed dynamic cell state changes of SC-EC from static to flow culture conditions. Live/dead staining of SC-ECs on the chip under flow and static conditions revealed no differences (Figure S3a), however, SC-EC retrieval from the on-chip static culture condition resulted in a higher dead cell count, suggesting generally lower cell stress of SC-ECs under flow culture conditions. This is probably related to the expression of stress-related genes like *NQO1* or *ROMO1*[173], especially in the “static” cluster. Notably, the resolved SC-EC cell states were in accordance with the morphological and functional phenotypes of the chip, including sprouting, barrier-forming, and flow-exposed ECs. SC-EC under shear flow upregulated the shear stress-responsive genes essential for vascular function, including *KLF2/KLF4* under flow conditions[198]. Most strikingly, the higher transcriptomic correlation of the SC-EC cultured under flow culture conditions with adult arterial ECs demonstrated the flow maturing effect on the SC-ECs. Staining for endothelial markers (CD31), sprouting markers (DLL4 and ARP3[189]), static marker (ANGPT2[135]), barrier marker (CLDN5[183]), and flow induction marker (KLF4[135]) substantiated the single-cell transcriptomic data at the protein level, and hence to translate into biological function.

Another central finding derived from our vessel-on-chip model is the identified transcriptomic upregulation of NO synthesis, respective signaling genes, such as eNOS (*NOS3*), and *CAMK2D* under flow culture conditions. In stark contrast, SC-EC cultured under static conditions revealed increased expression of genes known to downregulate eNOS function, e.g. *NOSTRIN, NOSIP*, and *CAV1*[187]. An on-chip quantitative assay (**Figure 8**, j) indeed verified the opposing effects of shear versus static culture conditions on NO synthesis, and by extension, on the *in vivo* endothelial cell behavior[199].

Beyond the characterization of the organotypic EC culture on-chip, we validated the general functional relevance of our new chip platform by modeling the pathogenesis of atherosclerosis. Given oxLDL particles shown to be involved in the induction of the early characteristic events of atherosclerosis[200] and excess FFA present in patients with atherosclerosis, we treated our SC-ECs with FFA or oxLDL to potentially address FFA pathomechanisms[191]. One hallmark of oxLDL is the uncoupling of NO production in the ECs via eNOS inactivation[190]. Functional changes, high ROS production, and reduced NO synthesis were indeed observed in the SC-EC vessels-on-chip. The proteome of SC-ECs under oxLDL treatment reflected the ROS-induction, ER stress, and antioxidant stress responses. Particularly, the DEPs ENG[201], CYBG[202], and HMOX1[195] are known regulators of endothelial NO synthesis and mechanistically link induced ROS with the functional phenotype of reduced NO synthesis. Notably, the increased ROS occurrence upon oxLDL treatment was ameliorated in SC-ECs by adding the sortilin inhibitor TY52156. However, TY52156 did not rescue NO production, indicating that either the ROS-reducing effect of TY52156 could not compensate for NO-synthesis or both responses not being directly interlinked.

Additionally, FFA treatment induced a proteomic stress signature in SC-ECs with overlapping DEPs in response to oxLDL stress. In contrast to the oxLDL treatment and to *in vivo* experimental data, NO production and ROS concentrations were not altered compared to the controls. One explanation for this finding can be the relatively short treatment of 48 h. FFAs are stored in the SC-ECs in small lipid droplets as shown by the BODIPY staining (**Figure 10**, c). Comparably to *in vivo* conditions, endothelium initially buffers excessive FFA loads by storing them in lipid vesicles and degrading those lipids by lipolysis[203]. Therefore, long-term *in vitro* studies are required to answer this question. Notably, an immediate ROS-protective response was initiated through the upregulation of the heme-oxygenase system for both treatments. Vitronectin was an additional upregulated DEP after oxLDL and FFA treatments. Evidently, vitronectin is central to atherosclerosis progression[204]. Elevated vitronectin levels have been suggested as potent biomarker of coronary artery disease[205]. Vitronectin detection within the secretome after oxLDL treatment underpins the relevance and applicability of the chip for new biomarker discovery.

One limitation of our study is the bidirectional laminar flow profile at a lower wall shear stress regime of up to 3 dyn/cm^2 on the vessel-on-chip platform. Under physiological conditions, blood flow occurs unidirectional, where the wall shear stresses vary largely depending on organ function, vessel size, or viscoelastic parameters of the blood. For example, shear rates in capillaries or lymphatic vessel are in the order of 2 dyn/cm^2, whereas in larger arteries the shear stress ranges from 10 as high as 70 dyn/cm^2 [5]. Engineering *in vitro* tissue models on chip is a balance between simplicity in terms of cost-effective handling and screening versus the complexity of the *in vitro* tissue. The presented vessel-on-chip platform provided a dynamic microenvironment, in which the SC-ECs established a complete endothelial barrier function, matured to arterial-like ECs, showed NO-secretion comparable to *in vivo* vessels, and enabled higher throughput screening. On the other hand, perturbed flow, which is defined as turbulent flow at low shear stress, will promote atherosclerosis under *in vivo* conditions. To which extent the bidirectional flow on-chip, but also long-term culture times contribute to the atherosclerosis model remains to be resolved. From a future perspective, unidirectional flow and higher wall shear stress can be established on our chip by adopting gravity flow concepts developed for closed[206] microfluidic channel networks, increasing the hydrodynamic flow pressure by increasing the volume of the fluid reservoirs, or the tilt angle of the chip.

In summary, we developed a robust and easy to use open OoC platform for screening parallel endothelial functions using standard laboratory equipment. The reported integration of stem cell-derived endothelial cells offers the opportunity to study *in vitro* endothelial development, tissue-specific toning, and immune interactions at high resolution and at single-cell levels. Beyond the increasing number of vessel-on-chip platforms, our open and general design of the chip allows it to ‘host’ seamlessly any epithelial cell type. Combined with the open hydrogel design, our setup facilitates the engineering of more complex, and particularly vascularized tissues in a ‘plug and play’ manner, to our knowledge for the first time. More broadly, our platform opens new avenues for universal use to engineer larger and more complex tissue/organs considering the integration of gene editing tools or patient-specific stem cell lines. Our approach thus serves the urgent need to replace animal models/reduce animal use by developing a novel, functionally reliable, and easily customizable vascularized human OoC platform.

3.6 Extended Data

Supplement Figures can be found in the publication this chapter is cited from: Marder, M.[$], **Remmert, C.[$]**, Perschel, J. A., Otgonbayar, M., von Toerne, C., Hauck, S., Bushe, J., Feuchtinger, A., Sheikh, B., Moussus, M. and Meier, M. (2024). Stem Cell-Derived Vessels-on-Chip for Cardiovascular Disease Modeling. Cell Reports. doi: 10.1016/j.celrep.2024.114008.

4 Vascularization of stem cell-derived β-cells for diabetes research

4.1 Declaration of contribution

Experiments, analysis, and results in the following chapter were conducted and evaluated by me, if not otherwise stated. This included: all experiments with stem cell-derived islet-like clusters (SC-ILC), functional assays, staining, the single-cell RNA sequencing (scRNAseq) experiment, and data analysis. Sandra Wiedenmann and I did the CellChat analysis. Nicole Rogers differentiated hiPSCs to SC-ILC until early stage 6 (S6). Maren Marder acquired the scRNAseq control data of stem cell-derived endothelial cell (SC-EC). Figure design and writing was done by me. The study was designed by Matthias Meier, and me. Heiko Lickert and Henrik Semb advised the study with their knowledge about islet biology.

4.2 Introduction

The endocrine pancreas consists of the islets of Langerhans, which are responsible for the secretion of hormones into the bloodstream. The islets contain various endocrine cell types, the majority of which are insulin-producing β-cells. The β-cells' counterparts include glucagon-producing α-cells and somatostatin-secreting δ-cells[207]. The coordinated interaction of all endocrine cells is important for precisely regulating blood glucose levels. The microenvironment of islet cells consists not only of endocrine cells, but also of extracellular matrix (ECM) and other cell types such as stromal cells, macrophages, nerve cells and blood vessels, all of which influence endocrine functionality[208]. Although the islets comprise only 1-2 % of the pancreatic volume, they are supplied with about 15 % of the blood[68]. The islet microvasculature is essential for the function of endocrine cells, especially for β-cells. It plays a role in the onset and progression of diabetes, resulting in morphological changes in the microvasculature[209]. In the islet niche, endothelial cells (ECs) and β-cells signal bidirectionally by secreting molecules, ECM, and through cell-cell interaction[210]. Islet-ECs secrete ECM molecules and synthesize the basement membrane, which is important for the function and survival of islet cells. At the same time, β-cells secrete angiogenic factors such as VEGF, which influence the vessels' size, density, and migration[70,210]. It has been shown that islet-ECs are important for the development and proliferation of β-cells[211], improve glucose-stimulated insulin secretion, and increase insulin content[210,212].

Diabetes mellitus is a metabolic disorder that leads to impaired insulin secretion and hyperglycemia. Diabetes can be divided into two major groups: Type I diabetes (T1DM), which is caused by the destruction of β-cells due to an autoimmune reaction, and Type II diabetes (T2DM), which is characterized by stress-induced exhaustion and dysfunction of β-cells. Various metabolic, environmental, genetic, and immunological factors influence both types[213]. Patients require lifelong insulin therapy to treat hyperglycemic events and insulin injections remain the standard care particularly for T1DM and late-stage T2DM. However, the disease is not cured and patients who fail in normalizing blood glucose levels suffer from secondary complications, shortened life expectancy or life-threatening hypoglycemic events[65]. Thus, different approaches have been studied to protect and regenerate the β-cell mass including immunotherapy[78], bariatric surgery[214], pharmacological interventions[215] or cell replacement therapy[65]. Cell replacement therapies, in which pancreatic islets are transplanted, can re-establish glycemic control, decrease the risk of hypoglycemic events, and prevent life-threatening complications associated with diabetes[75]. Currently, approved replacement therapies for T1DM include transplantation of cadaveric islets or whole pancreas and allow independence from exogenous insulin for more than 10 years [80,81]. However, the limitation of islet transplantation is the shortage in donor material and the reliance on immunosuppressive drugs which inhibit the widespread adoption of pancreatic or islet transplantation therapies. Here, differentiation of human pluripotent stem cells, such as human induced pluripotent stem cells (hiPSCs), hold promise as they can serve as an unlimited source of stem cell-derived islet-like cluster (SC-ILC)[96,216]. SC-ILC respond to glucose concentrations in secreting insulin and show transcriptional similarity to native islets. However, compared to the transcriptome and function of primary human islets, they are of an immature character[217]. Maturation requires an *in vivo* environment, as shown in rodent transplantation studies[88]. More research is needed to improve differentiation and *in vitro* cultivation protocols to further mature SC-ILC. In addition, SC-ILC transplantation still requires immunosuppression and continued research is needed to develop immune-protective strategies like encapsulation[79], co-transplantation with immune-regulatory cells[94] or improving the transplantation site[218]. Islet vascularization is particularly important when considering encapsulation strategies and alternative, rather avascular, transplantation sites. SC-ILC lack any vascularization, and cadaveric islets lose most of their vasculature during isolation[98]. The low vascular density leads to poor graft survival, resulting in delayed and suboptimal glycemic control. Prevascularization of the graft has been shown to improve graft survival, revascularization, and function and can positively affect β-cell maturation[99]. However, generation of a fully hiPSC-derived vascularized transplant has not been shown so far and there is a lack in *in vitro* stem cell models to study islet-EC interactions.

Here we developed an *in vitro* encapsulation model for the vascularization of SC-ILC. We mimicked the islet microenvironment using stem cell-derived ECs (SC-ECs), stromal cells, and a hydrogel to investigate the interaction profiles of SC-ECs and SC-ILC. The SC-ECs and SC-ILC used can be differentiated from the same hiPSC line. In the future, this will make it possible to differentiate both cell types from a clinically established cell line or to produce autologous transplants. In addition, a stem cell-derived model has the advantage that early stages of embryonic development or patient-specific backgrounds can be investigated. Further, human adipose-derived stromal cells (hASC) were used offering the possibility of autologous isolation and have been reported to positively influence graft survival[94,219] and islet function[220,221]. Using this model, we show that vascularization enhances insulin secretion from stem cell-derived β-cells (SC-β). Single-cell RNA sequencing (scRNAseq) and cell-cell communication analysis revealed a specific and direct interaction between SC-ECs and endocrine cells. We show that this interaction benefits all cell types involved and that both SC-β-cells and SC-ECs matured and adapted to the islet microenvironment. The identified interaction pathways can be used as targets for SC-ILC maturation in the future. Although diabetes primarily affects β-cells, there is evidence that α-cell dysfunction contributes to the disease[222]. Here we show that islet vascularization positively influenced α-cell function. Vascularized SC-α-cells secreted glucagon at physiological glucose levels and showed expression of maturation markers similar to transplanted islets. Altogether, our vascularization model can help to better understand the interaction between ECs and endocrine cells, especially β- and α-cells. In the future, our model can be used to build patient-specific *in vitro* models that could be used for diabetes research.

4.3 Material and Methods

Resource table

Reagents used in this chapter can be found in the text or in **Table 3** or **Table 5**.

Table 3: Chemicals and recombinant proteins.

REAGENT or RESOURCE	SOURCE	IDENTIFIER
Chemicals, recombinant proteins, reagents		
Accutase	Sigma Aldrich	A6964
ADSC growth medium bulletKit	Lonza	PT-4505
BSA 10%	Thermo Fisher Scientific	37525
BSA fatty acid free	Proliant Biological	SKU68700
collagen type I hydrogel	Corning	354236
Collagenase P	Roche	11213857001
DAPI	Sigma Aldrich	D9542
Donkey serum	abcam	ab7475
EDTA	AppliChem	A4892
EGM-2	Sigma Aldrich	C-22011
FBS	Sigma	F7524
FGF2	Miltenyi Biotec	130-093-838
Fibronectin	Thermo Fisher Scientific	33010018
Geltrex	Thermo Fisher Scientific	A1413302
Glucose	Thermo Fisher Scientific	A2494001
GlutaMAX	Thermo Fisher Scientific	35050038
Heparin	Sigma	H3149
Matrigel	Corning	354277
MCDB131 medium	Thermo Fisher Scientific	10372019
MEM non-essential amino acids	Thermo Fisher Scientific	15333581
ROTI® Histofix 4% PFA	Carl Roth	P087.6
Somatostatin	Sigma	S1763
StemMACS™ iPS-Brew	Miltenyi Biotec	130104368
StemPro-34	Thermo Fisher Scientific	10639011
tissue freezing medium	Leica	14020108926
Trace elements A	Thermo Fisher Scientific	15333641
Trace elements B	Thermo Fisher Scientific	15343641
Trypan Blue	Sigma	T8154
VEGFA	Peprotech	100-20-250
Y-27632	Biozol	APE-A3008-10
ZnSO4	Sigma	Z0251

HiPSC culture

HiPSCs were cultured on tissue culture plates coated with diluted Geltrex (Life Technologies, #A1413302) in StemMACS™ iPS-Brew medium (Miltenyi Biotec, #130104368). Cells were

cultured under standard culture conditions (37°C, 5% CO_2) and medium was changed daily. HiPSCs were splitted with 0.5mM EDTA (AppliChem, Cat#A4892) at 70% confluency. Cells were checked for mycoplasma with the MycoAlert PLUS Mycoplasma Detection Kit (Lonza, Cat#LT07-703) according to the manufacturer´s protocol. For this study, an unpublished reporter line was used that was adapted from the published mCherry C-peptide clone HMGUi001-A-8[223]. For this study, only the mCherry C-peptide expression was of interest.

Differentiation of stem cell-derived β-cells from hiPSCs and cell culture procedures

HiPSCs were differentiated to SC-ILC according to a published protocol[85]. In brief, hiPSCs were single cell dispersed and seeded at 0.6 x 10^6 cells ml^{-1} in 30 ml spinner flasks or 6 well ultra-low attachment plates (ULA, Corning, Cat#3471) with 10µM Rock inhibitor Y-27632 (Biozol, #APE-A3008-10). Before differentiation was started, the cells were cultured as 3D aggregates for at least 2 days. In a 6-stage protocol, cells were differentiated to SC-β-cells. Beginning of stage 6 (S6), cells were reaggregated to reduce the number of off-target products. Therefore, S6 cells were washed with PBS, dispersed with Accutase (Sigma Aldrich, Cat#A6964) for approximately 30 min and filtered through a 40 µm cell strainer (pluriSelect, Cat#43-10040-40). Single cells were seeded at 1 x 10^6 cells ml^{-1} in ULA plates (S6 medium with 10µM Rock inhibitor Y-27632) and placed on an orbital shaker at 100 rpm at 37°C and 5% CO_2. Medium was changed every day. After 14 days in S6, medium was changed every other day. Composition of the S6 medium (S6M) can be found in **Table 4**.

Table 4: S6 medium.

REAGENTS	FINAL CONCENTRATION	VOLUME for 100 ml [ml]
MCDB131 medium		100
Glucose	0.46 g l^{-1}	0.23
BSA	0.02 g ml^{-1}	2.1 g
GlutaMAX 100x	1x	1.04
P/S 100x	1x	1.04
MEM non-essential amino acids 100x	1x	1.04
Trace elements A 1000x	1x	0.105
Trace elements B 1000x	1x	0.105
ZnSO4 10mM	10 µM	0.105
Heparin 50 mg/ml	10 µg ml^{-1}	0.02

Human adipose tissue-derived stromal cells (hASCs) were purchased from ZenBio (NC, USA, donor ASC062118A) and maintained in routine 2D cell culture using Adipose Derived Stem Cell Growth Medium (Lonza, Cat#PT-4505). hASCs were used at passages 5-9 for experiments.

To differentiate endothelial cells (SC-EC), hiPSCs (AICS-0036-006, Corielle Institute) were differentiated in a 3D shaking culture approach as described before[18,31,224]. The protocol was slightly adjusted by extending the differentiation protocol until day 10. From day 7 to day 10, cells were matured in StemPro-34 medium (Life Technologies, Cat#10639011, see **Table 1**) with 15% FBS (Sigma, Cat#F7524), 100 ng/ml VEGFA (PeproTech, Cat#10-20-100) and 100 ng/ml FGF2 (Miltenyi Biotech, Cat#130-093-838). Successful differentiation was determined by flow cytometry analysis and staining for the EC marker CD31-FITC (BD, Cat#555445) and the smooth muscle cell marker CD140b-PE (BD, Cat#558821). For purification, SC-ECs were cultured on fibronectin-coated plates (Sigma, Cat#33010018, 5 µg/ml final concentration) leading to a SC-EC population of >90% after 1 or 2 passages. Standard SC-EC culture was performed on fibronectin-coated plates in StemPro-34 medium supplemented with 15% FBS, 100 ng/ml VEGFA and 100 ng/ml FGF2. Medium change was done every other day. SC-ECs could be passaged and were used until passage 6. For passaging, cells were washed with PBS-/- and detached with Accutase. The reaction was stopped with StemPro-34 medium followed by a centrifugation at 200xg and 5 min. SC-ECs were resuspended in supplemented StemPro-34 medium and seeded in a 1:2 ratio in T75 flasks. For cryopreservation, detached SC-ECs were resuspended in FBS with 10% DMSO.

Generation of a vascularization model for SC-ILC

To generate the vascularized co-culture (vCo-culture, SC-ILC with hASC and SC-EC in a hydrogel) and Co-culture (SC-ILC with hASC in a hydrogel), a collagen type I hydrogel (Corning # 354236) was neutralized for pH=7.0 with the appropriate proportions of 10xPBS,1 mM NaOH and H_20 to obtain 2.5 mg ml^{-1}, mixed thoroughly and placed for 1 hour on ice. After the incubation, the collagen I hydrogel was mixed with an equal volume of hESC qualified Matrigel (Corning, Cat#354277, stock concentration 8 mg ml^{-1}). For cell seeding, hASCs and SC-ECs were dispersed to single cells. For the vCo-culture, 12 x 10^3 hASCs and 3 x 10^3 SC-ECs were seeded in 5 µl hydrogel in an µ-Slide Angiogenesis (ibidi, #81501, uncoated). For generating the co-culture, 12 x 10^3 hASCs were seeded in hydrogel. For both conditions, SC-ILC were resuspended in hydrogel and pipetted into the prepared hydrogel-cell-suspension, aiming for 2-6 aggregates per well. Hydrogel cultures were incubated for 30 min at 37°C to allow polymerization before 50 µl medium were added. Samples were cultured at 37°C, 5% CO_2 for seven days. Medium was changed every day. For medium condition testing, cells were cultured either in S6 medium (S6M) or in a 1:1 mix of S6M and the endothelial growth media EGM2 (Sigma, #C-22011), or StemPro34 supplemented with 15% FBS, 100 ng/ml VEGFA and FGF2, respectively. For the normalization of functional assays, SC-ILC were counted in each well on day 0. Besides the two hydrogel cultures, SC-ILC were cultured in

suspension for the time of the experiments to have a comparable control without hydrogel and hASCs.

Hormone secretion assay

A static glucose-stimulated insulin secretion (GSIS) assay was performed to assess the ability of SC-ILC to secrete insulin. Therefore, SC-ILC and hydrogel cultures were transferred to a 96-well V-bottom plate and starved for 2 hours in Krebs Ringer Buffer (KRB, 129 mM NaCl, 4.8 mM KCl, 1.2 mM KH_2PO_4, 1.2 mM $MgSO_4$, 2 mM $CaCl_2$, 24 mM $NaHCO_3$) with a concentration of 2.8 mM Glucose. After 1 hour of starvation, the buffer was renewed. Samples were washed and incubated for 1 hour each in KRB with 2.8 mM Glucose or 20 mM Glucose. Supernatants were collected after each step, followed by a washing step. In total, two cycles of low and high glucose concentrations were performed. Last, samples were incubated in KRB with 30 mM KCl and 2.8 mM Glucose for 1 hour; supernatants were collected afterward. All supernatants were stored at -20°C until the insulin concentration was quantified with an ultra-sensitive human insulin ELISA kit (Mercodia, Cat#10113201) according to the manufacturer protocol.

For the glucagon secretion assay, cells were prepared and starved as described before. Next, cells were incubated in the following buffers for 1 hour each: 7 mM glucose, 20 mM glucose, 100 ng/ml somatostatin in 2.8 mM glucose buffer, 30 mM KCl in 2.8 mM glucose buffer. Each step was followed by a washing step in the respective buffer before the next incubation was started. Glucagon concentration in the collected supernatants was quantified with a glucagon ELISA kit (Mercodia, Cat#10-1271-01) according to the manufacturer's protocol.

Microscopy and immunofluorescence

Live images were taken with a confocal microscope (LSM-880, Zeiss). For immunostainings, cells and hydrogels were fixed in 4% paraformaldehyde (ROTI Histofix) for 30 min at RT. Samples were washed in PBS-/- and dehydrated at RT using a sucrose gradient of 10% (w/v) and 30% (w/v) for 2 hours each, followed by overnight incubation in a 1:1 mixture of 30% sucrose and tissue freezing medium (Leica, # 14020108926) at 4°C. The next day, samples were embedded in cryo tissue molds in tissue freezing medium on dry ice. Samples were sectioned into 10-20 µm slices at the cryostat for immunofluorescence staining.

For staining, sections were dried for 30 min at RT, rehydrated in PBS-/- for 20 min, and permeabilized for 20 min at RT (0.1 M glycine, 0.1% TritonX-100 in PBS-/-). Next, samples were blocked in blocking buffer (10% FBS, 0.1% BSA, 3% donkey serum in PBS-Tween (0.2 %), 0.1 M glycine) for 2 hours at RT. Sections were incubated in staining buffer (0,1% BSA, PBS-Tween (0.2 %)) with primary antibody overnight at 4°C. The next day, samples were washed 3 times for 10 min in PBS-/- before incubating with secondary antibody for 3 hours at

RT. All secondary antibodies were diluted 1:500 in staining buffer. Sections were washed 3 times in PBS-/-, mounted in Vectashield mounting medium PLUS (Vector Laboratories, #VEC-H-1900-10) and z-stacked images were taken with a confocal microscope (LSM-880, Zeiss). All antibodies used can be found in **Table 5**.

For image analysis, the area of expression was analyzed in z-projected images with FIJI. Measured values were normalized to the expression of DAPI. For statistical analysis, samples were tested for normal distribution with a Shapiro test. Equal variances were tested with a Bartlett test. If normally distributed, a one-way-ANOVA was conducted. A Tukey post-hoc test was performed afterward.

Table 5: Immunofluorescence antibodies used for the characterization of the vCo-culture.

REAGENT or RESOURCE	SOURCE	CATALOG NUMBER
Primary Antibodies		
CD31, rabbit (1:100)	Invitrogen	PA516301
Insulin, guinea pig (1:300)	BioRad	53300104G
Glucagon, mouse (1:2000)	Sigma	G2654
Ki67, rabbit (1:200)	abcam	ab211968
NKX6.1, rabbit (1:100)	Cell Signaling	54551S
SCL18A1, rabbit (1:500)	ATLAS	HPA063797
CD44, mouse (1:100)	Merck	MAB4065
Cleaved Caspase3, rabbit (1:300)	Cell Signaling	9661S
Somatostatin, mouse (1:500)		
Collagen3A1, rabbit (1:50)	Novus	NB600-594SS
Integrin β1, mouse	R&D	MAB17781
Integrin α1, rabbit	R&D	MAB56761
E-Cadherin, rabbit	Cell Signaling	3195S
Collagen IV, rabbit	abcam	ab6586
MCAM, mouse	Invitrogen	MA1-25100
NCAM1, rabbit	Cell Signaling	99746S
Midkine (MDK), rabbit	abcam	AB52637-1001
MIF, rabbit	abcam	AB187064-1001
VEGF, rabbit	biotechne	AF-293-SP
GPR56, rabbit	Life Technologies	720373
Secondary Antibodies		
Cy3, anti- guinea pig	Biozol Diagnostica	706-165-148
AlexaFluor-488, anti-guinea pig	Jackson Immuno Research	JIM-706-545-148
AlexaFluor-647, anti-guinea pig	Jackson Immuno Research	706-605-148
AlexaFluor-555, donkey anti-rabbit	Thermo Fisher Scientific	A31572
AlexaFluor-488, donkey anti-mouse	Thermo Fisher Scientific	A32766TR
AlexaFluor-647, goat anti-mouse	Thermo Fisher Scientific	A31571
AlexaFluor-488, donkey anti-rabbit	Jackson Immuno Research	JIM-711-545-152

Whole mount immunofluorescence staining

For whole mount staining in the hydrogel, cells were fixed with 4% PFA (ROTI Histofix) for 30 min at RT and washed with PBS afterward. Samples were permeabilized with PBS + 0.1% Triton X-100 for 30 min at RT, washed with PBS and blocked for 2 h with blocking buffer "light" (0,1% BSA, PBS-Tween (0.2 %), 0.1 M glycine). Hydrogels were stained with primary antibodies (**Table 5**) in staining buffer for 2 days at 4°C. Primary antibodies were washed out thoroughly with PBS for 30 min before secondary antibodies were added in staining buffer. Secondary antibodies were incubated overnight at 4°C. Next, samples were washed with PBS for 30 min and mounted in Vectashield for imaging.

Sample preparation for single-cell RNA sequencing

For single-cell RNA sequencing, samples were washed with PBS, treated with a 1:1 mix of Collagenase P (18 U final concentration, Roche 11213857001) and Accutase and incubated for 30 min at 37°C. Successfully dissolved hydrogels and a single cell suspension was confirmed under the microscope before harvesting the cells in PBS + 10% FBS. The cells were centrifuged at 300xg for 3 min, washed with PBS + 2% BSA (Thermo Scientific, Cat#37525) and filtered with a 20 µm cell Pluristrainer (pluriSelect, Cat#43-50020-023). Cells were counted with TrypanBlue (Sigma, Cat#T8154) and a cell viability of over 90% was confirmed. RNA libraries were generated using Chromium Single Cell 3' library and gel bead kit v3.1 (10x Genomics, Cat#1000269 and #1000127). The amplified cDNA library was sequenced on a NovaSeq S2 flow cell from Illumina.

Pre-processing of scRNAseq data

Raw sequencing data files were demultiplexed, aligned (reference genome hg38_ensrel96), filtered, barcodes and UMIs counted, and subjected to a quality filter with CellRanger (10xGenomics). The pre-processing and downstream analysis were performed with the package Scanpy[149] in python with default parameters, if not stated differently. CellRanger-processed data were first concatenated. Next, dead or stressed cells, identified by a percentage of mitochondrial genes higher than 15%, were filtered out. Cells with more than 80000 total counts or cells with less than 200 expressed genes were excluded. Also, genes expressed in only 1 cell were rejected. Afterwards, gene counts were normalized to 10^4 per cell and log transformed. Additionally, total gene counts, cell cycle genes and mitochondrial genes were regressed out. Doublets were detected with the doubletDetection[225] package and regressed out.

Clustering and cell type annotation

The single-cell neighborhoods were calculated with 10 nearest neighbors, principal components were calculated, and cells clustered with the Leiden algorithm. For visualization,

UMAP was used to reduce dimensionality of the data. Cell types were annotated based on known markers from literature. Cell type proportions and gene expression analysis were performed based on the defined categorical clusters. Endocrine subcluster was defined by the expression of *CHGA* and the identified endocrine Leiden clusters. For endocrine subclustering, Leiden cluster identified as endocrine cells were subclustered into a new AnnData, raw genes were loaded and filtered. Doublets, total gene counts and mitochondrial genes were regressed out.

For the analysis of vCo-, Co-culture, and SC-ILC, subclustering was done on the concatenated AnnData according to *INS* and *GCG* positive Leiden clusters.

To compare SC-ECs from the vCo-culture to a control, CellRanger-files were loaded and concatenated. AnnData files were filtered and processed as described before and an EC subcluster was extracted after Leiden clustering. Subclustering was performed as described before. For this analysis, a batch correction[226] was necessary, which was performed on both the complete and subclustered AnnData.

Velocity analysis of the scRNAseq data

For further analysis of the scRNAseq data, a velocity analysis was performed. We analyzed the RNA velocity by recovering directed dynamic gene information through splicing kinetics in basic mode following the scVelo[184] standard pipeline. Variables and observations, like cluster annotation and UMAP coordinates were accessed from the Scanpy analysis as described above. The splicing matrix was generated by default settings of the velocyto[227] pipeline. After concatenating splice matrix and scanpy information, splice variants and cells were filtered, normalized, and logarithmized with the function scv.pp.filter_and_normalize. The moments, based on the connectivity, were calculated in the next step. Then, velocities and the base root cell were assessed by the sc.velo[184] algorithm and represented in a UMAP embedding stream projection.

Pathway analysis

For KEGG pathway analysis[228], the SC-α-cells were subclustered according to Glucagon expression and DEGs of vCo-culture, Co-culture, and SC-ILC were calculated. The top 300 DEGs were exported. The contribution of the exported DEGs to respective pathways was calculated with the gseapy package[229] (p-value cut off = 0.05, log2 foldchange minimum = 0.25). Interesting pathways were extracted from the analysis and pathways with a -log10(adjusted p-value) > 2 were stated as significantly upregulated. For the GO-term analysis, the SC-EC subcluster was analyzed with the gseapy package[229] and the significance was calculated by comparing DEGs with the "Biological Processes 2023" database[230].

CellChat analysis

For cell-cell communication analysis, the R package CellChat version2[231] and tutorial[232] was used. Therefore, the h5ad files of the vCo-culture and Co-culture were transformed to R compatible Seurat[233,234] files and analyzed independently. In the Seurat objects Leiden clusters of the same cell types were combined. The human database CellChatDB was imported for the analysis. The communication pathways "Secreted signaling", "ECM receptor" and "Cell-cell contact" were selected from the CellChatDB. Of all the interaction pathways revealed by the CellChat analysis, only those involving interactions between SC-ECs and endocrine cells were selected for deeper analysis.

Statistical methods

Statistical methods used are indicated in each figure legend. Data was generally tested for normal distribution and equal variances with a Shapiro and Bartlett test, respectively. Next, we performed a One-way ANOVA and Tukey's post hoc test. For insulin and glucagon secretion assays, a stimulation index related to the first low glucose peak of each sample was calculated. This was necessary as other normalization methods like DNA or insulin content could not be used due to the culture with other cell types. For the GSIS analysis, samples with a negative stimulation index were excluded, as this indicated an error in the measurement process such as insufficient washing.

4.4 Results

Formation of vascularized SC-ILC using a self-organized culture

For the vascularization of stem cell-derived islet-like clusters (SC-ILC) a self-condensation culture was established using human adipose-derived stromal cells (hASC) and hiPSC-derived endothelial cells (SC-ECs) in a collagen 1 (COL1)/Matrigel hydrogel (referred as vascularized co-culture, vCo-culture) (**Figure 12**, a). To enable live imaging of vascular structures during the culture, we used a GFP-expressing hiPSC line to differentiate SC-ECs. Within seven days of culture, the hydrogel started to condensate, and the migration of SC-ECs towards and the formation of vascular structures around the SC-ILC embedded in the hydrogel could be observed (**Figure 12**, b and **Extended Data Figure 1**, a). To ensure that the imaged GFP signal originated from SC-ECs, we stained the endothelial marker CD31 and observed a match of both signals. In the vCo-culture, SC-ILC and SC-ECs could be found in close proximity to each other suggesting a direct cell-cell contact (**Figure 12**, c). The culture with other cell types and the change of the standard medium condition can affect each cell identity. Therefore, staining of CD44 confirmed the unchanged identity of hASC after seven days in the vCo-culture (**Extended Data Figure 1,** b). As SC-ECs, SC-ILC, and hASC all require different mediums in routine cell culture, it was tested how different growth media influenced the vCo-culture. Therefore, the culture medium was optimized by evaluating SC-EC integrity and SC-β-cell functionality. We tested three different growth media, the stage 6 β-cell medium (S6M) and either a mix of S6M with the endothelial growth medium EGM2 or StemPro34 (both in a 50%:50% ratio). Both endothelial growth media also contained the EC growth factors VEGFA and FGF2. The integrity of SC-ECs was analyzed based on the level of vascular structure formation. In cultures with S6M, SC-ECs showed a lower vascular structure density than SC-ECs cultured in a mix of S6M with EGM2 or StemPro34. However, when analyzing SC-β-cell functionality with a glucose-stimulated insulin secretion assay (GSIS), the S6M condition showed the highest insulin stimulation index. Particularly with the EGM2:S6M medium, GSIS results showed impaired SC-β-cell stimulation in 6 out of 8 replicates in at least one stimulation cycle (**Extended Data Figure 1**, c, d). Based on these results it is possible to conclude that SC-β-cell functionality should be prioritized over the level of vascular structure formation and that the S6M condition should be used for further experiments. Next, the viability of cells in the vCo-culture was assessed. Therefore, the apoptotic state of cells was analyzed by staining for caspase 3 in its cleaved, activated form. Cleaved caspase 3 staining identified some apoptotic, mainly insulin-negative, cells within the SC-ILCs of the vCo-culture. However, the level of apoptotic cells appeared not significantly changed compared to SC-ILC from the suspension culture (**Extended Data Figure 1**, e).

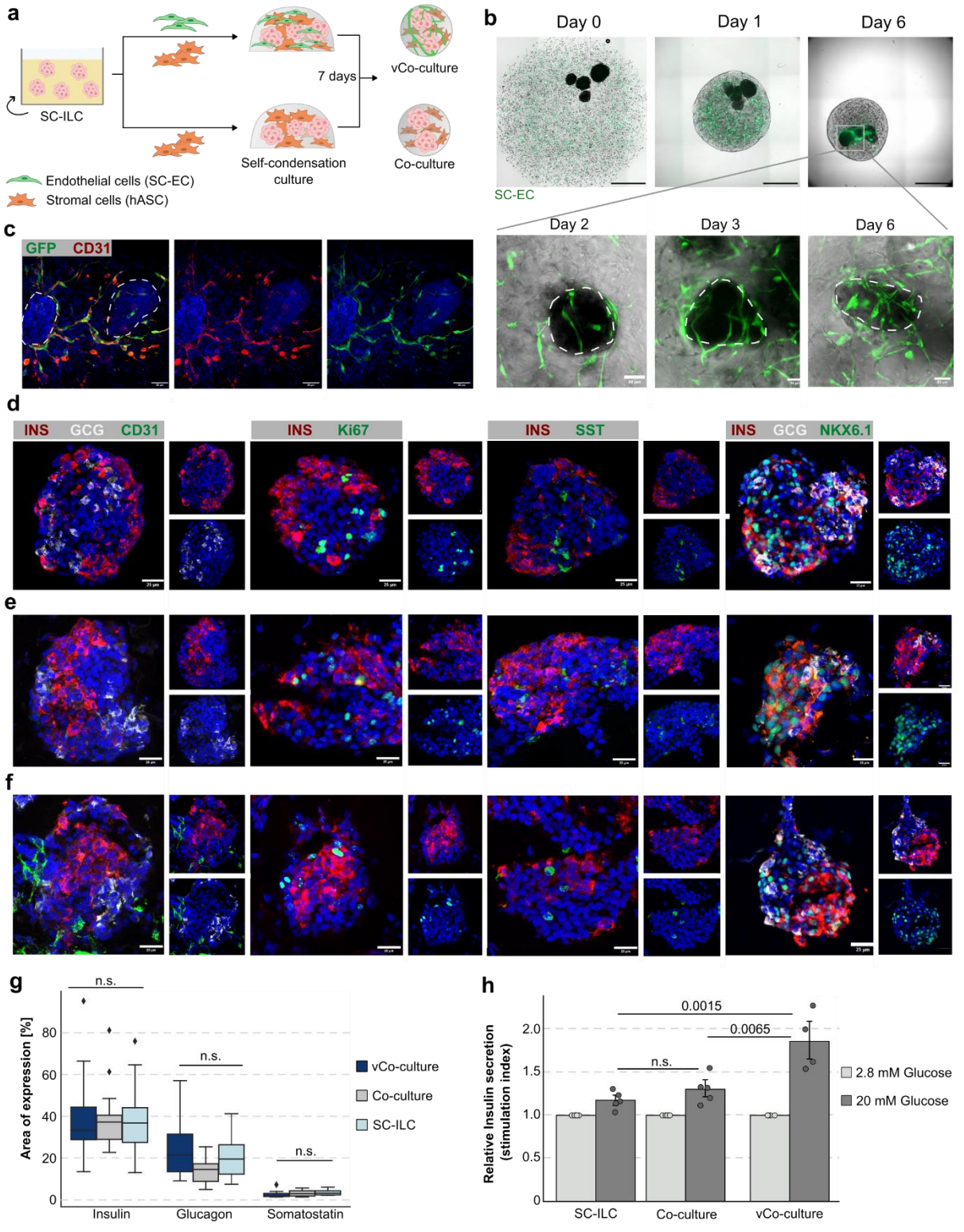

Figure 12: Establishment of a stem cell-derived vascularization model of SC-β-cells that enables increase in insulin secretion. **a** Differentiated stem cell-derived islet-like clusters (SC-ILC) were transferred in a hydrogel supported by stromal cells (hASC) and stem-cell derived endothelial cells (SC-EC, GFP positive) forming a self-organized vascularization model. Cells were co-cultured for seven days forming a vascularized co-culture (vCo). As a control, SC-ILC were cultured only with hASCs (Co). **b** Overlay of brightfield and fluorescent real-time images showing the condensation of the hydrogel and the formation of vascular

structures (green). Scale, 500 µm upper panel, 50 µm lower pannel. **c** Whole mount staining of a vCo-culture depicting the signal consistency of GFP and the endothelial cell marker CD31. Scale, 50 µm. **d-f** Known endocrine marker staining showing the expression of insulin (INS), glucagon (GCG), somatostatin (SST) and the transcription factor NKX6.1, the proliferation marker Ki67 and the endothelial cell marker CD31 in the respective samples (**d**, SC-ILC, **e**, Co-culture, **f**, vCo-culture). Scale, 25 µm. **g** Analysis of marker expression in the three sample groups. Immunofluorescent stainings were imaged, the area of expression analyzed and normalized to the DAPI expression. The data was acquired in 1-6 independent experiments with n ≥ 7. Significance was tested with a one-way ANOVA and Tukey's post-hoc test for each marker. **h** Glucose stimulated insulin secretion of the three sample groups depicted as stimulation index. *p* values of mean of experiment were calculated with a one-way ANOVA and Tukeys post-hoc test, 4-5 independent experiments were conducted with n ≥ 9. Error bars indicate an 85% confidence interval.

For the further evaluation of the vCo-culture, we conducted experiments with two control groups: i) SC-ILC in suspension culture to evaluate the effect of the hydrogel culture, and ii) SC-ILC cultured with hASCs in a COL1/Matrigel hydrogel to obtain a direct comparison of the effects of SC-ECs on the vCo-culture (referred to as Co-culture). To determine whether the cytoarchitecture of SC-ILC is maintained in the hydrogel cultures, immunofluorescent stainings were performed. All three conditions showed the expression of endocrine cell markers, including insulin/NKX6.1 positive SC-β-cells, glucagon positive SC-α-cells, somatostatin positive SC-δ-cells, and some proliferating cells (Ki67 positive) (**Figure 12**, d-f). When comparing the proportion of insulin-, glucagon, and somatostatin-expressing cells, no significant difference could be observed between the conditions (**Figure 12**, g). On average, SC-ILC in the three conditions contained 35 ± 2 % insulin and 17.5 ± 3.5 % glucagon-positive cells but only 2.5 ± 0.7 % somatostatin-positive cells. Also, proliferation did not change significantly between the conditions (**Extended Data Figure 1**, f). To analyze the response of vCo-culture SC-β-cells to glucose stimulation, a GSIS was performed and compared to the results of the two control groups. Here, insulin secretion was significantly increased in the vCo-culture. Surprisingly the Co-culture did not increase insulin secretion significantly in comparison to control SC-ILC, showing a benefit of the vCo-culture over both controls (**Figure 12**, h).

vCo-culture leads to a transcriptomic change in the SC-α-cell population

Next, we performed single-cell RNA sequencing (scRNAseq) to evaluate the transcriptomic changes of the endocrine cells associated with the vCo-culture in comparison to the SC-ILC control (**Figure 13**, a). With a Collagenase P/Accutase digestion of the hydrogel and SC-ILC, a live cell recovery rate >90% could be achieved, and retrieved cells were used as input for scRNAseq. The quality parameters of the sequencing run are shown in **Extended Data Figure**

2. After high-quality scRNAseq data filtering, single-cell transcriptomes of 11374 cells were obtained from both conditions. We could identify nine distinct cell populations using Leiden clustering[168] and two-dimensional data reduction (UMAP)[169] of the single-cell transcriptome data. The identified clusters could be annotated to different cell types according to previously published marker genes (**Figure 13**, b, c and **Extended Data Figure 3**). Cell clusters only found in the vCo-culture condition could be annotated to SC-ECs and hASC/stromal cells and showed the typical gene expression like *PECAM1, KDR,* and *FLT1* or *CD44, THY1,* and *PDGFRB*, respectively. In both conditions, endocrine cell clusters were observed including *INS, MAFA, MAFB, NKX6.1,* and *ERO1B* expressing SC-β-cells[235]; *GCG, ARX,* and *IRX1* expressing SC-α-cells[117]; and *SST* and *HHEX* expressing SC-δ-cells. We also identified enterochromaffin cells, a known side product of the hiPSC differentiation to SC-ILC. Enterochromaffin cells synthesize and secrete serotonin in the gut and express genes required for serotonin production (*TPH1* and *SLC18A1*)[236]. Further, another off-target cluster was identified expressing *KRT19, KRT17, SPP1,* and *CDH1* that we annotated to exocrine-like cells[237] (**Figure 13**, d and **Extended Data Figure 3**). SPP1 was previously identified as a marker of undifferentiated pancreatic progenitors and proliferative ducts in mice[238].

For the further and deeper characterization of the endocrine cells, all cells that showed a high expression of *CHGA* were subclustered (**Figure 13**, e-g). *CHGA* is a neuroendocrine secretory protein known to be expressed in endocrine cells[239]. The endocrine subcluster contained single-cell transcriptome data from 5646 cells from both conditions. As in the previous analysis, SC-β, SC-α, SC-δ, and enterochromaffin cells were identified. Since reduced proliferation is an important hallmark of mature β-cells[117], cell cycle genes were analyzed in the subcluster analysis. However, no difference in the distribution of proliferating cell types could be observed. The proliferating cluster contained cells from both conditions that expressed proliferation-related genes like *MKI67* or *PCNA* (**Figure 13**, h). In the cluster, mainly *INS*- and/or *GCG*-positive cells and enterochromaffin cells were found. This is consistent with the immunofluorescence staining (**Extended Data Figure 1**, f), which also showed no difference in proliferation between vCo-culture and SC-ILC.

Interestingly, SC-β-cells from both conditions clustered together and gene expression of known maturation and functional genes was comparable. SC-β-cells showed the expression of known β-cell identity genes like *INS, NKX6.1, ERO1B,* and *DLK1*[235] and mature β-cell markers including *MAFA, IAPP*, *UCN3, CPE, PCSK1,* and *ABCC8*[117]. For cells in the SC-δ-cell cluster, we observed the expression of the known δ-cell markers *SST* and *HHEX*, but also of ε-related genes like *GHRL* and *ACSL1* (**Figure 13**, h). Surprisingly, the main transcriptional difference between vCo-culture and SC-ILC was observed in the α-cell population. We, therefore, named the α-cell clusters according to their conditions: α-cells SC-ILC or α-cells

vCo-culture. SC-α-cells of both conditions expressed known α-cell identity genes, including *GCG*, *ARX, IRX1/2, LOXL4,* and *DPP4*[240,241]. Nevertheless, the transcriptomes from SC-α-cells of vCo-culture and SC-ILC barely overlapped, indicating a transcriptional difference apart from the known marker genes. Apart from the SC-α-cells, the proportions of cell types in the different conditions remained comparable (**Figure 13**, i). Compared to the immunofluorescence staining (**Figure 12**, g) we identified less SC-β cells within our scRNAseq (21.5 ± 2.5 %), whereas the population of SC-α-cells was slightly higher (25.5 ± 2.5 %). One explanation can be variations in the differentiation efficiency, which is still one main obstacle of SC-ILC differentiations[242,243]. However, when comparing our cell type distribution with other scRNAseq datasets[87,244] from SC-ILC, they are comparable, confirming that transcriptome and protein expression cannot be considered identical.

To better decipher the transcriptomic changes between SC-ILC and vCo-culture, we also performed scRNAseq of the Co-culture. We subclustered for cells of our main interest, *INS* and/or *GCG* positive SC-β- and SC-α-cells (**Figure 14**, a). Interestingly, a Pearson correlation analysis highlighted the transcriptomic similarity between vCo-culture and Co-culture, but a missing correlation to SC-ILC (**Figure 14**, b). Again, we saw a considerable convergence of SC-β-cell transcriptome profiles which contrasted with the SC-α-cells showing transcriptional variations between the conditions (**Figure 14**, c, d). We identified a SC-α-cell cluster that contained 60% of cells from the vCo-culture and 37% cells from the Co-culture. Whereas a second SC-α-cell cluster contained 95% cells of SC-ILC origin (**Figure 14**, e). Next, we reconstructed the single-cell data into developmental trajectories by calculating RNA velocity to gain a better understanding of the dynamic changes in SC-α-cell transcripts. Interestingly, the velocity lines revealed a distinct separation of the two identified α-cell populations indicating a transcriptomic change within the SC-α-cells in the different conditions. Next, we investigated whether the velocity lines were indicative of α-cell maturation. To this end, the gene enrichment score for upregulated genes obtained from grafted SC-α-cell and human islet α-cell single-cell datasets[88] was calculated within our single-cell transcriptome data. Strikingly, the enrichment score increased in the SC-α-cell cluster of vCo- and Co-culture origin, thus supporting a maturation effect of SC-α-cells in both cultures (**Figure 14**, f, g). The similar transcriptional profiles of SC-α-cells of both hydrogel models (vCo- and Co-cultrue) to the *in vivo* data additionally demonstrated that the models can mimic the *in vivo* microenvironment better than SC-ILC in shaking culture.

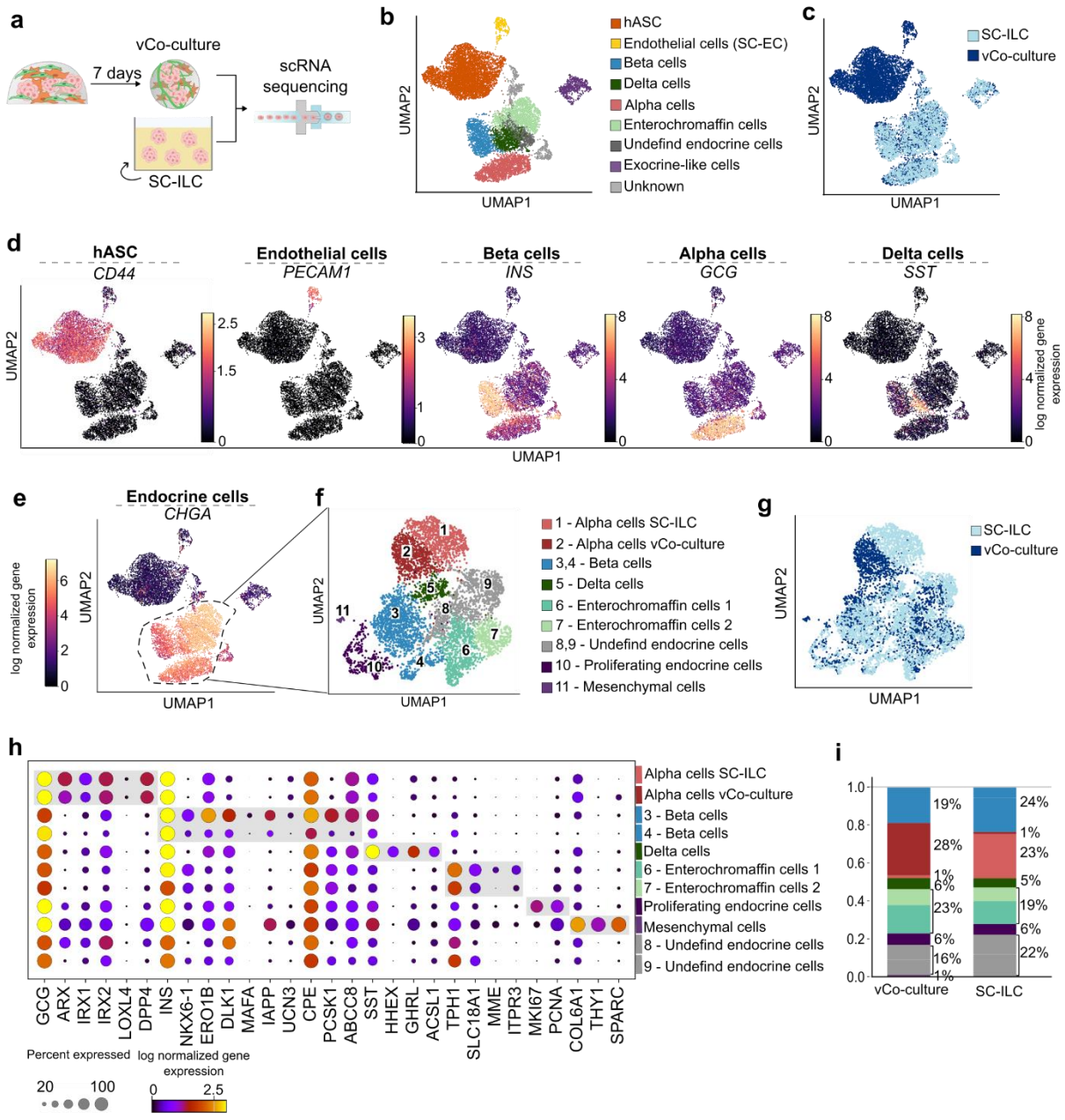

Figure 13: Single-cell transcriptomic analysis of vCo-culture shows a transcriptomic change in the α-cell population. **a** Cells from the vCo-culture and SC-ILC from the shaking culture were dissociated to single cells and used for 10x Genomics single-cell RNA sequencing. **b and c** Major cell clusters separated based on cell type (**b**) or vCo-culture versus SC-ILC origin (**c**) shown as cluster in a Uniform manifold approximation and projection (UMAP) plot. **d** Gene expression patterns of the selected cell marker genes used for cell cluster assignments. **e** Cells expressing the endocrine marker *CHGA* were subclustered to an endocrine dataset for further analysis. **f and g** Major endocrine cell clusters separated based on cell type (**f**) or vCo-culture versus SC-ILC origin (**g**) shown as cluster in a UMAP plot. **h** Normalized expression level of DEGs for the respective endocrine cell clusters. **i** Cell distribution according to the identified endocrine cell clusters.

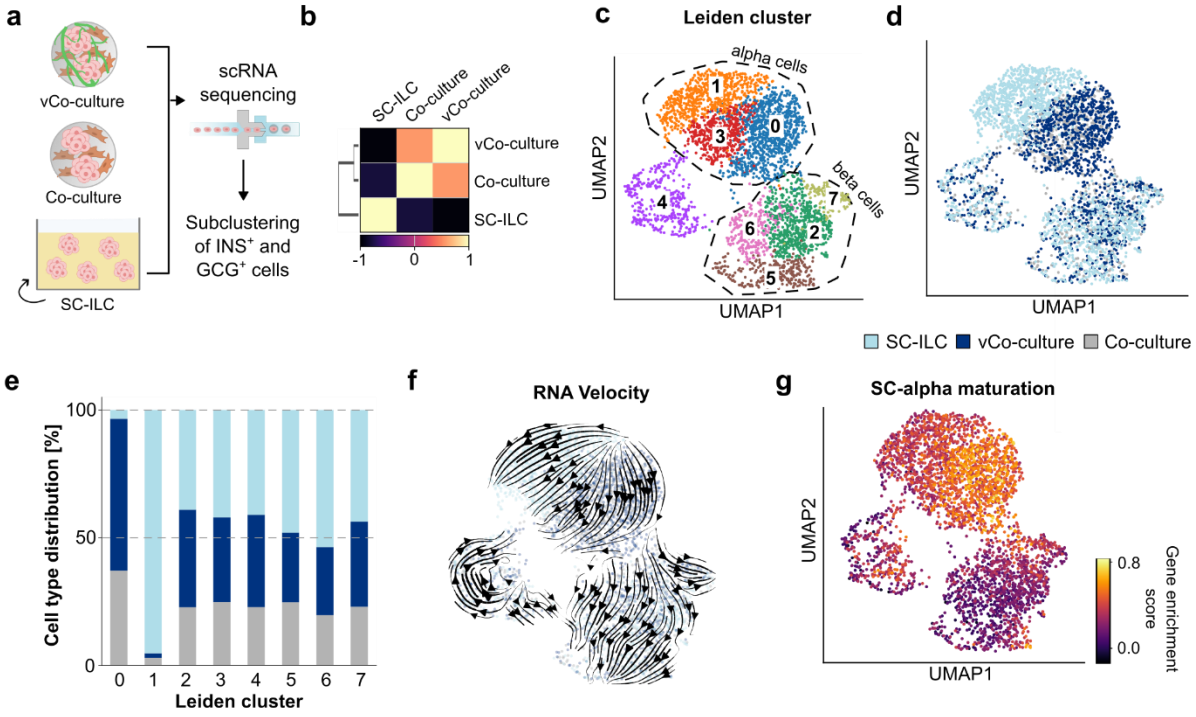

Figure 14: Subcluster of SC-β- and SC-α-cells indicates SC-α-cell maturation in vCo- and Co-culture. a ScRNAseq of the vCo-culture, Co-culture and SC-ILC was performed, datasets were concatenated, and endocrine cells of interest were subclustered. **b** Pearson correlation plot depicts a correlation of vCo-culture and Co-culture and a negative correlation to SC-ILC. **c** Leiden cluster (resolution 0.5) of the integrated scRNAseq dataset. Cluster of SC-α- and SC-β-cells are indicated. **d** UMAP plot of the three acquired single-cell transcriptomic data sets. **e** Barplot depicts the distribution of cells in the different Leiden clusters according to sample origin. Legend is the same as in d. **f** Single-cell transcriptomic velocity analysis. Velocity streamlines showed the transcriptomic state progression within the Leiden cluster. **g** Enrichment score of α-cell maturation genes from upregulated genes in grafted and human islet α-cells within our scRNAseq dataset.

Cell communication analysis reveals interaction pathways of SC-ECs and endocrine cells

ECs produce the islet ECM and interact with the endocrine cells [245]. Based on this knowledge, we wanted to know how the endocrine cells interact within the vCo-culture. To identify specific interaction pathways between SC-ECs and endocrine cells, the interaction profiles of the vCo-culture were compared to those of the Co-culture. We, therefore, performed an analysis of cell-cell communication using CellChat[246], identifying 92 interaction pathways between cell types. Identified pathways included secreted signaling, ECM-receptor and cell-cell interactions and were filtered for interactions between SC-ECs and endocrine cells. Within the vCo-culture, the endocrine cell types SC-β-, SC-α-, and SC-δ-cells showed the strongest interaction with SC-ECs functioning as strong signal senders towards SC-ECs. SC-ECs, on the other hand, showed an overall equal signaling strength towards all cell types in the culture but received most of the incoming signals. Expectedly, hASCs that represented the islet stromal cells in the

culture strongly interacted with SC-ECs but also showed interaction with the endocrine cell types (**Figure 15**, a). In comparison, the SC-ECs were missing as interaction partners in the Co-culture. Here, hASCs functioned as the strongest signal sender to endocrine cells whereas the endocrine cells showed similar interaction patterns to all cell types in the culture (**Extended Data Figure 4**, a).

As anticipated, ECM-receptor interaction pathways were found in the CellChat analysis highlighting the role of ECs and islet stromal cells in secreting the islet ECM and basement membrane[247]. In the vCo-culture, SC-ECs expressed the ECM molecules collagen IV, laminin α2, α4, α5, β1, β2 and γ1, the heparin sulfate proteoglycans perlecan and agrin[248] (*HSPG2* and *AGRN*), and fibronectin (*FN1*), all known to be important for β-cell functionality and insulin expression and secretion[245]. Consistent with this, SC-β-cells expressed the known integrins for ECM interaction, such as integrin β1, α1 and αv[249,250] and the non-integrin complex dystroglycan also expressed on islet cells as an alternative laminin binding site[251] (**Figure 15**, b, d, **Extended Data Figure 4**, b, **Extended Data Figure 5**, a). Expectedly, hASCs also contributed to the secretion of most ECM molecules and took over the function of islet stromal cells in forming the basement membrane (**Figure 15**, c). Besides, hASCs expressed collagen type III, which improves β-cell viability and function when it binds to its receptor *ADGRG1* on β-cells (**Figure 15**, e). Additionally, this interaction has been described as protective in T2DM[252,253]. In the Co-culture, hASCs expressed most ECM-related genes replacing the SC-ECs in their role of ECM-secretion (**Figure 15**, b, c and **Extended Data Figure 4**, b, c).

In the vCo-culture, we found pathways involved in the communication of SC-ECs and SC-β-cells either through direct cell-cell interaction or by secreted signaling. The identified signaling pathways can be broadly divided into interactions beneficial for angiogenesis, EC function, and migration or for improving the health, functionality, and insulin secretion of β-cells. For instance, SC-β-cells expressed angiogenic factors like *VEGFA*[68,254], *MDK*[255,256], *DLK1*[257,258], or *WNT5A,* that improves EC migration when binding to its receptor MCAM[259] (**Extended Data Figure 4**, b and **Extended Data Figure 5**, b). SC-β-cells expressed plexins that interact with their semaphorin ligands in ECs, influencing angiogenesis (pathways SEMA3-6)[260,261]. Further, we found pathways involving genes like *MIF*[262], *WNT5A*[263], *SORT1*[264], *ROBO1/2*[265] or *BMP5*[266] reported to be important for insulin secretion or β-cell development (**Extended Data Figure 5**, b). For example, it has been shown that the WNT5A-FZD3 axis is important for β-cell development[267], a signaling axis we identified between SC-ECs and SC-β- and SC-α-cells. Interestingly, pathways that involve signaling between SC-ECs and SC-β-cells were absent in the Co-culture, providing a possible mechanism for why insulin sensitivity was only increased in the vCo-culture. Those pathways included VEGF, SEMA4, and MIF signaling. MIF has been reported to be important for insulin secretion but also influences EC survival

and migration when binding to its receptor ACKR3 on ECs[268]. One signaling pathway exclusive for SC-β-cells and SC-ECs was the CALCR pathway involving *IAPP*, known to have glucoregulatory effects in β-cells. The binding of the *IAPP*-encoded protein amylin to its receptors on ECs (including CALCRL) has been reported to function in vascular biology and regulation of blood pressure[269,270].

Although the relationship between β-cells, ECs, and stromal cells is well-studied, little is known about the role of α-cells in this interaction. In the vCo-culture most interactions found were between SC-β-cells, SC-ECs, and hASCs. However, SC-α-cells also showed a strong signaling towards SC-ECs and expressed most angiogenic genes like *VEGFA*, *MDK, MIF,* and *WNT5A*. SC-α-cells expressed integrins and dystroglycan for ECM interaction and cadherins (E-cadherin, N-cadherin) for cell-cell interaction within the islet[271]. Further, SC-α-cells expressed *N-CAM* that has been reported as a regulator of glucagon secretion[272,273] and its receptor *FGFR1* has been associated with islet development, survival, and cell migration[274,275] (**Extended Data Figure 4**, b and **Extended Data Figure 5**, a and b). Thus, the CellChat analysis indicates that SC-α-cells are also involved in the interaction with SC-ECs and stromal cells, which can positively affect their function and maturation.

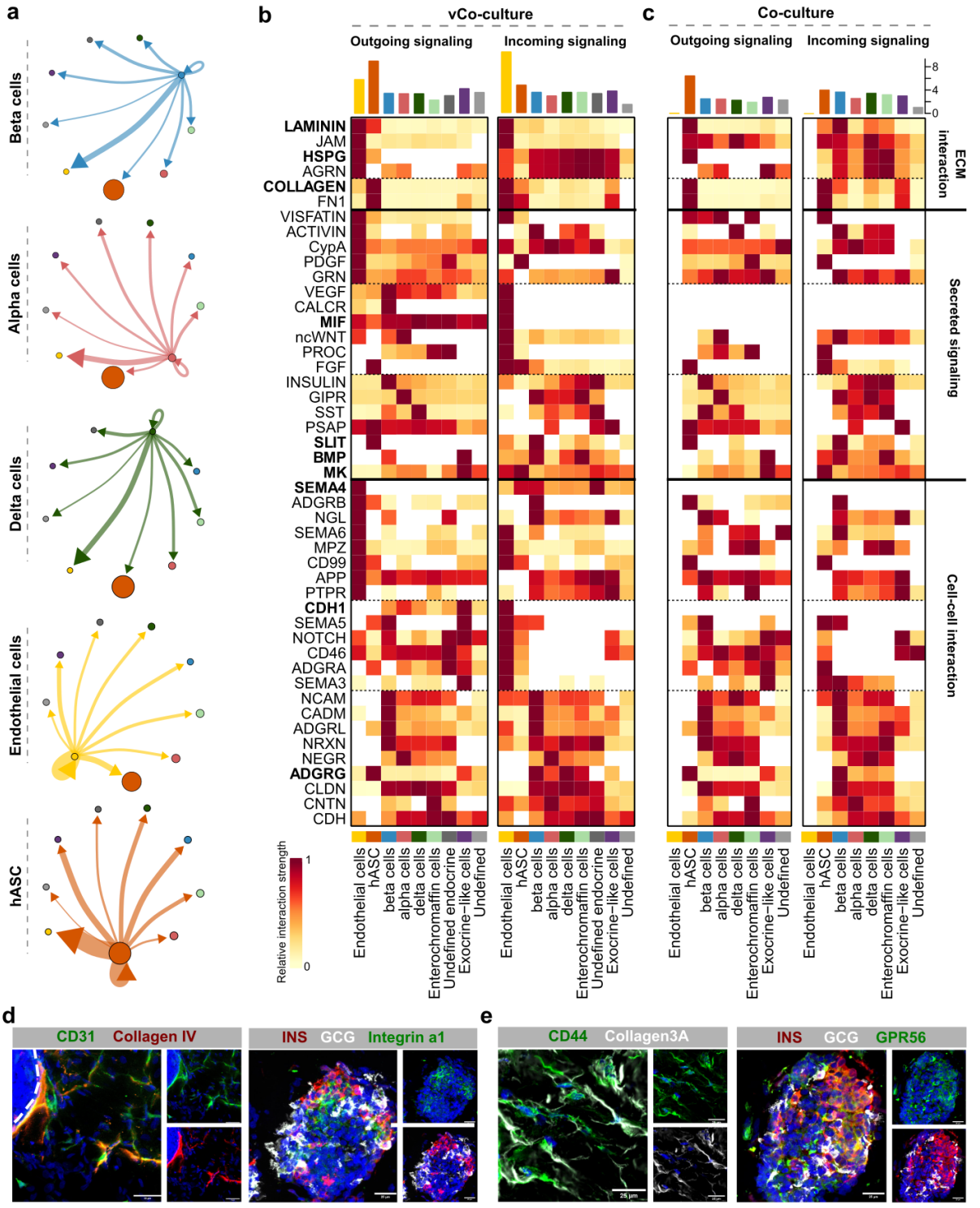

Figure 15: Cell communication analysis reveals SC-EC to endocrine-specific signaling pathways. a Cell-cell communication network of cell types in the vCo-culture. The signaling strength between the cell types is symbolized by the line thickness within the graph network, and dot size indicates the number of cells within one cell cluster. Cell type color code is according to b and c. **b-c** Selected signaling pathways of vCo-culture (**b**) or Co-culture (**c**) from the CellChat analysis, including secreted signaling, ECM, and cell-cell interaction pathways. The diagrams show the relative interaction strength of cell clusters and highlight the cell types with the strongest contribution to the respective signaling pathway, subdivided according to sender and receiver. **d-e** Representative z-projected immunofluorescence of the

vCo-culture (**d**) stained for SC-ECs expressing CD31 and Collagen IV (whole mount, scale, 50 µm, dotted line indicates a SC-ILC) and SC-ILC expressing insulin (INS), glucagon (GCG) or Integrin-α1 (scale, 25 µm) and (**e**) stromal cells expressing CD44 and Collagen-3A or SC-ILC expressing INS, GCG or GPR56 (*ADGRG1*). Scale, 25 µm.

Subtypes of SC-ECs from the vCo-culture express islet-EC-specific genes

The cell-cell communication analysis confirmed that islet-ECs and endocrine cells, especially SC-β-cells, are interdependent and influence each other's function and maturation. In the human body, islet-ECs are highly specialized and differ in their expression pattern from other ECs in the body[70]. To further investigate the transcriptional profile of SC-ECs in the vCo-culture, we extracted the SC-ECs from the scRNAseq data followed by Leiden clustering and DEG analysis (**Figure 16**, a). We identified three distinct SC-EC subtypes which we further characterized by Gene Ontology (GO) analysis. While in one cluster endothelial barrier and junction genes were upregulated, cells of the other clusters expressed pathways involved in ECM production and collagen organization or cell migration, respectively (**Figure 16**, b). SC-ECs of the barrier cluster expressed known endothelial barrier genes such as claudin-5 (*CLDN5*)[276], *CDC42*[277], *KLF2*[278] or *THSD1*[279], confirming a hallmark of EC function and vessel biology. Endothelin-1 (EDN1) is found in native islet blood vessels where it can stimulate insulin secretion by β-cells[70]. *EDN1* was expressed in the barrier cluster, however at a low level. Consistent with the CellChat analysis, cells of the ECM-secreting cluster expressed islet basement membrane components like *FN1* and *LAMA2* but also ECM-related genes such as *COL1A1, COL6A1* [280] or *LOXL1*[281]. Interestingly, collagen IV and nidogen, important islet basement membrane proteins[282], were expressed the highest in the barrier and migration cluster. Cells of the ECM-cluster expressed matricellular protein-encoding genes (*CTGF, THBS1, THBS2*) characteristic of islet ECs. Thrombospondin 1 (*THBS1*) is expressed almost exclusively by the islet endothelium and is important for postnatal β-cell functionality[70]. At the same time, connective tissue growth factor (CTGF) promotes β-cell regeneration and modulates the response to high glucose concentrations[70]. Consistent with studies in mice, SC-ECs expressed *SERPINA1*, a proteinase inhibitor specifically synthesized by islet-ECs[70,283]. Overall, this implies that SC-ECs express islet-EC identity genes and thus respond to the environmental stimuli in the vCo-culture. However, some islet-EC-specific genes were barely expressed, including *HGF*[284], important for glucose sensing and β-cell differentiation[70], or nephrin[285] (encoded by *NPHS1*) a highly specific barrier protein[70]. This indicates that SC-ECs in the vCo-culture are responsive to the islet microenvironment but have not yet fully matured into islet-ECs. In coherence with the observation that SC-ECs migrate towards SC-ILC in the vCo-culture, we identified a cluster of migratory character. SC-ECs from this cluster expressed genes involved in EC migration and angiogenesis, such as the VEGF-receptors *FLT1* and

KDR, confirming that SC-ECs react to angiogenic factors secreted by endocrine cells. In this context, angiogenesis-related genes such as *ADGRL4*[286], *TGFb1*[180] and *HEY1*[287] were upregulated, as well as CellChat identified migratory genes including *ACKR3* or *MCAM* (**Figure 16**, c-d).

To confirm that the observed transcriptional profiles are vCo-culture specific, we compared the data with the transcriptome of SC-ECs cultured with hASCs but without SC-ILC. In comparison to the vCo-culture, the culture parameters differed slightly in respect to the culture medium (EC growth medium StemPro34 medium) and the hydrogel composition (COL1 hydrogel). The analysis shows that ECM and tight junction gene expression were comparable between conditions. However, we observed a cell cluster from the vCo-culture that expressed islet EC-specific genes, including *SERPINA1*. In addition, neuroligin- and neurexin-encoding genes (*NRXN1* and *NLGN1*)[288] were expressed, which are thought to mediate direct cell contact with β-cells. The islet EC-specific genes *CTGF* and *THBS1* were also highly expressed by a subset of SC-ECs in the vCo-culture, but also to a lesser extent by the control cells. When comparing the DEGs of both conditions, genes related to VEGF signaling were expressed by SC-ECs of the vCo-culture, confirming the targeted interaction of SC-ILC with SC-ECs through angiogenic signaling. The genes include *CFL1*[289], which is involved in EC migration after VEGF stimulation; *EDF-1*[290], a regulator of VEGF-induced NO release; and *TM4SF18*[291], which is involved in VEGF-mediated angiogenesis. *THSD1* expression was also characteristic for SC-ECs from the vCo-culture, which has been reported to have endothelial barrier function[279] and mediate binding of ECs to ECM and basement membrane[292].

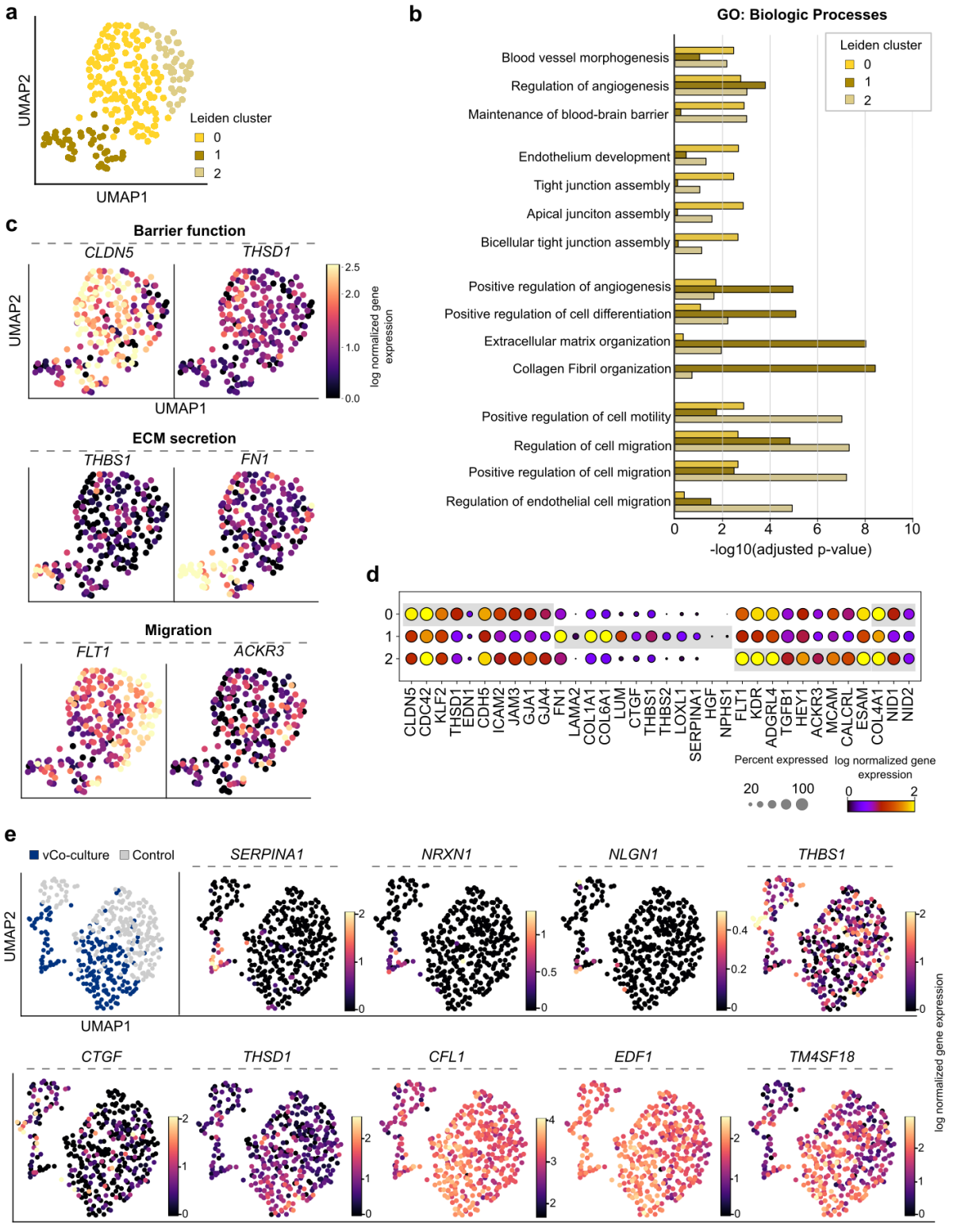

Figure 16: SC-ECs express EC-islet-specific genes in the vCo-culture. a SC-ECs were extracted from the scRNAseq data of the vCo-culture and analyzed. Leiden clustering revealed three distinct subtypes. **b** GO-term analysis indicates the specification of the SC-EC subclusters into endothelial barrier, ECM-secretion, and migration subtypes. For GO term analysis, all differentially expressed genes (DEG) were matched with the Biologic Processes database and significance was calculated. The plot shows selected GO terms of each

sample's 10 most significant pathways. **c** Plots show characteristic DEGs for each cluster. **d** Normalized expression level of DEGs for the respective SC-EC clusters. **e** Comparison of vCo-culture SC-ECs to a control without SC-ILC reveals transcriptomic differences. The control group contains SC-ECs cultured with hASCs in a collagen I hydrogel (StemPro-34 medium). Raw data was analyzed and subclustered together, and batch corrected with harmony[226].

SC-α-cells from the vCo-culture show increased sensitivity in glucagon secretion

Our data suggest a change in the transcriptome and maturation of SC-α-cells, possibly related to an interaction with SC-ECs and hASCs. To further analyze the functionality of SC-α-cells, we performed a glucose-dependent glucagon secretion assay (**Figure 17**, a). For this purpose, the response of the culture system to different glucose concentrations was measured. In mature α-cells, glucagon secretion is inhibited by glucose, and the δ-cell hormone somatostatin inhibits both glucagon and insulin secretion[222]. Indeed, SC-α-cells from vCo-culture and Co-culture showed significantly increased sensitivity to changes in glucose concentration compared to SC-ILC control. This effect was maximal at 7 mM glucose. In SC-α-cells from the vCo-culture, glucagon secretion was reduced by 40% compared to 2.8 mM. In contrast, SC-ILC were not responsive to 7 mM glucose. Interestingly, a higher glucose concentration (20 mM) was less inhibitory, and no significant difference in glucagon secretion was detected between vCo-, Co-culture, and SC-ILC. However, compared to the secretion at 2.8 mM, all samples showed significantly decreased glucagon secretion. That 7 mM glucose has a stronger inhibitory effect than higher glucose concentrations has also been reported by others[222,293]. Treatment of the cells with somatostatin significantly reduced glucagon secretion under all conditions. Here, SC-ILC showed less variability than vCo- and Co-culture, which can be explained by the diffusion gradient of the hydrogel. The data shows improved SC-α-cell functionality which can be attributed to the interaction with SC-ECs and/or hASCs and the microenvironment. To better understand the induced functional changes in SC-α-cells, we performed a Kyoto Encyclopedia of Genes (KEGG) pathway analysis of the SC-α-cell subpopulations (**Figure 17**, b). To this end, we observed a significant upregulation of genes involved in ECM-receptor interaction and focal adhesion in the vCo-culture, recapitulating the results of the CellChat analysis. Compared to Co-culture and SC-ILC, Glycolysis and Pi3K-Akt signaling pathways were also upregulated and are known to regulate islet function[117,294]. Changes in glycolysis indicate an altered metabolic activity and glucose sensing[295]. Indeed, glycolysis genes like *GCK, PGK1*, and *ENO1*[117] were expressed highest in SC-α-cells from the vCo-culture (**Figure 17**, c). Immunofluorescent staining for ENO1 confirmed the transcriptional observation on the protein level (**Figure 17**, d), indicating that the glycolytic activity of SC-α-cells is altered in the vCo-culture.

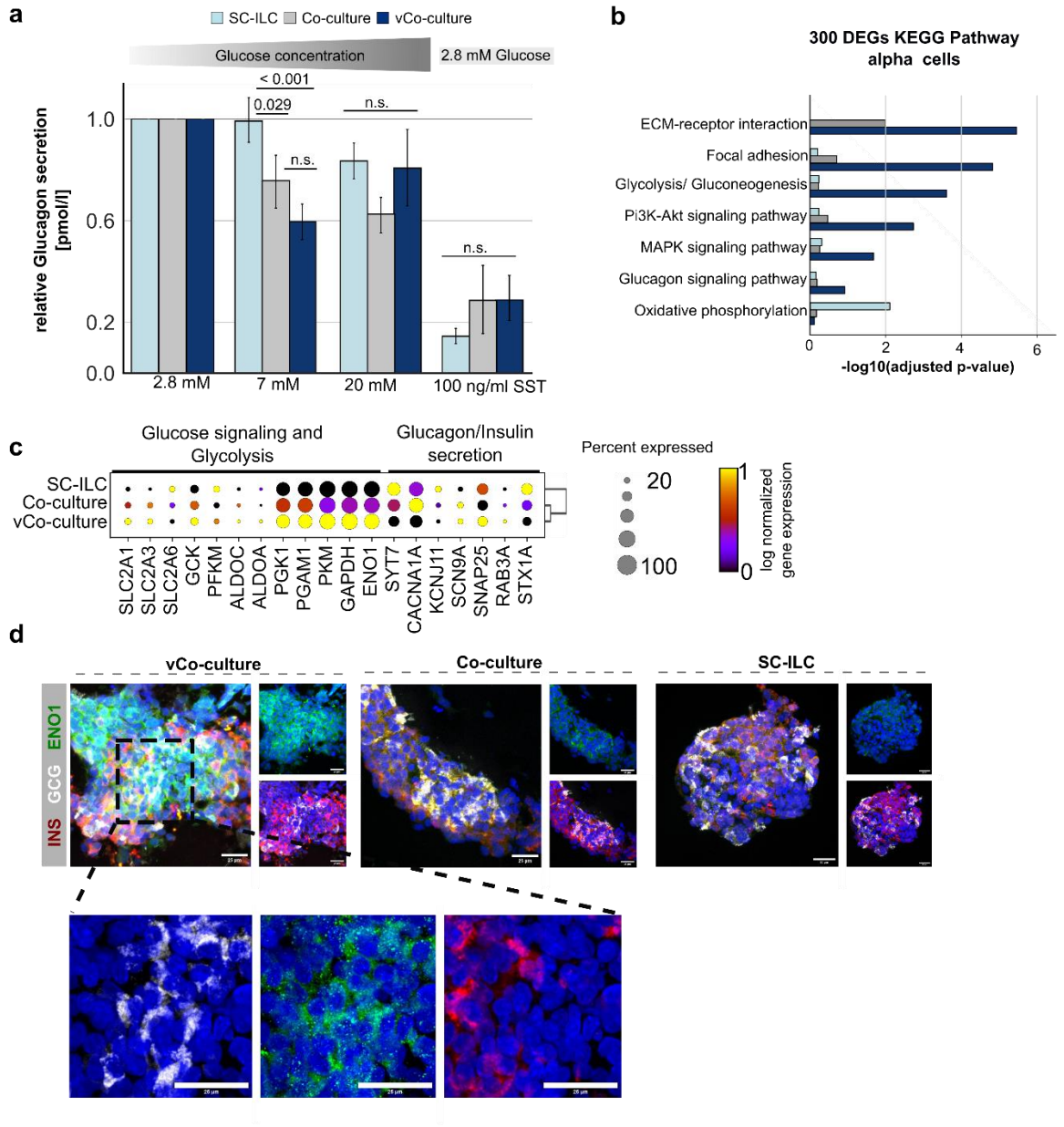

Figure 17: SC-α-cells from the vCo- and Co-culture show increased sensitivity in glucagon secretion. a Representative ELISA measurement of secreted glucagon from vCo-culture, Co-culture, and SC-ILC control. Cells were challenged sequentially with 2.8, 7 or 20 mM glucose with a 60-min incubation for each concentration. Cells were treated with 100 ng/ml somatostatin (SST) in 2.8 mM glucose to block glucagon secretion. n = 23-30 of 6 independent experiments. Significance was tested with a one-way ANOVA and Tukey´s post-hoc test. *P*-values are indicated in the figure. **b** KEGG pathway analysis reveals specific pathways for each condition. The 300 top DEGs of every condition were used for the analysis after gene ranking. Significantly upregulated pathways had a -log10(adjusted p-value) greater than 2. Other pathways of interest were selected and displayed. **c** Dotplot shows normalized gene expression of glucose signaling, secretion, and glycolysis genes. **d** Immunofluorescent staining of the glycolysis enzyme ENO1, insulin (INS), and glucagon (GCG). Scale bar, 25µm.

4.5 Discussion

Islet function highly depends on the microenvironment of the islet niche, including supporting stromal cells, the ECM, and a connection to vasculature to ensure optimal blood supply and the fast response of endocrine cells to changes in blood glucose concentrations[68]. Thus, the functionality of endocrine cells, like β- and α-cells, and the secretion of hormones can be influenced by microenvironmental cues, and islet-ECs have been shown to improve insulin secretion of β-cells[99]. The islet vasculature is particularly important for cell replacement therapies in T1DM as fast graft survival and function have been connected to successful revascularization at the transplant site[99]. As cadaveric donor material for islet transplantation is limited, SC-ILC hold great promise as an unlimited source of transplant material, enabling large-scale production.

In this study, we engineered the islet microenvironment using a vascularized co-culture model *in vitro* to investigate the interaction between islets, ECs, and stromal cells. For this purpose, we developed a stem cell-based model system. This offers the advantage that all cell types could be obtained autologously, or an established cell line could be used to differentiate SC-ILCs and SC-ECs. In addition, a hiPSC-based model could enable patient-specific research. As a stromal cell source, we used hASCs, which can also be obtained from the patient and have been reported to have immunomodulatory functions[94,220,296]. In our *in vitro* model, we observed the formation of vascular structures at the islet periphery, which enabled a direct cell-cell interaction between SC-ECs and islet cells. Since the culture medium used did not contain endothelial growth factors, the formation of vascular structures can be attributed to the secretion of angiogenic factors by the islet cells, which was also confirmed by the CellChat analysis. Consistent with previous studies[52,99], we show that the presence of vascular structures increased the response of SC-β-cells to physiological concentrations of glucose by increasing the insulin stimulation index. Importantly, the presence of stromal cells alone was not sufficient to increase the stimulation index significantly, demonstrating that the vasculature is critical for β-cell functionality.

Cell-cell communication analysis revealed signaling pathways between SC-ECs, SC-β-, and SC-α-cells, which were absent in the Co-culture (**Figure 15**). This was especially true for paracrine signals, which SC-β-cells and SC-ECs secrete. In the vCo-culture, we observed the secretion of angiogenic factors by SC-β- and SC-α-cells, including *VEGFA*[68], *MDK*[256], or *DLK1*[258]. This is consistent with findings *in vivo*, where the induction of angiogenesis and the formation of new blood vessels within the islets is crucial for islet function and development[254]. In addition, we identified signaling pathways that influence the functionality of both ECs and

SC-β-cells, such as WNT5A[259,267], IAPP[269,270], or MIF[262,268] signaling, highlighting the interdependence of both cell types. These interaction pathways disappeared when SC-ECs were absent from the culture. This implies that the paracrine interaction between SC-ECs and SC-β-cells critically influenced GSIS. Our findings suggest that treatment of SC-ILC with the identified growth factors could improve the *in vitro* maturation and differentiation of SC-ILC. Indeed, Chmielowiec et al[267] showed that treating endocrine progenitors with WNT5A can improve insulin secretion by SC-β-cells. However, we identified most interaction pathways not only between SC-ECs and SC-β-cells, but also SC-α-cells. Future experiments could, therefore, concentrate on screening the identified growth factors and studying not only insulin secretion but also glucagon secretion by SC-α-cells. Consistent with the role of ECs and stromal cells in secreting the islet ECM and the basement membrane[251,253], the CellChat analysis highlighted ECM interaction as one of the main signaling pathways within the vCo- and Co-culture. Although SC-ECs functioned as the main signal sender for ECM interactions in the vCo-culture, the pathways were still identified in the Co-culture analysis. Interestingly, stromal cells were now the signal senders of ECM interactions, except for the heparin sulfate proteoglycan agrin, taking over the role of SC-ECs. Our data indicates that vascular-derived ECM is important for endocrine functionality. However, comparing the GSIS results of vCo- and Co-cultures, our data suggest that paracrine signaling and direct cell-cell interactions of SC-ECs were responsible for the improved functionality of SC-β-cells in the vCo-culture.

Single-cell transcriptomic data, particularly velocity analysis, revealed a transcriptomic change of SC-α-cells in the vCo-culture and Co-culture (**Figure 14**). Although most research focuses on SC-β-cell differentiation and maturation, the mechanism underlying SC-α-cell maturation is particularly interesting. It has been shown that mature α-cells can improve β-cell functionality and that the interdependence of both cell types is critical for precisely regulating blood glucose levels[222,297]. Additionally, recent studies indicate that dysfunctional α-cells contribute to T1DM progression[298,299]. Since our data indicated the maturation of SC-α-cells, we investigated the functionality of the cells in a glucose-dependent glucagon secretion assay (**Figure 17**). Interestingly, SC-α-cells from both hydrogel cultures showed a significant improvement in glucagon secretion at physiological glucose concentrations (7 mM) compared to SC-ILC. However, blocking glucagon secretion with the δ-cell hormone somatostatin resulted in a lower stimulation index in SC-ILC compared to the two hydrogel cultures. A possible explanation for this is the diffusion gradient in the hydrogel, which slows down the effect of somatostatin compared to SC-ILC. In conjunction with the CellChat results, we conclude that SC-α-cell functionality was not significantly affected by the absence of SC-ECs but by the absence of stromal cells and a 3D environment. This indicated that ECM secretion and interaction strongly influence SC-α-cell functionality. Treatment with ECM molecules such as laminin or collagen

could therefore help to mature SC-α-cells *in vitro*. This conclusion was further supported by a KEGG pathway analysis, which showed an upregulation of ECM-receptor interactions in SC-α-cells from the vCo- and Co-culture. However, KEGG pathway analysis also identified the significant upregulation of glycolysis genes in SC-α-cells from the vCo-culture. The upregulation of glycolysis genes indicates improved glucose uptake and sensing. This is important for the proper function of adult islet cells[295] and is required to regulate insulin and glucagon secretion precisely. Thus, the interaction with SC-ECs might trigger a change in metabolic activity that could effect the long-term functionality of SC-α-cells. To investigate this further, we plan future experiments using MALDI (Matrix Assisted Laser Desorption/Ionization) imaging to examine glycolytic metabolites in all three conditions. Islet metabolism is an important component for islet functionality as has been already described by others[117,295]. Therefore, MALDI imaging could help to investigate our observations in the transcriptome data further and gain insight into how vascularization affects islet metabolism.

The scRNAseq analysis identified not only endocrine cells but also enterochromaffin cells considered as an off-target product of SC-ILC differentiation. The presence of enterochromaffin cells as a by-product of *in vitro* differentiation is controversially discussed. The discussions range from enterochromaffin cells as an off-target product and actual intestinal origin[235,244] to enterochromaffin cells as a pre-β-cell population of the fetal pancreas[87]. However, a high percentage of enterochromaffin cells indicates insufficient maturation, and sorting SC-α- and SC-β-cells using antibodies[242,244,300] could help to enrich more mature SC-ILC *in vitro*.

To test our vCo-culture for the purpose of islet transplantation, we have performed initial transplantation studies into the anterior chamber of the eye (ACE) of mice (data not shown). One advantage of the ACE as a transplantation site is that *in vivo* re-vascularization can be followed live post-transplantation[213]. This is particularly interesting because we assume that pre-vascularization of the SC-ILC *in vitro* improves re-vascularization after transplantation. However, we faced some problems with the ACE as a transplantation site. Although the ACE is well suited for islet transplantation[301,302], the vCo-cultures were larger than islets. This resulted in a considerably higher risk of infection for the mice, which meant that several animals had to be excluded from the experiment at an early stage. Thus, functional evaluation post-transplantation was not possible due to limited cell material. We, therefore, aim for an alternative transplantation site for future experiments, such as the kidney capsule or subcutaneous space. The subcutaneous space is an attractive transplantation site as it is easily accessible, allowing for easy surgical intervention and facilitating monitoring of the graft[213]. The subcutaneous space is comparatively avascular, but this can be overcome by pre-vascularization and possible encapsulation of the graft[303]. The most common

transplantation site in mouse studies is the kidney capsule, which allows the revascularization of the transplanted islets and intravital microscopy. However, whether the vCo-culture can be transplanted under the kidney capsule in terms of size remains to be proven. The hydrogel must also be optimized in the future, as Matrigel is unsuitable for human transplantation studies[304].

One limitation of the study was the limited number of vascular structures in the core of the SC-ILC. *In vivo,* islets are highly vascularized throughout the islet, providing each endocrine cell with rapid access to the blood system for hormone secretion. However, achieving a vascularization of the islet core *in vitro* is challenging. To generate an organoid with a homogeneous mixture of all cell types, reaggregation with ECs is usually performed[50]. However, when we applied this protocol with SC-ECs, stromal cells, and SC-ILC, the organoids were stable for a maximum of 1-2 days before endocrine cells and SC-ECs separated from each other and formed distinct aggregates. The mechanisms underlying this phenomenon remain to be investigated in the future. Despite this, we could show that the vascularization in the vCo-culture is sufficient to increase SC-β-cell functionality *in vitro*. The scRNAseq analysis of the SC-ECs revealed that SC-ECs responded to the islet microenvironment in the vCo-culture, but still need to mature further. Here, the induction of a flow system could help to mature SC-ECs with applied shear stress. Whether a further maturation of SC-ECs could also be beneficial for vascularizing the islet core remains to be tested. This study investigated the effects of a hydrogel culture with SC-ECs and/or stromal cells on endocrine functionality. Whether cultivation in a hydrogel alone without supporting cells already has an effect on the endocrine cells, therefore, remains open.

In summary, we have developed a vCo-culture model for SC-ILC vascularization that improved the functionality of SC-β- and SC-α-cells. Our model system provides new insights into SC-α-cell maturation and revealed potential supplements for recently published[222] SC-α-cell differentiation protocols. We demonstrate the importance of cell-cell communication with ECs, particularly for the functionality of SC-β-cells. Our model thus provides a platform with potential utility for cell replacement therapy and disease modeling and gives new insights into the biology of α- and β-cells. We present a culture model that could be generated fully autologously, the next step for islet transplantation and future patient-derived diabetes research.

4.6 Extended Data

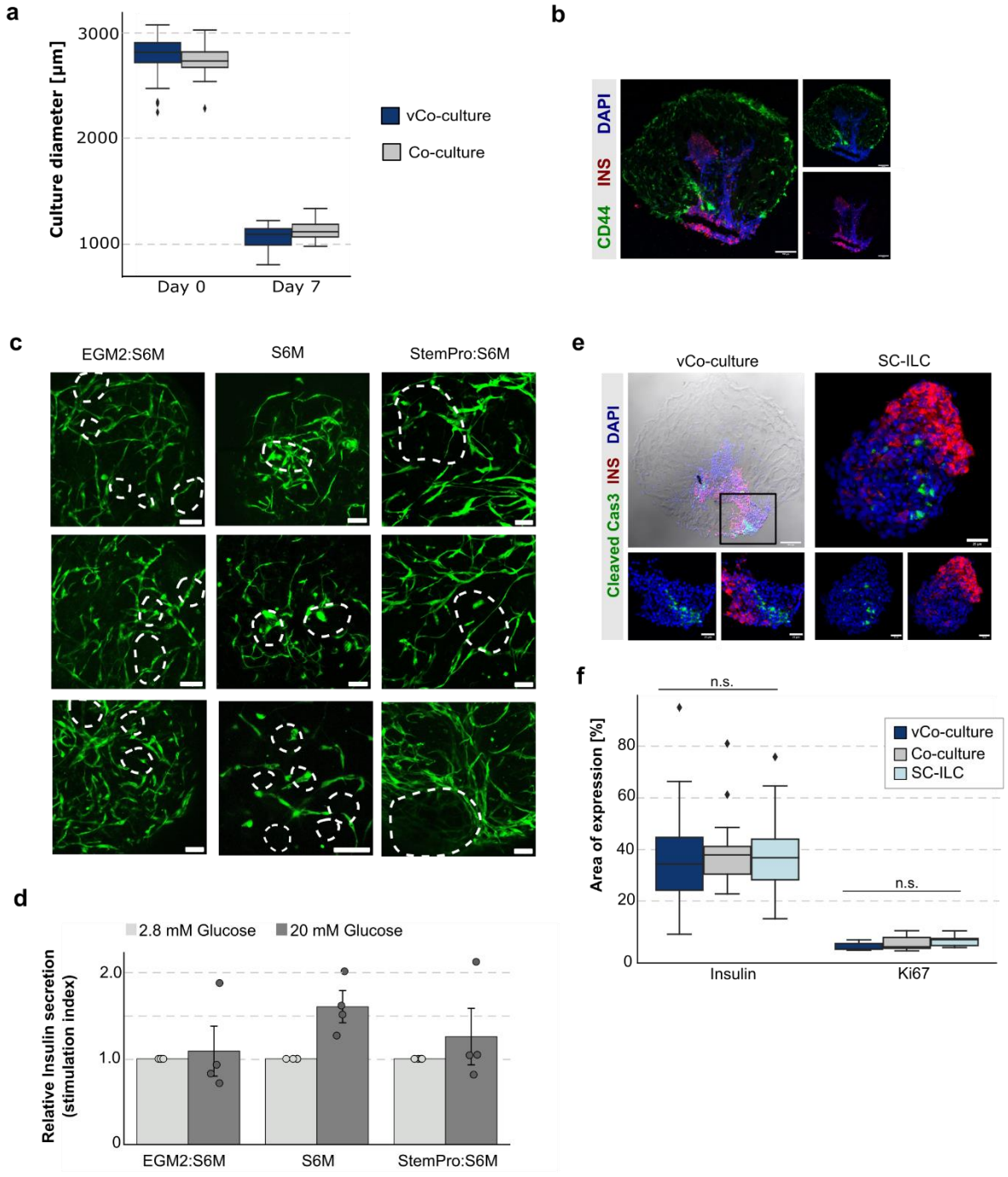

Extended Data Figure 1. Related to Figure 12. Optimization of culture conditions and characterization of vCo-culture. a Culture diameter reduction over the time of culture in vCo- and Co-culture. n>45 in 2 independent experiments. **b** Staining of hASC marker CD44 and insulin (INS) in the vCo-culture. scale bar, 100 µm. **c-d** Optimization of medium condition was evaluated by vascular structure formation of SC-ECs (**c**) and insulin secretion of SC-β-cells (**d**). Medium conditions included the β-cell medium S6 (S6M) or a mix of S6M with two different EC media: EGM2 or StemPro. Scale bar, 100 µm. **d** Stimulation index of insulin secretion in different medium conditions of the vCo-culture. n = 7-12 in 4 independent experiments, error bars indicate a confidence interval of 85%, mean of experiment is depicted. **e** Staining of the apoptotic marker cleaved caspase 3 in the vCo-culture and SC-ILC control from the

suspension culture. scale bar, 100 µm on the upper left image, 25 µm for all other images. **f** Analysis of insulin and Ki67 expression in the three sample groups. Immunofluorescent stainings were imaged, the area of expression analyzed and normalized to the DAPI expression. The data were acquired in 1-2 independent experiments with n ≥ 7.

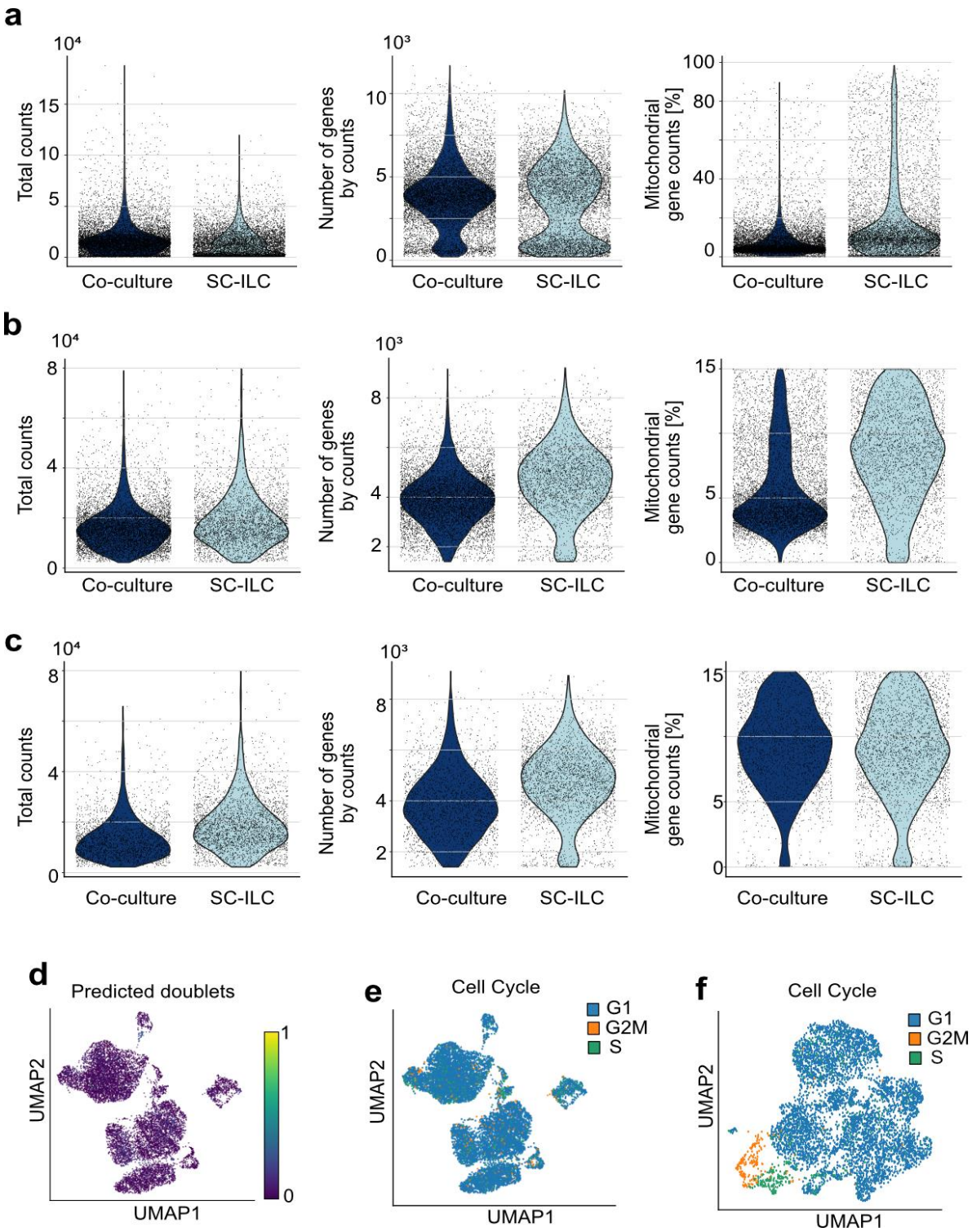

Extended Data Figure 2: Related to Figure 13. Quality control of the single-cell RNA sequencing data of integrated vCo-culture and SC-ILC dataset. a-c Violin plots depict total cell counts, number of genes by counts, and percentual mitochondrial gene counts of scRNA sequencing run without (a) and with the cell filtering procedure (b) and after endocrine subclustering (c), respectively. **d** Doublet analysis before filtering and subclustering confirms

high single cell encapsulation efficiency within the 10x run and thus a low doublet count. **e-f** Uniform manifold approximation and projection (UMAP) plot depicts cells in cell cycle before and after endocrine subclustering.

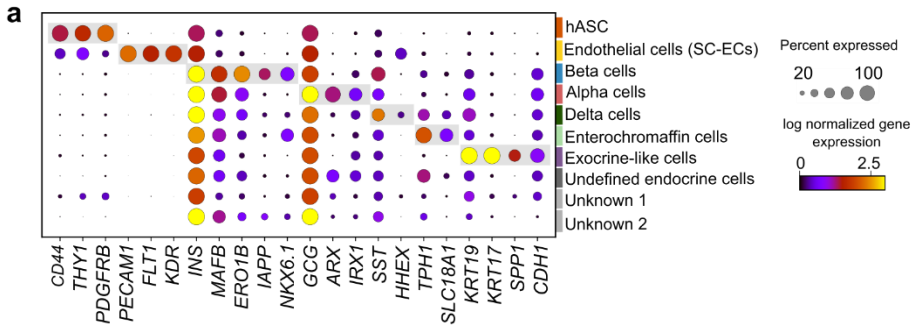

Extended Data Figure 3. Related to Figure 13. Characterization of the vCo-culture by single-cell RNA sequencing (scRNAseq). a The dot plot shows the normalized cluster mean expression of marker genes used for cell type annotations in the concatenated data of vCo-culture and SC-ILC.

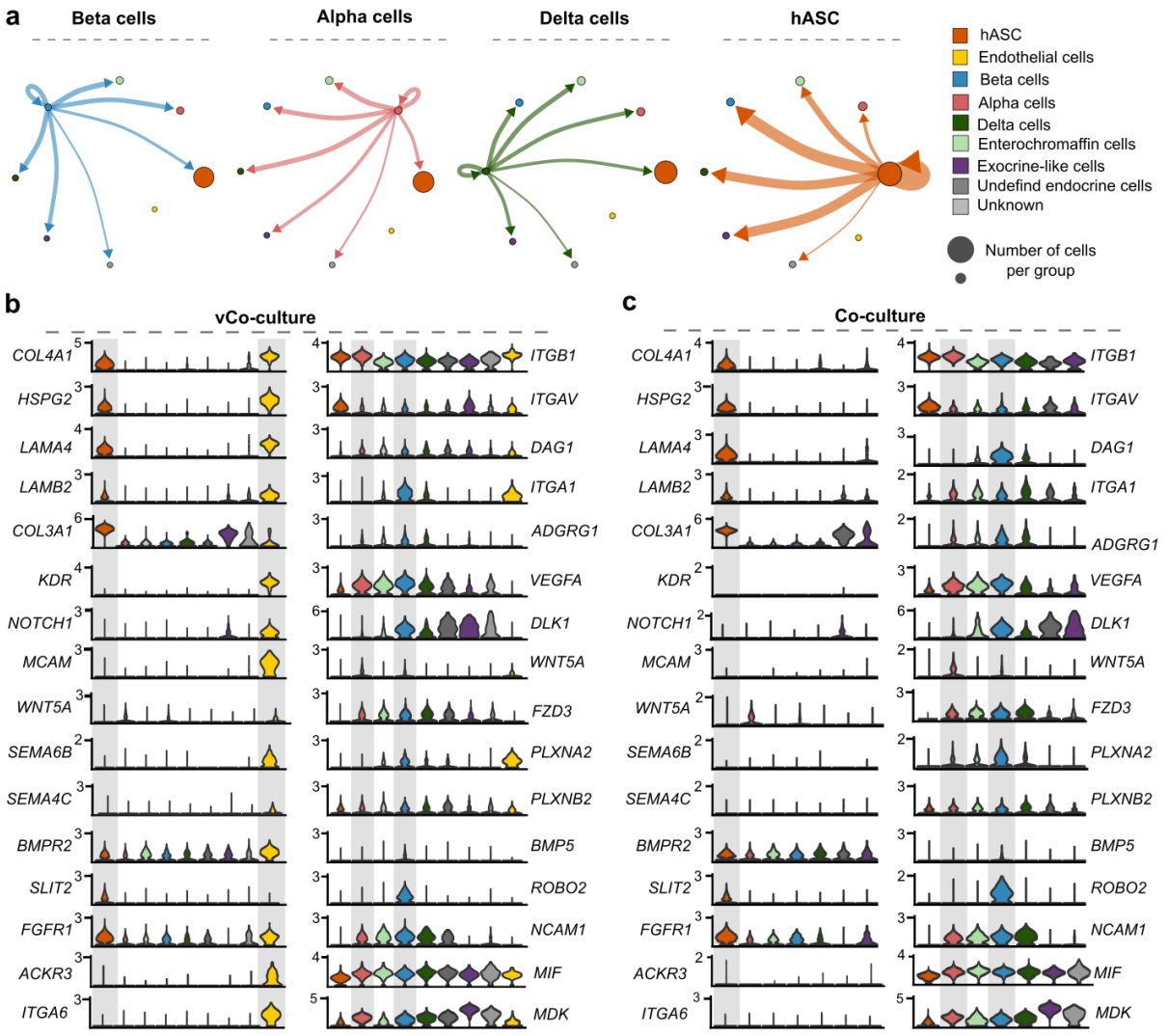

Extended Data Figure 4. Related to Figure 15. Cell-cell communication analysis reveals differences in vCo- and Co-culture signaling. a Cell-cell communication network of cell types in the Co-culture. The signaling strength between the cell types is symbolized by the line thickness within the graph network. **b-c** Violin plots depict the expression of genes of interest from the CellChat analysis in vCo-culture (**b**) or Co-culture (**c**).

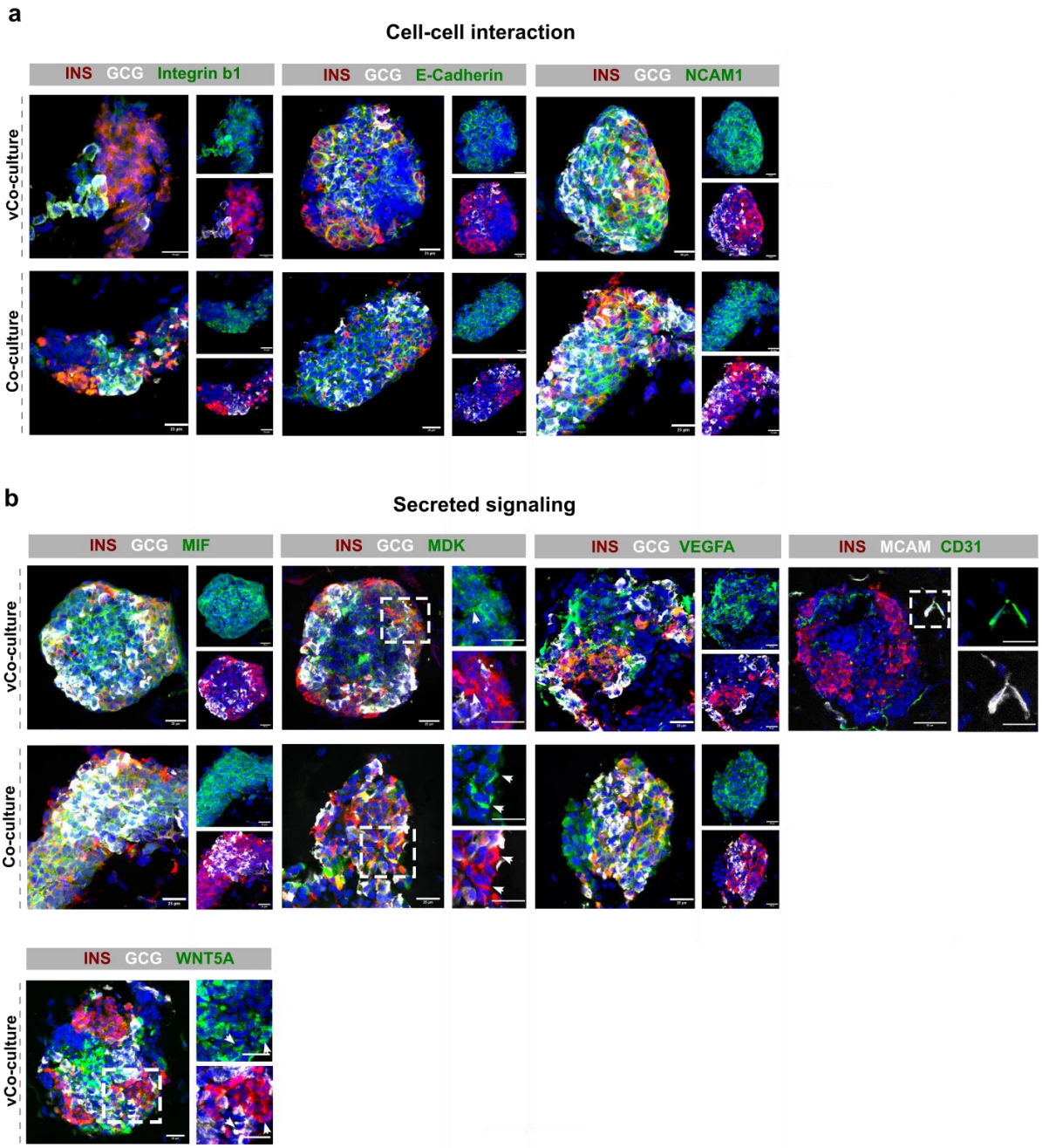

Extended Data Figure 5. Related to Figure 15. Cell-cell communication marker expressed in vCo- and Co-culture. Representative z-projected immunofluorescent images of CellChat identified markers such as (**a**) insulin (INS) and glucagon (GCG) and cell-cell interaction proteins integrin-β1, E-cadherin, or NCAM1 and (**b)** proteins involved in secreted signaling like MIF, MDK, VEGFA, MCAM or WNT5A. Scale, 25µm.

5 Direct monitoring of insulin secretion in stem cell-derived β-cells by impedance spectroscopy

5.1 Declaration of contribution

In this chapter, the maintenance of stem cell-derived islet-like clusters (SC-ILC), the analysis of supernatants by ELISA, staining, and imaging were conducted by me. Differentiations of hiPSCs to SC-ILC were done by Nicole Rogers. Impedance measurements were done by Franziska Zitzmann and Heinz-Georg Jahnke. The analysis of the impedance spectra was done by Heinz-Georg Jahnke. For the experimental design of the study, I provided the biological knowledge, whereas Heinz-Georg Jahnke and Franziska Zitzmann provided the technical knowledge. The study was advised by Matthias Meier. Figure design and manuscript writing was done by me.

5.2 Introduction

Diabetes mellitus is a metabolic disorder characterized by insufficient levels of insulin and can be mainly grouped into type I and type 2 diabetes (T1DM and T2DM). Over 500 million people are suffering from diabetes worldwide and incidences are rising[71]. The pathogenesis of diabetes involves the destruction or dysfunction of insulin-producing β-cells. In T1DM, β-cells get destroyed by an autoimmune reaction leading to hyperglycemia. Although first-line medication treats hyperglycemia and the symptoms of insulin resistance, this does not restore the lost β-cell mass and function. Here, cell-replacement therapy is one possible approach to restore the lost β-cells and has the potential of re-establishing glycemic control, decreasing the risk of hypoglycemic events, and preventing life-threatening complications associated with diabetes. However, donor material shortage and the reliance on immunosuppressive drugs inhibit the widespread adoption of pancreatic or islet transplantation therapies[75]. Human induced pluripotent stem cells (hiPSCs) can be differentiated into insulin-secreting β-like cells (SC-β-cells) in a multi-stage protocol following pancreas development[85]. The generated stem cell-derived islet-like cluster (SC-ILC) have several applications in diabetes research, like their use for cell replacement therapy[96,216], modeling islet development and function[305,306], studying diabetes onset[307], or testing anti-diabetic drugs[308–310]. However, differentiation efficiency is still very variable and SC-ILC are of an immature phenotype [65,311]. Thus, further effort is necessary to improve the heterogeneity, maturation, and function of SC-ILC to gain an authentic and reproducible cell model[312]. Especially in the context of cell replacement therapy, screening of the differentiated SC-ILC is necessary to identify mature cells and to improve differentiation

protocols that still need further adaptation. The main characteristic of functional β-cells is their insulin secretion after glucose stimulation. To this end, a glucose-stimulated insulin secretion assay (GSIS) is performed, followed by the evaluation of secreted insulin with an enzyme-linked immunosorbent assay (ELISA). This assay is elaborate in time and cost (>$2/well[116]), hindering high-throughput screenings of SC-ILC. Therefore, establishing a reliable, fast, and cost-effective method for detecting insulin is necessary to expand SC-β-cell screening not only for maturation tests but also for diabetic drug screening.[313].

One monitoring technique for cell culture systems is impedance spectroscopy, which has proven to be an automation-compatible technique for label-free real-time monitoring of 2D and 3D cultures. In combination with microcavity arrays (MCA), impedance spectroscopy is suitable for 3D cell culture screening, e.g. for analyzing changes in morphology, testing drug penetration and cytotoxicity[111], or the electrophysiological properties of cardiomyocytes[112]. In impedance spectroscopy, changes in current/voltage through the cells are measured while a frequency shift is performed. Like this, electric resistance and capacitance of cells can be monitored[107].

In this study, we used impedance spectroscopy to monitor insulin secretion by SC-ILC. To this end, we performed GSIS on an MCA chip and recorded the impedance changes in individual SC-ILC. In addition to recordings with low and high glucose solutions, the impedance measurement correctly mapped the inhibition of insulin secretion after treatment with a Ca^{2+} influx inhibitor. Overall, we report a new, fast, non-invasive method for screening SC-ILC insulin secretion that could replace expensive ELISA analysis and is suitable for high-throughput screening.

5.3 Materials and Methods

Differentiation and culture of stem-cell derived β-cells

HiPSCs (For this study, an unpublished reporter line was used that was adapted from the published mCherry C-peptide clone HMGUi001-A-8[223]. For this study, only the mCherry C-peptide expression was of interest.) were cultured under standard conditions on Geltrex coated plates (Life Technologies, Cat#A1413302) in StemMACS iPS-Brew medium (Miltenyi Biotec, Cat#130104368). HiPSCs were differentiated into stem cell-derived islet-like clusters (SC-ILC) according to a published protocol[85]. In brief, hiPSCs were single-cell dispersed and seeded at 0.6 x 10^6 cells ml^{-1} in 30 ml spinner flasks or six well ultra-low attachment plates (ULA) with 10µM Rock inhibitor Y-27632 (Biozol, Cat#APE-A3008-10). In a 6-stage protocol, cells were differentiated into β-like cells following endocrine development. At the beginning of stage 6 (S6), cells were reaggregated to reduce the number of off-target products. Therefore, cells were washed with PBS-/-, dispersed with Accutase (Sigma Aldrich, Cat#A6964) for approximately 30 min, and filtered through a 40 µm cell strainer. Single cells were seeded at 1 x 10^6 cells ml^{-1} in ULA plates (S6 medium with 10µM Rock inhibitor Y-27632) and placed on an orbital shaker at 100 rpm at 37°C and 5% CO_2. Medium was changed every day until S6 day 14, then the medium was changed every other day. Differentiated SC-ILC could be identified by a positive mCherry signal indicating insulin-positive SC-β-cells. The composition of the S6 medium can be found in **Table 4**.

Microcavity fabrication

Microcavities were produced by the selective laser-induced etching (SLE) process in fused silica glass as reported before[314]. In brief, microcavities were designed as a truncated pyramid structure with a side length of 400µm and a height of 2/3 of the side length. The glass substrate was processed with a 1030nm Yb: YAG laser and etched in KOH solution. Electrodes were fabricated using a lift-off process.

Hormone secretion assay measured with impedance spectroscopy.

For impedance measurement, SC-ILC were handpicked according to size and mCherry positivity and were starved in 2.8 mM glucose in Krebs-Ringer-buffer (KRB, 129 mM NaCl, 4.8 mM KCl, 1.2 mM KH_2PO_4, 1.2 mM $MgSO_4$, 2 mM $CaCl_2$, 24 mM $NaHCO_3$) for 2 hours. Afterwards, SC-ILC were transferred to microcavities, and impedance spectra were recorded as previously described[112,314]. Briefly, bioelectronic analysis was performed with a high-precision impedance analyzer Agilent 4294A and the self-developed IMATadvanced software (500 Hz–5 MHz, 51 frequency measurement points, ±10 mV amplitude, 0 V bias potential). Each Microcavity array (MCA) was fabricated to contain twelve individual microcavities for 3D cell culture. Low glucose (2.8 mM) impedance spectra were recorded for 10 min before changing the buffer to 20 mM high glucose concentration. The corresponding glucose

concentration was added to the buffer on the chip. Impedance spectra in high glucose were recorded for 1 hour. Afterwards, KCl was added to the buffer reaching a concentration of 30 mM KCl, followed by 1 hour incubation. After each incubation step, 150 µl buffer were taken for insulin ELISA analysis. The total volume of buffer within one medium reservoir was 1500µl. Collected supernatants were analyzed for insulin concentration with an Ultra-sensitive Insulin ELISA kit (Mercodia, Cat#10113201) according to manufacturer's protocol. For inhibitor tests, buffer contained 250 µM diazoxide (Sigma, Cat#D9035).

Microscopy and immunofluorescence

For immunostainings, cells were fixed in 4% paraformaldehyde for 30 min at RT. Cells were washed in PBS-/- and dehydrated at RT using a sucrose gradient of 10% (w/v) and 30% (w/v) for 2 h each, followed by overnight incubation in a 1:1 mixture of 30% sucrose and tissue freezing medium (Leica, Cat#14020108926) at 4°C. The next day, samples were embedded in cryo tissue molds in tissue freezing medium on dry ice. Samples were sectioned into 10 µm slices at the cryostat for immunofluorescence staining.

For staining, sections were dried for 30 min at RT, rehydrated in PBS for 20 min, and permeabilized for 20 min at RT (0.1 M glycine, 0.1% TritonX-100 in PBS). Next, samples were blocked in blocking buffer (10% FCS, 0.1% BSA, 3% donkey serum, 0.1 M glycine in PBS-Tween (0.2 %)) for 2 hours at RT. Sections were incubated in blocking buffer with primary antibody overnight at 4°C. Primary antibodies were diluted in blocking buffer as follows: guinea pig anti-Insulin (1:300, Bio-Rad, Cat#53300104G), mouse anti-Glucagon (1:2000, Sigma, Cat#G2654), rabbit anti-cleaved caspase3 (1:300, Cell Signaling, Cat#9661S).

The next day, samples were washed 3 times for 10 min in PBS-/- before incubated with secondary antibody for 3 hours at RT. All secondary antibodies were diluted 1:500 in blocking buffer: anti-guinea pig Cy3 (Biozol Diagnostica, Cat#JIM706165148), anti-mouse AlexaFluor647 (Invitrogen, Cat#A31571), anti-rabbit AlexaFluor488 (Invitrogen, Cat#A21206).

Sections were washed again 3 times in PBS, mounted in Vectashield mounting medium (Vector Laboratories, Cat#VEC-H-1900-10) and imaged with a confocal microscope (LSM-880, Zeiss).

5.4 Results

Impedimetric analysis allows monitoring of insulin secretion by stem-cell derived β-cells

For the impedimetric analysis, hiPSCs were differentiated to SC-ILC in a six-stage protocol[85] following pancreas development. As in *in vivo* islets, SC-ILC contain different endocrine cell types, including SC-β- and SC-α-cells. Both cell types were verified within the SC-ILC by staining of known markers and are represented by insulin and NKX6.1 positive SC-β-cells and glucagon positive SC-α-cells (**Figure 18**, a). For the impedimetric monitoring, an MCA-based sensor chip consisting of twelve individual square microcavities with a diameter of 400µm was used. Gold electrodes were attached to four sides of each cavity, enabling the measurement of impedimetric signals. The fabrication of the MCA chip was done as previously described[314] and involved i) microcavity structuring in fused silica substrates using a laser etching process, ii) patterning of the gold electrodes, and iii) the assembly of all parts with a medium reservoir. Each microcavity allowed for the analysis of a single SC-ILC and the monitoring of bioelectric alterations within the SC-ILC. Given that we aimed to analyze SC-β-cell functionality with impedance spectroscopy, a GSIS assay within the MCA chip was performed and the impedance spectra were recorded in real-time. The MCA-chip setup enabled the screening of up to twelve SC-ILC on a single islet level (**Figure 18**, b, d, e). SC-ILC diameter usually ranges from 100µm to 250µm, and clusters contain up to a few thousand endocrine cells[315]. Thus, the measured impedance is determined by all cells within the electric field contributing to the impedance spectra with the cellular capacitance (cell membrane capacitance), the cellular resistance (cell membrane resistance), and the intercellular resistance[111] (**Figure 18**, c).

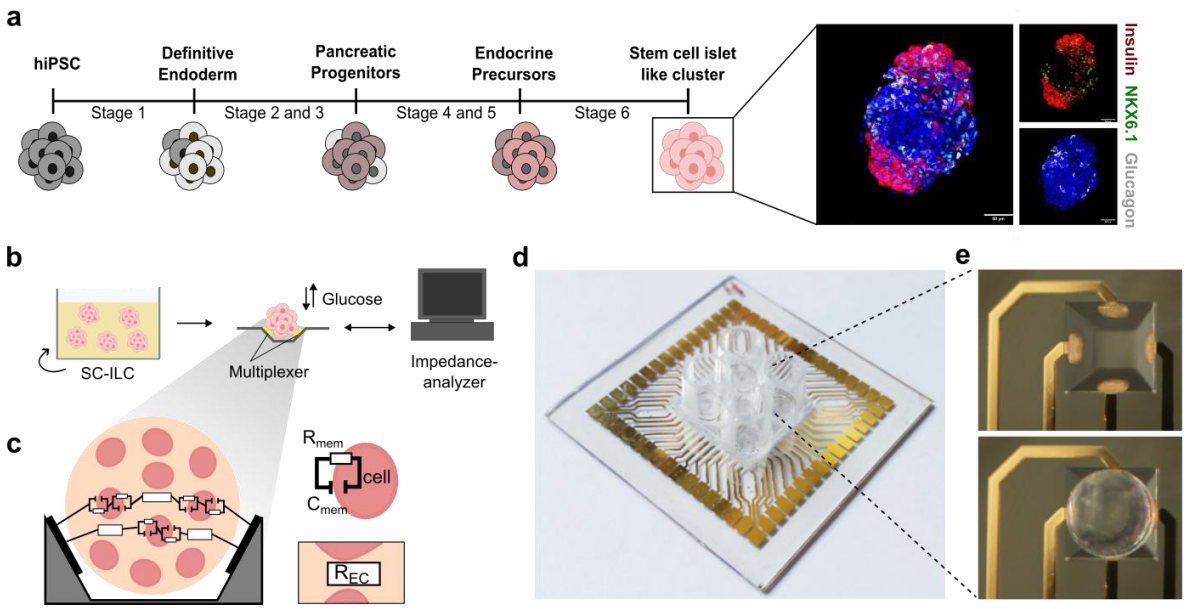

Figure 18: Microcavity array for impedance analysis of stem-cell derived β-cells. a Differentiation of hiPSCs to stem cell-derived islet-like clusters (SC-ILC) in a six-stage protocol. Stage 6 SC-ILC contain endocrine cells including insulin and NKX6.1 positive SC-β-cells and glucagon positive SC-α-cells. scale bar, 100µm. **b** SC-ILC were cultured in a 3D shaking culture. For glucose-stimulated insulin secretion assay (GSIS), SC-ILC were transferred to microcavities, and impedance spectra were recorded. Glucose concentrations were changed on the microcavity array (MCA)-chip. **c** Cross section scheme of a SC-ILC within a microcavity. The total impedance results from the sum of individual cells in the electric field, where each cell is characterized by its membrane capacity (C_{mem}) and membrane resistance (R_{mem}). Additionally, the measured impedance is impacted by the extracellular resistance (R_{EC}). **d** For impedimetric measurements a multielectrode MCA-chip with four attached cell chambers was used. Each cell chamber contains three measuring cavities. **e** Image of a microcavity either empty (upper image) or with a glass sphere symbolizing a 3D SC-ILC (lower image). Four gold electrodes are attached to each microcavity to allow impedimetric analysis. Adapted from Ref.[111,314] with permission of the authors represented by Dr. Heinz-Georg Jahnke.

To screen SC-ILC for their insulin secretion capacity, SC-ILC were starved in a low glucose buffer (2.8 mM) and the respective impedance was measured as a baseline. When increasing the buffer concentration to 20 mM glucose (high glucose), a decrease in impedance within the first 10 min was detected followed by a slow increase back to baseline levels. Since the differentiation efficiency varies between batches, but also between islets of the same batch, differences in insulin secretion capacity are to be expected. Accordingly, we observed variations in the relative change in impedance between different SC-ILC (**Figure 19**, a). To confirm that the detected impedance changes were consistent with insulin secretion, the supernatants of the MCA chip were analyzed. It is important to note that only the supernatant of all twelve SC-ILC could be measured collectively, as the medium reservoir was connected across all twelve cavities. In all samples, an increase in the insulin stimulation index in 20mM

glucose was observed. Again, differences in insulin secretion were visible, reflecting the observations from the impedance measurements (**Figure 19**, b). The insulin stimulation index and the change in relative impedance showed a high correlation (Pearson's coefficient: 0.93), confirming that the insulin stimulation index was reflected by the change in impedance (**Figure 19**, c). Additionally, the measured impedance spectra reflected published insulin secretion curves of a dynamic GSIS in progression and timing[85]. It can therefore be postulated that impedance spectroscopy can be used to monitor insulin secretion from SC-ILC in real-time.

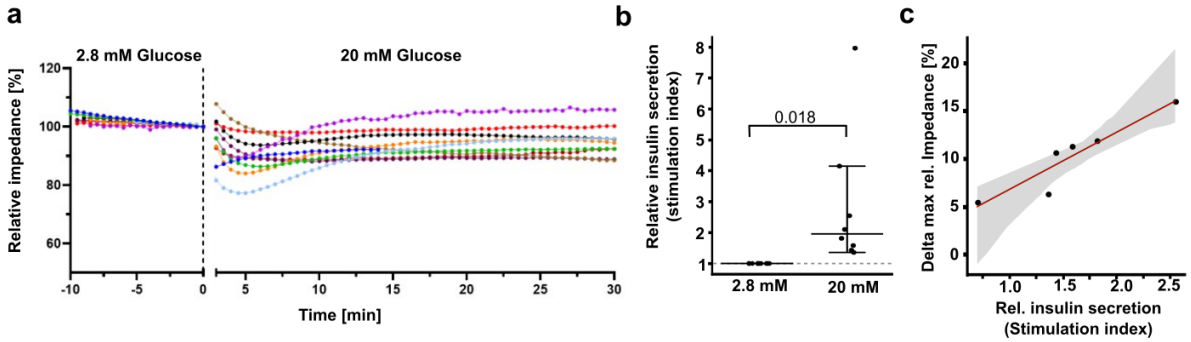

Figure 19: Glucose stimulated insulin secretion assay measured by impedance spectroscopy. a Change in impedance was measured at 2.8 mM glucose as a baseline before changing to 20 mM glucose (timepoint zero). Relative impedance spectra show the response of single SC-ILC to a high glucose challenge (20 mM). n = 10. As the change in buffer concentration led to short-term disturbances in the recording, the measurement in 20 mM glucose was started after 2 min (interrupted x-axis). **b** Supernatant analysis of SC-ILC cultured in one microcavity chip representing 8-11 SC-ILC. Insulin concentration was measured with an ultra-sensitive insulin ELISA kit and stimulation indices are depicted in the figure. n = 9. Statistical analysis by students t-test, *p-value* is depicted in the figure. **c** Correlation analysis of measured insulin secretion (stimulation index) to relative impedance showing a Pearson correlation coefficient of 0.93. One datapoint represents the mean of one experiment. n = 6. Outliers were removed when indicated in the python package seaborn-boxplot.

Impedimetric screening of SC-ILC response to Ca^{2+} -influx inhibitor diazoxide

We believe that impedance spectroscopy can be used for drug screening of SC-ILC in real time. To test this, SC-ILC were treated with the Ca^{2+}-influx inhibitor diazoxide and their impedimetric response was monitored. In a β-cell, glucose-mediated insulin secretion is caused by glucose oxidation, leading to an increase in the ATP to ADP ratio. This results in a closure of ATP-sensitive potassium channels (K_{ATP}), followed by a membrane depolarization and the influx of Ca^{2+} through voltage-gated calcium channels. The increase of intracellular Ca^{2+} concentration triggers the exocytosis of insulin granules. Diazoxide activates K_{ATP} channels, inhibiting Ca^{2+}-influx into the β-cell and glucose-mediated insulin secretion[66,316]. When treating the SC-ILC with Diazoxide, an increase in the minimal relative impedance was observed and recorded spectra were near to baseline levels. When comparing the diazoxide

treated samples to an untreated control group, a significant difference in relative impedance could be observed. Here, untreated controls had a minimal relative impedance of 89.38 ± 2.64%, whereas treated samples were at 97.5 ± 0.75% (**Figure 20**, a, b). When comparing the relative impedance with the insulin stimulation indices, it was observed that the impedance measurements also correctly mapped SC-ILCs that did not respond to treatment (**Figure 20**, c marked with an asterisk). However, mean insulin stimulation index and relative impedance only weakly correlated (Pearson coefficient: 0.176). This was mainly because of one experiment, showing a high insulin stimulation index but only a weak change in relative impedance (**Figure 20**, c marked with an arrow). On closer examination of the sample group, we found that the impedance spectra of three SC-ILCs showed the expected response. In contrast, one SC-ILC did not react to the treatment with diazoxide (**Figure 20**, d). Due to the chip design, the analysis of the insulin supernatant could only be performed for the entire batch and not for individual SC-ILCs. Therefore, even a single secreting SC-ILC can falsify the analysis. We can, therefore, conclude that impedance spectroscopy analyzed SC-ILCs for their insulin secretion capacity more accurately than would be possible with traditional batch analysis of multiple islets.

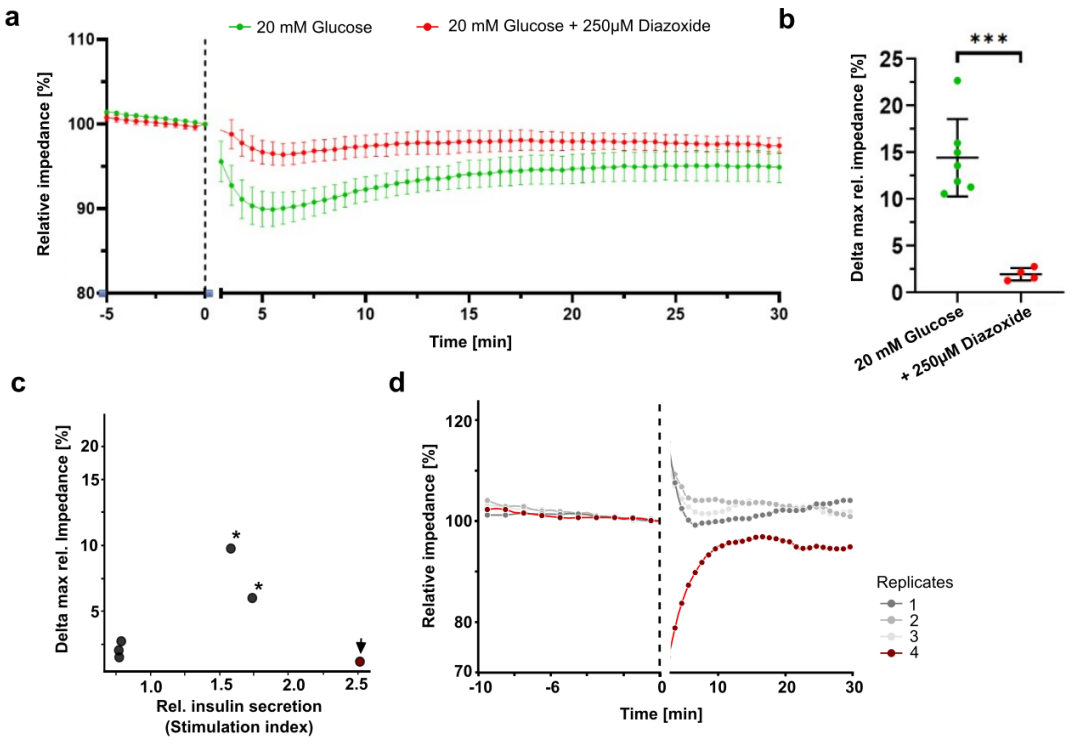

Figure 20: Determination of SC-ILC response to Ca^{2+}-influx inhibitor diazoxide. a Mean relative impedance of SC-ILC in high glucose (20 mM) or with a treatment of 250µM diazoxide to inhibit insulin secretion. The baseline was recorded in 2.8 mM glucose and is depicted (5 minutes before timepoint zero). At timepoint zero buffer concentration was changed to 20mM glucose with or without diazoxide. n = 6. As the change in buffer concentration led to short-term disturbances in the recording, the measurement in 20 mM glucose was started after 2

min (interrupted x-axis). **b** Statistic analysis of the change of mean relative impedance of high glucose and diazoxide treatment. The maximal change to baseline levels was calculated for each experiment and plotted. For statistical test a student's t-test was performed. *** $p \leq 0.001$. **c** Correlation analysis shows weak correlation of impedance measurement and insulin secretion after diazoxide treatment. Insulin secretion is depicted as stimulation index and means of individual experiments are shown. Asterisks indicate two experiments correlating in high stimulation index and strong change of relative impedance. Arrow indicates one outlier that will be considered further in d. **d** Impedance spectra of one experiment (marked with arrow in c) showing the variance in response of 4 single SC-ILC to a treatment with diazoxide. Red curve indicates a responsive SC-ILC although treated with diazoxide.

5.5 Discussion

In this study, we demonstrate that impedance spectroscopy can be used to monitor insulin secretion of SC-ILC in real-time. Therefore, an MCA-chip, we previously published[314], was used to measure the changes in impedance of single SC-ILC. With the MCA-chip used, it was possible to monitor up to twelve SC-ILC simultaneously. For the study, the measurement protocol on the MCA chip was adapted, including establishing a protocol for changing the GSIS buffer conditions without disturbing the SC-ILC in the microcavities (see Methods). We demonstrate that the SC-ILC could be adjusted to baseline in a low glucose buffer (2.8 mM) before changing the buffer concentration to high glucose (20 mM). At high glucose, the impedance change was monitored in real-time and a response curve similar to traditional dynamic GSIS curves was observed (**Figure 19**, a). In perfusion GSIS assays, islets typically respond with increased insulin secretion within the first 10 minutes when exposed to high glucose. Thereafter, insulin secretion falls back to baseline within 30 to 40 minutes via plateauing [85]. We show that this response could be measured with impedance spectroscopy and that the change in impedance also reflected the insulin secretion curve over time. In contrast to dynamic GSIS, we were able to measure this at the single aggregate level, whereas traditional GSIS require the use of up to 100 SC-ILC to record one response curve[317]. This opens up new possibilities for screening assays, as with this technique 100 SC-ILCs could also provide 100 individual results. Thus, the costs of expensive cell material could be reduced, and the use of ELISAs could be replaced.

As an example of possible drug screenings with impedance spectroscopy, SC-ILC were treated with diazoxide and their response was measured (**Figure 20**). We show that diazoxide inhibited insulin secretion from SC-ILC, which was reflected in only marginal changes in impedance. In particular, by measuring individual SC-ILC, outliers could be identified that distorted the result of the insulin ELISA in the batch analysis. We were thereby able to show

that impedance spectroscopy is suitable for screening individual SC-ILCs and thus achieved more accurate results than with traditional GSIS assays that rely on batch analyses.

In particular, the screening of multiple drugs is conceivable in the future, requiring larger MCA chips for higher throughput. We have recently published a 96-well plate MCA chip[112] that offers the possibility for high-throughput screening and will be used in future studies. A limitation of this study is that SC-ILCs exhibit high variability in their ability to secrete insulin. This can be explained by the differences in differentiation efficiency. In addition, off-target products are formed during differentiation, which further influence the efficiency[65]. Purification methods[242] for purer SC-β- and SC-α-cell populations would therefore be advantageous to achieve more uniform results, which would also reduce the number of replicates needed for future screening experiments. Overall, the impedance spectroscopy on the MCA-chip has proven its applicability for the screening of insulin secretion by SC-ILC in real time. In the future, this method could therefore be used to screen for mature SC-ILC or to test compounds for SC-ILC maturation, thus improving differentiation protocols. This brings us one step further to a high-throughput analysis of *in vitro* generated islets for drug development, diabetes research and therapy.

6 Conclusion and Outlook

The vascular system is of central importance for all organ functions and endothelial dysfunction is associated with many diseases, such as diabetes. With the increasing number of diabetes cases worldwide, there is a need to develop alternative treatment options and understand islet and endothelial biology and dysfunction better. This work therefore focused on β-cell and endothelial cell (EC) biology, which was addressed in three interconnected research projects.

To study the vascular system and early onset of metabolic damage to ECs better, scalable Organ-on-Chip (OoC) models are needed that allow the deep characterization of the engineered tissue in a more physiologic environment. In this thesis, a microfluidic vessel-on-chip was developed and used for a multiomic characterization of stem cell-derived ECs (SC-ECs). The 3D-printed chip allowed for fast prototyping and production, and the open design enabled the easy extraction of cell material for downstream analysis. By using a rock shaker to induce gravity-driven flow, a physiological shear stress could be generated, while at the same time the parallel cultivation of many chips was enabled, which allowed upscaling. In contrast to other OoC models, this enabled the extraction of single cells from the OoC platform for single-cell RNA sequencing (scRNAseq) and proteome analysis. In addition, the use of SC-ECs can offer the possibility to study endothelial development, tissue-specific toning, or patient-specific backgrounds in OoC models. However, most of the current vessels-on-chip use primary EC cell lines and it is unclear how SC-ECs will develop on-chip. The OoC platform developed in this work enabled the cultivation of SC-ECs in an organotypic microchannel and, to my knowledge, for the first time their in-depth characterization with scRNAseq, proteome and secretome analysis on-chip. The detailed characterization revealed a flow-induced maturation of SC-ECs towards an arterial phenotype as well as an increased nitric oxide (NO) secretion - an important hallmark of functional ECs. In addition, functional readouts and high-resolution imaging showed that SC-derived EC vessel structures recapitulated vascular barrier integrity and sprouting angiogenesis. Using an atherosclerosis model it was shown that the vessel-on-chip is suitable for investigating the effects of metabolic diseases on vascular function. Proteome and secretome analysis revealed early onset of metabolic stress induced by either oxidized low-density lipoprotein (oxLDL) or free fatty acids (FFA) treatment. In addition to the multiomic analysis, functional assays and imaging confirmed early endothelial dysfunction such as an altered NO synthesis, reactive oxygen species (ROS) production, and the accumulation of lipids within the SC-ECs. Beyond current vessels-on-chip this thesis therefore achieved i) the development of a scalable SC-derived vessel-on-chip; ii) the maturation of SC-ECs validated on a functional and single-cell transcriptomic level; iii) the

modeling of early endothelial dysfunction in atherosclerosis within SC-ECs; and iv) the multiomics analysis of SC-derived vessels in a healthy state and under metabolic stress.

In the future, the vessel-on-chip could offer the possibility to study diabetes-related endothelial dysfunction in more detail. In diabetes, chronic hyperglycemia, hyperinsulinemia, and insulin resistance can cause vascular dysfunction and cardiovascular diseases such as diabetic cardiomyopathy[318], atherosclerosis, or retinopathy[33,319]. Additionally, the metabolic activity of ECs is altered, resulting, for example, in increased glucose uptake by ECs[318]. Previous organoid studies with SC-ECs from diabetic and non-diabetic patients, revealed that diabetic SC-ECs show altered angiogenesis, and are more prone to oxidative stress and inflammation[320]. The culture of diabetic SC-ECs or the treatment of SC-ECs with high glucose concentrations on the vessel-on-chip could therefore help to obtain more detailed information about early endothelial dysfunction in diabetes. In addition, the communication of ECs and smooth muscle cells (SMCs) is altered in diabetes, as has been shown before[321]. However, early biomarkers are missing to detect changes in EC and SMC functionality and crosstalk. Here, co-seeding of SMCs and ECs can be used to mimic *in vivo* vessels more closely helping to study SMC and EC crosstalk in health and vascular diseases. In addition, the further upscaling of the vessel-on-chip platform could help to produce more conditions simultaneously and enable the platform for robust biomarker and drug screening (ongoing patent process). In the future, the general design of the OoC platform could enable the cultivation of other epithelial cell types and thus open up possibilities for other research questions, such as the design of an exocrine ductal epithelium on the chip.

In the second project, a vascularization model of stem cell-derived islet-like clusters (SC-ILC) was established *in vitro*. As the vascular system and the interaction of ECs and endocrine cells are essential for islet function and maturation, the *in vitro* vascularization could help to mature SC-ILC (which are still of an immature phenotype *in vitro*), enhance our knowledge about EC and endocrine communication, and improve transplantation outcome. Thus, this thesis aimed to vascularize SC-ILC and investigate its effect on endocrine function. As current vascularization models mainly use primary EC lines for islet vascularization, this thesis aimed to use SC-ECs to study tissue-specific toning, allow patient-specific research, or the engineering of autologous transplants in the future. Therefore, a vascularized co-culture (vCo-culture) was established, and the functional and transcriptional changes were analyzed. Within the vCo-culture, SC-β-cells showed a significant increase in function evaluated by insulin secretion, while their transcriptomic profile appeared unchanged in comparison to controls. While most research focuses on β-cell function, little is known about other cells of the islet niche, including α-cells and ECs. ScRNAseq analyses revealed that SC-ECs upregulated angiogenesis-associated genes and adopted an islet-EC tone. In addition, transcriptional

maturation of SC-α-cells occurred. Glucagon secretion assays confirmed the functional maturation of SC-α-cells in the 3D environment, emphasizing the importance of the *in vitro* generated microenvironment for the function of all islet cells. Using the acquired scRNAseq data, this thesis aimed to study SC-ECs and endocrine crosstalk within the vCo-culture. The most prominent interaction was observed between SC-β-cells and SC-ECs, including communication pathways influencing angiogenesis, migration, and β-cell function. This emphasizes that both cell types are important for each other's function and that a directed communication could be observed within the vCo-culture. In summary, this thesis i) established a stem cell-derived vascularization model for SC-ILC; ii) showed an improved functional maturation of SC-β- and SC-α-cells; iii) resolved transcriptional changes in the *in vitro* model; and iv) identified a directed cell-cell communication between SC-ECs and endocrine cells that could influence SC-β- and SC-α-cell functionality.

In the future, the established vCo-culture may help to investigate the interaction between SC-EC and endocrine cells in diabetes. Further, the identified interaction pathways could be tested for their role in SC-ILC maturation using compound tests. In addition, patient-derived iPSC lines could be used to reveal how the interaction of ECs and endocrine cells is altered in diabetes and to identify patient-specific differences. Further, the induction of a flow system is promising for increasing SC-EC function within the vCo-culture and enabling long-term cultivation. This can contribute to improving the overall health of the *in vitro* system. For example, Jun et al[40] have shown that a dynamic microfluidic culture increases viability and function in human islets. The most intuitive flow induction approach would be transferring the vCo-culture to the established vessel-on-chip platform. However, the first attempts were not successful because the hydrogel was not stable enough and the lumen collapsed over time. Here, adapting the hydrogel composition is a decisive step to enable long-term culture on the vessel-on-chip. In addition, transplantation studies could be initiated to test the vCo-culture for its use in cell replacement therapy. Also here, the hydrogel composition will need further adaption to good manufacturing practice (GMP) standards.

The third project focused on the analytical screening of SC-ILCs to i) replace expensive insulin ELISAs; ii) screen for mature SC-ILC; and iii) establish an alternative method for future drug screening in diabetes research. To achieve those aims, impedance spectroscopy was used to measure the impedimetric changes in SC-ILC caused by insulin secretion. The impedance spectra correlated with the measured insulin concentration from the supernatant, indicating that impedance spectroscopy was suitable for monitoring insulin secretion. A microcavity array (MCA) chip was used to analyze differences in insulin secretion from individual SC-ILCs that batch analysis cannot reflect. Thus, impedance spectroscopy offers the possibility for label-free detection of insulin secretion, which can reduce the analytical costs of current secretion

assays and enable high-throughput screening of SC-ILC. Screening of SC-ILC is particularly relevant as current differentiation protocols produce heterogeneous, immature islet populations. High-throughput screening of SC-ILC could therefore be used to improve differentiation protocols and test compounds for SC-ILC maturation. To achieve this, the MCA chip could be scaled up to a 96-well plate format in the future, which would also enable drug testing. In this context, the use of SC-ILC from diabetic patients could offer the possibility of patient-specific drug tests. In addition, MCA-based impedance spectroscopy can monitor 3D cultures over a longer period. Here, long-term treatments on the MCA chip would be interesting in investigating stress factors on SC-ILC. As the *in vitro* culture of SC-ILC requires shear stress[40], induction of a microfluidic system on the MCA chip could also be considered to extend the time SC-ILC can be cultured in the chip setup. Impedance spectroscopy is also of interest for use in OoC platforms. Transepithelial/endothelial electrical resistance (TEER) is a common method for analyzing barrier tissue integrity[322]. Especially in endothelial research, TEER measurements are used to investigate the endothelial barrier. Impedance spectroscopy can be used as a technique to determine the TEER. By integrating measuring electrodes into the vessel-on-chip system, an OoC system could, therefore, be developed in which the endothelial barrier can be measured live and over a longer period of time. This would enable the simple evaluation of the endothelial barrier on the vessel-on-chip.

In summary, this doctoral thesis has investigated various aspects of islet and endothelial biology. The stem cell-derived *in vitro* models go one step further toward physiological 3D models and show an improved replication of the *in vivo* microenvironment of islets and vascular vessels, which helps to reduce animal experiments. In addition, all three projects can be combined in the future to further investigate islet and endothelial biology in health and diabetes.

7 References

1. Pugsley, M. K. & Tabrizchi, R. The vascular system: An overview of structure and function. *J Pharmacol Toxicol Methods* **44**, 333–340 (2000).
2. Ricard, N., Bailly, S., Guignabert, C. & Simons, M. The quiescent endothelium: signalling pathways regulating organ-specific endothelial normalcy. *Nature Reviews Cardiology 2021 18:8* **18**, 565–580 (2021).
3. Trimm, E. & Red-Horse, K. Vascular endothelial cell development and diversity. *Nature Reviews Cardiology 2022 20:3* **20**, 197–210 (2022).
4. Mandrycky, C. J., Howard, C. C., Rayner, S. G., Shin, Y. J. & Zheng, Y. Organ-on-a-chip systems for vascular biology. *J Mol Cell Cardiol* **159**, 1–13 (2021).
5. Vascular Wall Shear Stress: Basic Principles and Methods | Enhanced Reader.
6. Polacheck, W. J., Kutys, M. L., Tefft, J. B. & Chen, C. S. Microfabricated blood vessels for modeling the vascular transport barrier. *Nat Protoc* **14**, 1425–1454 (2019).
7. Gerecht-Nir, S. *et al.* Vascular Development in Early Human Embryos and in Teratomas Derived from Human Embryonic Stem Cells. *Biol Reprod* **71**, 2029–2036 (2004).
8. Classification & Structure of Blood Vessels | SEER Training. https://training.seer.cancer.gov/anatomy/cardiovascular/blood/classification.html.
9. Senger, D. R. & Davis, G. E. Angiogenesis. *Cold Spring Harb Perspect Biol* **3**, a005090 (2011).
10. Tahergorabi, Z. & Khazaei, M. A Review on Angiogenesis and Its Assays. *Iran J Basic Med Sci* **15**, 1110 (2012).
11. Adair, T. H. & Montani, J.-P. Angiogenesis. *Colloquium Series on Integrated Systems Physiology: From Molecule to Function* **2**, 1–84 (2010).
12. Weber, C. & Noels, H. Atherosclerosis: current pathogenesis and therapeutic options. *Nat Med* **17**, 1410–1422 (2011).
13. Cardiovascular diseases. https://www.who.int/health-topics/cardiovascular-diseases#tab=tab_1.
14. Dubois-deruy, E., Peugnet, V., Turkieh, A. & Pinet, F. Oxidative Stress in Cardiovascular Diseases. *Antioxidants 2020, Vol. 9, Page 864* **9**, 864 (2020).
15. Falk, E. Pathogenesis of Atherosclerosis. *J Am Coll Cardiol* **47**, (2006).
16. Björkegren, J. L. M. & Lusis, A. J. Atherosclerosis: Recent developments. *Cell* **185**, 1630–1645 (2022).
17. Xu, S. *et al.* Endothelial Dysfunction in Atherosclerotic Cardiovascular Diseases and Beyond: From Mechanism to Pharmacotherapies. *Pharmacol Rev* **73**, 924–967 (2021).
18. Marder, M. *et al.* Stem cell-derived vessels-on-chip for cardiovascular disease modeling. *Cell Rep* **43**, (2024).

19. von Scheidt, M. *et al.* Applications and Limitations of Mouse Models for Understanding Human Atherosclerosis. *Cell Metab* **25**, 248–261 (2017).

20. van Berlo, D., van de Steeg, E., Amirabadi, H. E. & Masereeuw, R. The potential of multi-organ-on-chip models for assessment of drug disposition as alternative to animal testing. *Curr Opin Toxicol* **27**, 8–17 (2021).

21. Laschke, M. W. & Menger, M. D. Life is 3D: Boosting Spheroid Function for Tissue Engineering. *Trends Biotechnol* **35**, 133–144 (2017).

22. George, B., Shirure, V. S., Hughes, C. C. W. & George, S. C. Engineering Vascularized Organoid-on-a-Chip Models. 141–167 (2021).

23. Seo, H., Son, J. & Park, J.-K. Controlled 3D co-culture of beta cells and endothelial cells in a micropatterned collagen sheet for reproducible construction of an improved pancreatic pseudo-tissue. *APL Bioeng* **4**, 046103 (2020).

24. Riopel, M., Trinder, M. & Wang, R. Fibrin, a scaffold material for islet transplantation and pancreatic endocrine tissue engineering. *Tissue Eng Part B Rev* **21**, 34–44 (2015).

25. Maji, S. & Lee, H. Engineering Hydrogels for the Development of Three-Dimensional In Vitro Models. *International Journal of Molecular Sciences 2022, Vol. 23, Page 2662* **23**, 2662 (2022).

26. Bhatia, S. N. & Ingber, D. E. Microfluidic organs-on-chips. *Nature Biotechnology* vol. 32 760–772 Preprint at https://doi.org/10.1038/nbt.2989 (2014).

27. Zhang, S., Wan, Z. & Kamm, R. D. Vascularized organoids on a chip: strategies for engineering organoids with functional vasculature. *Lab Chip* **21**, 473–488 (2021).

28. Salewskij, K. & Penninger, J. M. Blood Vessel Organoids for Development and Disease. *Circ Res* **132**, 498–510 (2023).

29. Noonan, J. *et al.* A novel triple-cell two-dimensional model to study immune vascular interplay in atherosclerosis. *Front Immunol* **10**, 440551 (2019).

30. Shakeri, A. *et al.* Engineering Organ-on-a-Chip Systems for Vascular Diseases. *Arterioscler Thromb Vasc Biol* **43**, 2241–2255 (2023).

31. Rosowski, S. *et al.* Single-cell characterization of neovascularization using hiPSC-derived endothelial cells in a 3D microenvironment. *Stem Cell Reports* **18**, 1972–1986 (2023).

32. Wimmer, R. A., Leopoldi, A., Aichinger, M., Kerjaschki, D. & Penninger, J. M. Generation of blood vessel organoids from human pluripotent stem cells. *Nature Protocols 2019 14:11* **14**, 3082–3100 (2019).

33. Wimmer, R. A. *et al.* Human blood vessel organoids as a model of diabetic vasculopathy. *Nature* **565**, 505–510 (2019).

34. Patsch, C. *et al.* Generation of vascular endothelial and smooth muscle cells from human pluripotent stem cells. *Nat Cell Biol* **17**, 994–1003 (2015).

35. Jin, W. & Jiang, W. Stepwise differentiation of functional pancreatic β cells from human pluripotent stem cells. *Cell Regeneration* **11**, 24 (2022).

36. Ho, B. X., Pek, N. M. Q. & Soh, B. S. Disease Modeling Using 3D Organoids Derived from Human Induced Pluripotent Stem Cells. *Int J Mol Sci* **19**, (2018).

37. Jun, Y. *et al.* Engineered vasculature induces functional maturation of pluripotent stem cell-derived islet organoids. 1–47 (2022).

38. Jochems, P. G. M. *et al.* Development and validation of bioengineered intestinal tubules for translational research aimed at safety and efficacy testing of drugs and nutrients. *Toxicology in Vitro* **60**, 1–11 (2019).

39. Homan, K. A. *et al.* Flow-enhanced vascularization and maturation of kidney organoids in vitro. *Nature Methods 2019 16:3* **16**, 255–262 (2019).

40. Jun, Y. *et al.* In vivo–mimicking microfluidic perfusion culture of pancreatic islet spheroids. *Sci Adv* **5**, (2019).

41. Bender, R. H. F. *et al.* A vascularized 3D model of the human pancreatic islet for ex vivo study of immune cell-islet interaction. *Biofabrication* **16**, (2024).

42. Quintard, C. *et al.* A microfluidic platform integrating functional vascularized organoids-on-chip. *Nat Commun* **15**, (2024).

43. Phan, D. T. T. *et al.* A vascularized and perfused organ-on-a-chip platform for large-scale drug screening applications. *Lab Chip* **17**, 511–520 (2017).

44. Wu, Y., Zhou, Y., Qin, X. & Liu, Y. From cell spheroids to vascularized cancer organoids: Microfluidic tumor-on-a-chip models for preclinical drug evaluations. *Biomicrofluidics* **15**, 61503 (2021).

45. Singh, D., Mathur, A., Arora, S., Roy, S. & Mahindroo, N. Journey of organ on a chip technology and its role in future healthcare scenario. *Applied Surface Science Advances* **9**, 100246 (2022).

46. Leung, C. M. *et al.* A guide to the organ-on-a-chip. *Nature Reviews Methods Primers 2022 2:1* **2**, 1–29 (2022).

47. Srivastava, S. K., Foo, G. W., Aggarwal, N. & Chang, M. W. Organ-on-chip technology: Opportunities and challenges. *Biotechnology Notes* **5**, 8–12 (2024).

48. Kim, D. *et al.* Vascularized lung cancer model for evaluating the promoted transport of anticancer drugs and immune cells in an engineered tumor microenvironment. *Adv Healthc Mater* 2102581 (2022) doi:10.1002/adhm.202102581.

49. Lee, S. R. *et al.* U-IMPACT: a universal 3D microfluidic cell culture platform. *Microsyst Nanoeng* **8**, (2022).

50. Arslan, U. *et al.* Vascularized hiPSC-derived 3D cardiac microtissue on chip. *Stem Cell Reports* **18**, 1394–1404 (2023).

51. Lee, S. *et al.* Angiogenesis-on-a-chip coupled with single-cell RNA sequencing reveals spatially differential activations of autophagy along angiogenic sprouts. *Nature Communications 2024 15:1* **15**, 1–17 (2024).

52. Palikuqi, B. *et al.* Adaptable haemodynamic endothelial cells for organogenesis and tumorigenesis. *Nature* **585**, 1–7 (2020).

53. Maurissen, T. L. *et al.* Modeling early pathophysiological phenotypes of diabetic retinopathy in a human inner blood-retinal barrier-on-a-chip. *Nature Communications 2024 15:1* **15**, 1–13 (2024).

54. Su, C. *et al.* A novel human arterial wall-on-a-chip to study endothelial inflammation and vascular smooth muscle cell migration in early atherosclerosis. *Lab Chip* **21**, 2359–2371 (2021).

55. Zhang, X. *et al.* Modeling early stage atherosclerosis in a primary human vascular microphysiological system. *Nature Communications 2020 11:1* **11**, 1–17 (2020).

56. Li, Y. *et al.* Diabetic vascular diseases: molecular mechanisms and therapeutic strategies. *Signal Transduction and Targeted Therapy 2023 8:1* **8**, 1–29 (2023).

57. Whitcomb, D. C. & Lowe, M. E. Human Pancreatic Digestive Enzymes. *Digestive Diseases and Sciences 2006 52:1* **52**, 1–17 (2007).

58. Jennings, R. E., Berry, A. A., Strutt, J. P., Gerrard, D. T. & Hanley, N. A. Human pancreas development. (2015) doi:10.1242/dev.120063.

59. Dolenšek, J., Rupnik, M. S. & Stožer, A. Structural similarities and differences between the human and the mouse pancreas. *Islets* **7**, (2015).

60. Pan, F. C. & Brissova, M. Pancreas development in humans. *Curr Opin Endocrinol Diabetes Obes* **21**, 77 (2014).

61. Zorn, A. M. & Wells, J. M. Vertebrate Endoderm Development and Organ Formation. *https://doi.org/10.1146/annurev.cellbio.042308.113344* **25**, 221–251 (2009).

62. Yu, X. *et al.* Defining multistep cell fate decision pathways during pancreatic development at single-cell resolution. *EMBO J* **38**, (2019).

63. Bastidas-Ponce, A., Scheibner, K., Lickert, H. & Bakhti, M. Cellular and molecular mechanisms coordinating pancreas development. *Development* **144**, 2873–2888 (2017).

64. Engineering a microwell duct-on-chip technology to translate exocrine pancreatic organoids to a cancer model | Enhanced Reader.

65. Siehler, J., Blöchinger, A. K., Meier, M. & Lickert, H. Engineering islets from stem cells for advanced therapies of diabetes. *Nat Rev Drug Discov* **20**, 920–940 (2021).

66. Campbell, J. E. & Newgard, C. B. Mechanisms controlling pancreatic islet cell function in insulin secretion. *Nature Reviews Molecular Cell Biology* vol. 22 142–158 Preprint at https://doi.org/10.1038/s41580-020-00317-7 (2021).

67. Rix, I., Nexøe-Larsen, C., Bergmann, N. C., Lund, A. & Knop, F. K. Glucagon Physiology. *Can J Diabetes* **34**, 187–188 (2019).

68. Hogan, M. F. & Hull, R. L. The islet endothelial cell: a novel contributor to beta cell secretory dysfunction in diabetes. *Diabetologia* **60**, 952–959 (2017).

69. Olsson, R. & Carlsson, P. O. The pancreatic islet endothelial cell: Emerging roles in islet function and disease. *Int J Biochem Cell Biol* **38**, 710–714 (2006).

70. Narayanan, S. *et al.* Intra-islet endothelial cell and β-cell crosstalk: Implication for islet cell transplantation. *World J Transplant* **7**, 117 (2017).

71. IDF Diabetes Atlas 2021 | IDF Diabetes Atlas. https://diabetesatlas.org/atlas/tenth-edition/.

72. Artasensi A, Pedretti A, Vistoli G & Fumagalli L. Type 2 diabetes mellitus: A review of multi-target drugs. Molecules [revista en Internet] 2020 [acceso 7 de marzo de 2022]; 25(8): 1-20. 1–20 (2020).

73. Cho, N. H. *et al.* IDF Diabetes Atlas: Global estimates of diabetes prevalence for 2017 and projections for 2045. *Diabetes Res Clin Pract* **138**, 271–281 (2018).

74. Kharroubi, A. T. Diabetes mellitus: The epidemic of the century. *World J Diabetes* **6**, 850 (2015).

75. Wan, X. X. *et al.* Stem Cell Transplantation in the Treatment of Type 1 Diabetes Mellitus: From Insulin Replacement to Beta-Cell Replacement. *Front Endocrinol (Lausanne)* **13**, (2022).

76. Cudini, A. & Fierabracci, A. Advances in Immunotherapeutic Approaches to Type 1 Diabetes. *Int J Mol Sci* **24**, (2023).

77. Rapini, N., Schiaffini, R. & Fierabracci, A. Immunotherapy Strategies for the Prevention and Treatment of Distinct Stages of Type 1 Diabetes: An Overview. *Int J Mol Sci* **21**, (2020).

78. Herold, K. C. *et al.* An Anti-CD3 Antibody, Teplizumab, in Relatives at Risk for Type 1 Diabetes. *New England Journal of Medicine* **381**, 603–613 (2019).

79. Kioulaphides, S. & García, A. J. Encapsulation and immune protection for type 1 diabetes cell therapy. *Adv Drug Deliv Rev* 115205 (2024) doi:10.1016/J.ADDR.2024.115205.

80. Brennan, D. C. *et al.* Long-Term Follow-Up of the Edmonton Protocol of Islet Transplantation in the United States. *American Journal of Transplantation* **16**, 509–517 (2016).

81. Berney, T. *et al.* Long-Term Insulin-Independence After Allogeneic Islet Transplantation for Type 1 Diabetes: Over the 10-Year Mark. *American Journal of Transplantation* **9**, 419–423 (2009).

82. The Edmonton Protocol Turns 20: What Have We Learned? : 2018 Reports : Archives Reports : Report Library : Publications : Juvenile Diabetes Cure Alliance (JDCA). https://www.thejdca.org/publications/report-library/archived-reports/2018-reports/the-edmonton-protocol-turns-20-what-have-we-learned.html.

83. Hogrebe, N. J., Augsornworawat, P., Maxwell, K. G., Velazco-Cruz, L. & Millman, J. R. Targeting the cytoskeleton to direct pancreatic differentiation of human pluripotent stem cells. *Nat Biotechnol* **38**, 460–470 (2020).

84. Nakamura, A. *et al.* Long-term feeder-free culture of human pancreatic progenitors on fibronectin or matrix-free polymer potentiates β cell differentiation. *Stem Cell Reports* **17**, 1–14 (2022).

85. Velazco-Cruz, L. *et al.* Acquisition of Dynamic Function in Human Stem Cell-Derived β Cells. *Stem Cell Reports* **12**, 351–365 (2019).

86. Rezania, A. *et al.* Reversal of diabetes with insulin-producing cells derived in vitro from human pluripotent stem cells. *Nat Biotechnol* **32**, 1121–1133 (2014).

87. Zhu, H. *et al.* Understanding cell fate acquisition in stem-cell-derived pancreatic islets using single-cell multiome-inferred regulomes. *Dev Cell* **58**, 727-743.e11 (2023).

88. Augsornworawat, P., Maxwell, K. G., Velazco-Cruz, L. & Millman, J. R. Single-Cell Transcriptome Profiling Reveals β Cell Maturation in Stem Cell-Derived Islets after Transplantation. *Cell Rep* **32**, 108067 (2020).

89. Leite, N. C., Pelayo, G. C. & Melton, D. A. Genetic manipulation of stress pathways can protect stem-cell-derived islets from apoptosis in vitro. *Stem Cell Reports* **17**, (2022).

90. Leite, N. C. *et al.* Modeling Type 1 Diabetes In Vitro Using Human Pluripotent Stem Cells In Brief ll Modeling Type 1 Diabetes In Vitro Using Human Pluripotent Stem Cells. *Cell Rep* **32**, (2020).

91. Millman, J. R. *et al.* Generation of stem cell-derived β-cells from patients with type 1 diabetes. *Nat Commun* **7**, (2016).

92. Sackett, S. D. *et al.* Genetic Engineering of Immune Evasive Stem Cell-Derived Islets. *Transplant International* **35**, (2022).

93. Hu, X. *et al.* Human hypoimmune primary pancreatic islets avoid rejection and autoimmunity and alleviate diabetes in allogeneic humanized mice. *Sci Transl Med* **15**, (2023).

94. Wang, X. *et al.* Engineered immunomodulatory accessory cells improve experimental allogeneic islet transplantation without immunosuppression. *Sci Adv* **8**, 1–17 (2022).

95. Shapiro, A. M. J. & Verhoeff, K. A spectacular year for islet and stem cell transplantation. *Nat Rev Endocrinol* **19**, 2022–2023 (2022).

96. Ramzy, A. *et al.* Implanted pluripotent stem-cell-derived pancreatic endoderm cells secrete glucose-responsive C-peptide in patients with type 1 diabetes. *Cell Stem Cell* **28**, 2047-2061.e5 (2021).

97. Luciana Mateus Gonç alves, A. *et al.* Pericyte dysfunction and impaired vasomotion are hallmarks of islets during the pathogenesis of type 1 diabetes. *CellReports* **42**, 112913 (2023).

98. Quizon, M. J. Engineering β Cell Replacement Therapies for Type 1 Diabetes: Biomaterial Advances and Considerations for Macroscale Constructs. *Annu Rev Pathol* **2**, 485–513.

99. Aghazadeh, Y. *et al.* Microvessels support engraftment and functionality of human islets and hESC-derived pancreatic progenitors in diabetes models. *Cell Stem Cell* **28**, 1936-1949.e8 (2021).

100. Wrublewsky, S. *et al.* Co-transplantation of pancreatic islets and microvascular fragments effectively restores normoglycemia in diabetic mice. 1–10 doi:10.1038/s41536-022-00262-3.

101. Takahashi, Y., Sekine, K., Kin, T., Takebe, T. & Taniguchi, H. Self-Condensation Culture Enables Vascularization of Tissue Fragments for Efficient Therapeutic Transplantation. *Cell Rep* **23**, 1620–1629 (2018).

102. Weaver, J. D. *et al.* Synthetic poly(ethylene glycol)-based microfluidic islet encapsulation reduces graft volume for delivery to highly vascularized and retrievable transplant site. *American Journal of Transplantation* **19**, 1315–1327 (2019).

103. Hugh F. Bender1, Benjamen T. O'Donnell1, Bhupinder Shergill2, Brittany Q. Pham1, Damie J. Juat1, Michaela S. Hatch1, Venktesh S. Shirure2, Matthew Wortham3, Kim-Vy Nguyen-Ngoc3, Yesl Jun3, Roberto Gaetani5, Karen L. Christman5, Luc Teyton6, Steven C. Geor, C. C. W. H. A vascularized 3D model of the human pancreatic islet for. **8771**, (2021).

104. Chen, C. H. *et al.* In vivo immune modulatory activity of hepatic stellate cells in mice. *Hepatology* **44**, 1171–1181 (2006).

105. Ito, T. *et al.* Mesenchymal stem cell and islet co-transplantation promotes graft revascularization and function. *Transplantation* **89**, 1438–1445 (2010).

106. Wang, K. *et al.* The paracrine effects of adipose-derived stem cells on neovascularization and biocompatibility of a macroencapsulation device. *Acta Biomater* **15**, 65–76 (2015).

107. De León, S. E., Pupovac, A. & McArthur, S. L. Three-Dimensional (3D) cell culture monitoring: Opportunities and challenges for impedance spectroscopy. *Biotechnol Bioeng* **117**, 1230–1240 (2020).

108. Xiao, X. *et al.* In-situ monitoring of breast cancer cell (MCF-7) growth and quantification of the cytotoxicity of anticancer drugs fluorouracil and cisplatin. *Biosens Bioelectron* **24**, 247–252 (2008).

109. Han, A., Yang, L. & Frazier, A. B. Quantification of the heterogeneity in breast cancer cell lines using whole-cell impedance spectroscopy. *Clin Cancer Res* **13**, 139–143 (2007).

110. Szulcek, R., Bogaard, H. J. & van Nieuw Amerongen, G. P. Electric Cell-substrate Impedance Sensing for the Quantification of Endothelial Proliferation, Barrier Function, and Motility. *J Vis Exp* **85**, 51300 (2014).

111. Jahnke, H. G. *et al.* Direct chemosensitivity monitoring ex vivo on undissociated melanoma tumor tissue by impedance spectroscopy. *Cancer Res* **74**, 6408–6418 (2014).

112. Zitzmann, F. D. *et al.* Microcavity well-plate for automated parallel bioelectronic analysis of 3D cell cultures. *Biosens Bioelectron* **250**, 116042 (2024).

113. Gerasimenko, T. *et al.* Impedance Spectroscopy as a Tool for Monitoring Performance in 3D Models of Epithelial Tissues. *Front Bioeng Biotechnol* **7**, 503370 (2020).

114. Li, W. hong. Functional analysis of islet cells in vitro, in situ, and in vivo. *Semin Cell Dev Biol* **103**, 14 (2020).

115. Sakamoto, S. *et al.* Enzyme-linked immunosorbent assay for the quantitative/qualitative analysis of plant secondary metabolites. *J Nat Med* **72**, 32 (2018).

116. Kalwat, M. & Cobb, M. H. Measuring relative insulin secretion using a co-secreted luciferase surrogate. *J Vis Exp* **2019**, (2019).

117. Balboa, D. *et al.* Functional, metabolic and transcriptional maturation of human pancreatic islets derived from stem cells. *Nat Biotechnol* (2022) doi:10.1038/s41587-022-01219-z.

118. Hwang, B., Lee, J. H. & Bang, D. Single-cell RNA sequencing technologies and bioinformatics pipelines. *Experimental & Molecular Medicine 2018 50:8* **50**, 1–14 (2018).

119. Tang, F. *et al.* mRNA-Seq whole-transcriptome analysis of a single cell. *Nature Methods 2009 6:5* **6**, 377–382 (2009).

120. Utada, A. S. *et al.* Monodisperse double emulsions generated from a microcapillary device. *Science* **308**, 537–541 (2005).

121. Slovin, S. *et al.* Single-Cell RNA Sequencing Analysis: A Step-by-Step Overview. *Methods in Molecular Biology* **2284**, 343–365 (2021).

122. Aebersold, R. & Mann, M. Mass spectrometry-based proteomics. *Nature 2003 422:6928* **422**, 198–207 (2003).

123. Shuken, S. R. An Introduction to Mass Spectrometry-Based Proteomics. *J Proteome Res* **22**, 2151–2171 (2023).

124. Im, K., Mareninov, S., Diaz, M. F. P. & Yong, W. H. An introduction to Performing Immunofluorescence Staining. *Methods Mol Biol* **1897**, 299 (2019).

125. Kane, R. S., Stroock, A. D., Li Jeon, N., Ingber, D. E. & Whitesides, G. M. Soft Lithography and Microfluidics. *Optical Biosensors* 571–595 (2002) doi:10.1016/B978-044450974-1/50018-5.

126. Macdonald, N. P. *et al.* Comparing Microfluidic Performance of Three-Dimensional (3D) Printing Platforms. *Anal Chem* **89**, 3858–3866 (2017).

127. Bhattacharjee, N., Urrios, A., Kang, S. & Folch, A. The upcoming 3D-printing revolution in microfluidics. *Lab Chip* **16**, 1720–1742 (2016).

128. Song, Y., Ghafari, Y., Asefnejad, A. & Toghraie, D. An overview of selective laser sintering 3D printing technology for biomedical and sports device applications: Processes, materials, and applications. *Opt Laser Technol* **171**, 110459 (2024).

129. Chen, C. *et al.* 3D-printed microfluidic devices: fabrication, advantages and limitations—a mini review. *Analytical Methods* **8**, 6005–6012 (2016).

130. Patsch, C. *et al.* Generation of vascular endothelial and smooth muscle cells from human pluripotent stem cells. *Nat Cell Biol* **17**, 994–1003 (2015).

131. Kennedy, C. C., Brown, E. E., Abutaleb, N. O. & Truskey, G. A. Development and Application of Endothelial Cells Derived From Pluripotent Stem Cells in Microphysiological Systems Models. *Front Cardiovasc Med* **8**, (2021).

132. Vila Cuenca, M. *et al.* Engineered 3D vessel-on-chip using hiPSC-derived endothelial- and vascular smooth muscle cells. *Stem Cell Reports* **16**, 1–10 (2021).

133. Cochrane, A. *et al.* Advanced in vitro models of vascular biology: Human induced pluripotent stem cells and organ-on-chip technology. *Adv Drug Deliv Rev* **140**, 68–77 (2019).

134. Williams, I. M. & Wu, J. C. Generation of Endothelial Cells From Human Pluripotent Stem Cells. *Arterioscler Thromb Vasc Biol* **39**, 1317–1329 (2019).

135. Helle, E., Ampuja, M., Antola, L. & Kivelä, R. Flow-Induced Transcriptomic Remodeling of Endothelial Cells Derived From Human Induced Pluripotent Stem Cells. *Front Physiol* **11**, (2020).

136. Campinho, P., Vilfan, A. & Vermot, J. Blood Flow Forces in Shaping the Vascular System: A Focus on Endothelial Cell Behavior. *Front Physiol* **11**, (2020).

137. Nguyen, D. H. T. *et al.* Biomimetic model to reconstitute angiogenic sprouting morphogenesis in vitro. *Proc Natl Acad Sci U S A* **110**, 6712–6717 (2013).

138. Hajal, C. *et al.* Engineered human blood–brain barrier microfluidic model for vascular permeability analyses. *Nature Protocols 2021 17:1* **17**, 95–128 (2022).

139. Trietsch, S. J., Israëls, G. D., Joore, J., Hankemeier, T. & Vulto, P. Microfluidic titer plate for stratified 3D cell culture. *Lab Chip* **13**, 3548–3554 (2013).

140. Zhang, X. *et al.* Modeling early stage atherosclerosis in a primary human vascular microphysiological system. *Nat Commun* **11**, 5426 (2020).

141. Madamanchi, N. R., Vendrov, A. & Runge, M. S. Oxidative stress and vascular disease. *Arterioscler Thromb Vasc Biol* **25**, 29–38 (2005).

142. Ghosh, A., Gao, L., Thakur, A., Siu, P. M. & Lai, C. W. K. Role of free fatty acids in endothelial dysfunction. *J Biomed Sci* **24**, 50 (2017).

143. Zhang, W.-Y. *et al.* Elevated Concentrations of Nonesterified Fatty Acids Increase Monocyte Expression of CD11b and Adhesion to Endothelial Cells. *Arterioscler Thromb Vasc Biol* **26**, 514–519 (2006).

144. Olmer, R. *et al.* Differentiation of Human Pluripotent Stem Cells into Functional Endothelial Cells in Scalable Suspension Culture. *Stem Cell Reports* **10**, 1657–1672 (2018).

145. Compera, N., Atwell, S., Wirth, J., Wolfrum, B. & Meier, M. Upscaling of pneumatic membrane valves for the integration of 3D cell cultures on chip. *Lab Chip* **21**, 2986–2996 (2021).

146. Tinevez, J. Y. *et al.* TrackMate: An open and extensible platform for single-particle tracking. *Methods* **115**, 80–90 (2017).

147. Poon, C. Measuring the density and viscosity of culture media for optimized computational fluid dynamics analysis of in vitro devices. *J Mech Behav Biomed Mater* **126**, 105024 (2022).

148. Schmidt, U., Weigert, M., Broaddus, C. & Myers, G. Cell Detection with Star-convex Polygons. in vol. 11071 265–273 (2018).

149. Wolf, F. A., Angerer, P. & Theis, F. J. SCANPY: large-scale single-cell gene expression data analysis. *Genome Biol* **19**, (2018).

150. Wolock, S. L., Lopez, R. & Klein, A. M. Scrublet: Computational Identification of Cell Doublets in Single-Cell Transcriptomic Data. *Cell Syst* **8**, 281-291.e9 (2019).

151. Traag, V. A., Waltman, L. & van Eck, N. J. From Louvain to Leiden: guaranteeing well-connected communities. *Sci Rep* **9**, 5233 (2019).

152. McInnes, L., Healy, J., Saul, N. & Großberger, L. UMAP: Uniform Manifold Approximation and Projection. *J Open Source Softw* **3**, 861 (2018).

153. Bergen, V., Lange, M., Peidli, S., Wolf, F. A. & Theis, F. J. Generalizing RNA velocity to transient cell states through dynamical modeling. *Nat Biotechnol* **38**, 1408–1414 (2020).

154. La Manno, G. *et al.* RNA velocity of single cells. *Nature* **560**, 494–498 (2018).

155. Bondareva, O. *et al.* Single-cell profiling of vascular endothelial cells reveals progressive organ-specific vulnerabilities during obesity. *Nat Metab* **4**, 1591–1610 (2022).

156. Abdelmagid, S. A. *et al.* Comprehensive profiling of plasma fatty acid concentrations in young healthy Canadian adults. *PLoS One* **10**, e0116195 (2015).

157. Compera, N. *et al.* Adipose microtissue-on-chip: a 3D cell culture platform for differentiation, stimulation, and proteomic analysis of human adipocytes. *Lab Chip* **22**, 3172–3186 (2022).

158. Hladik, D. *et al.* CREB Signaling Mediates Dose-Dependent Radiation Response in the Murine Hippocampus Two Years after Total Body Exposure. *J Proteome Res* **19**, 337–345 (2020).

159. Navarro, P. *et al.* General Statistical Framework for Quantitative Proteomics by Stable Isotope Labeling. *J Proteome Res* **13**, 1234–1247 (2014).

160. Uhlén, M. *et al.* The human secretome. *Sci Signal* **12**, eaaz0274 (2019).

161. Szklarczyk, D. *et al.* STRING v10: protein-protein interaction networks, integrated over the tree of life. *Nucleic Acids Res* **43**, D447-452 (2015).

162. Raudvere, U. *et al.* g:Profiler: a web server for functional enrichment analysis and conversions of gene lists (2019 update). *Nucleic Acids Res* **47**, W191–W198 (2019).

163. Kuleshov, M. V *et al.* Enrichr: a comprehensive gene set enrichment analysis web server 2016 update. *Nucleic Acids Res* **44**, W90-97 (2016).

164. Wirth, J. *et al.* Spatial transcriptomics using multiplexed deterministic barcoding in tissue. *Nature Communications 2023 14:1* **14**, 1–15 (2023).

165. Virtanen, P. *et al.* SciPy 1.0: fundamental algorithms for scientific computing in Python. *Nature Methods 2020 17:3* **17**, 261–272 (2020).

166. Roux, E., Bougaran, P., Dufourcq, P. & Couffinhal, T. Fluid Shear Stress Sensing by the Endothelial Layer. *Front Physiol* **11**, (2020).

167. Rhodes, J. M. & Simons, M. The extracellular matrix and blood vessel formation: not just a scaffold. *J Cell Mol Med* **11**, 176–205 (2007).

168. Traag, V. A., Waltman, L. & van Eck, N. J. From Louvain to Leiden: guaranteeing well-connected communities. *Sci Rep* **9**, 5233 (2019).

169. McInnes, L., Healy, J., Saul, N. & Großberger, L. UMAP: Uniform Manifold Approximation and Projection. *J Open Source Softw* **3**, 861 (2018).

170. Muhl, L. *et al.* Single-cell analysis uncovers fibroblast heterogeneity and criteria for fibroblast and mural cell identification and discrimination. *Nat Commun* **11**, 3953 (2020).

171. McCracken, I. R. *et al.* Transcriptional dynamics of pluripotent stem cell-derived endothelial cell differentiation revealed by single-cell RNA sequencing. *Eur Heart J* **41**, 1024–1036 (2020).

172. Dekker, R. J. *et al.* Endothelial KLF2 Links Local Arterial Shear Stress Levels to the Expression of Vascular Tone-Regulating Genes. *Am J Pathol* **167**, 609–618 (2005).

173. Bae, Y. S., Oh, H., Rhee, S. G. & Yoo, Y. Do. Regulation of reactive oxygen species generation in cell signaling. *Mol Cells* **32**, 491–509 (2011).

174. Galbusera, M. *et al.* Fluid shear stress modulates von Willebrand factor release from human vascular endothelium. *Blood* **90**, 1558–1564 (1997).

175. Fang, J. S. *et al.* Shear-induced Notch-Cx37-p27 axis arrests endothelial cell cycle to enable arterial specification. *Nat Commun* **8**, 2149 (2017).

176. McCracken, I. R. *et al.* Mapping the developing human cardiac endothelium at single-cell resolution identifies MECOM as a regulator of arteriovenous gene expression. *Cardiovasc Res* **118**, 2960–2972 (2022).

177. Magid, R., Murphy, T. J. & Galis, Z. S. Expression of matrix metalloproteinase-9 in endothelial cells is differentially regulated by shear stress. Role of c-Myc. *J Biol Chem* **278**, 32994–32999 (2003).

178. Morancho, A. *et al.* Impaired Vascular Remodeling after Endothelial Progenitor Cell Transplantation in MMP9-Deficient Mice Suffering Cortical Cerebral Ischemia. *Journal of Cerebral Blood Flow & Metabolism* **35**, 1547–1551 (2015).

179. Morawietz, H., Wagner, A. H., Hecker, M. & Goettsch, W. Endothelin receptor B-mediated induction of c-jun and AP-1 in response to shear stress in human endothelial cells. *Can J Physiol Pharmacol* **86**, 499–504 (2008).

180. Ferrari, G., Cook, B. D., Terushkin, V., Pintucci, G. & Mignatti, P. Transforming growth factor-beta 1 (TGF-beta1) induces angiogenesis through vascular endothelial growth factor (VEGF)-mediated apoptosis. *J Cell Physiol* **219**, 449–458 (2009).

181. Klemke, R. L. Abstract 1811: A PEAK1/GATA2 signaling axis controls VEGFR2 expression to mediate angiogenesis. *Cancer Res* **77**, 1811 (2017).

182. Hautefort, A., Pfenniger, A. & Kwak, B. R. Endothelial connexins in vascular function. *Vascular Biology* **1**, H117–H124 (2019).

183. Wettschureck, N., Strilic, B. & Offermanns, S. Passing the Vascular Barrier: Endothelial Signaling Processes Controlling Extravasation. *Physiol Rev* **99**, 1467–1525 (2019).

184. Bergen, V., Lange, M., Peidli, S., Wolf, F. A. & Theis, F. J. Generalizing RNA velocity to transient cell states through dynamical modeling. *Nat Biotechnol* **38**, 1408–1414 (2020).

185. Zeng, Y. *et al.* Tracing the first hematopoietic stem cell generation in human embryo by single-cell RNA sequencing. *Cell Res* **29**, 881–894 (2019).

186. CONSORTIUM, T. H. E. T. S. The Tabula Sapiens: A multiple-organ, single-cell transcriptomic atlas of humans. *Science (1979)* **376**, eabl4896 (2022).

187. Schilling, K. *et al.* Translocation of Endothelial Nitric-Oxide Synthase Involves a Ternary Complex with Caveolin-1 and NOSTRIN. *Mol Biol Cell* **17**, 3870–3880 (2006).

188. Murthy, S. *et al.* Endothelial CaMKII as a regulator of eNOS activity and NO-mediated vasoreactivity. *PLoS One* **12**, e0186311 (2017).

189. Taha, A. A., Taha, M., Seebach, J. & Schnittler, H.-J. ARP2/3-mediated junction-associated lamellipodia control VE-cadherin–based cell junction dynamics and maintain monolayer integrity. *Mol Biol Cell* **25**, 245–256 (2014).

190. Poznyak, A. V *et al.* Overview of OxLDL and Its Impact on Cardiovascular Health: Focus on Atherosclerosis. *Front Pharmacol* **11**, (2021).

191. Ghosh, A., Gao, L., Thakur, A., Siu, P. M. & Lai, C. W. K. Role of free fatty acids in endothelial dysfunction. *J Biomed Sci* **24**, 50 (2017).

192. Wang, Y. L., Hui, Y. N., Guo, B. & Ma, J. X. Strengthening tight junctions of retinal microvascular endothelial cells by pericytes under normoxia and hypoxia involving angiopoietin-1 signal way. *Eye (Lond)* **21**, 1501–1510 (2007).

193. Duvigneau, J. C., Esterbauer, H. & Kozlov, A. V. Role of Heme Oxygenase as a Modulator of Heme-Mediated Pathways. *Antioxidants* **8**, 475 (2019).

194. Rogero, M. M. & Calder, P. C. Obesity, Inflammation, Toll-Like Receptor 4 and Fatty Acids. *Nutrients* **10**, 432 (2018).

195. Luo, W. *et al.* Heme oxygenase-1 ameliorates oxidative stress-induced endothelial senescence via regulating endothelial nitric oxide synthase activation and coupling. *Aging* **10**, 1722–1744 (2018).

196. Di Pietro, P. *et al.* Sortilin evokes endothelial dysfunction and arterial hypertension through the dysregulation of sphingolipid metabolism and oxidative stress. *Eur Heart J* **41**, ehaa946.2704 (2020).

197. Uhlén, M. *et al.* The human secretome. *Sci Signal* **12**, eaaz0274 (2019).

198. Sangwung, P. *et al.* KLF2 and KLF4 control endothelial identity and vascular integrity. *JCI Insight* **2**, e91700 (2017).

199. Lundberg, J. O. & Weitzberg, E. Nitric oxide signaling in health and disease. *Cell* **185**, 2853–2878 (2022).

200. Jiang, H. *et al.* Mechanisms of Oxidized LDL-Mediated Endothelial Dysfunction and Its Consequences for the Development of Atherosclerosis. *Front Cardiovasc Med* **9**, 925923 (2022).

201. López-Novoa, J. M. & Bernabeu, C. The physiological role of endoglin in the cardiovascular system. *American Journal of Physiology-Heart and Circulatory Physiology* **299**, H959–H974 (2010).

202. Lilly, B. *et al.* Endothelial cell-induced cytoglobin expression in vascular smooth muscle cells contributes to modulation of nitric oxide. *Vascul Pharmacol* **110**, 7–15 (2018).

203. Liu, B. & Dai, Z. Fatty Acid Metabolism in Endothelial Cell. *Genes (Basel)* **13**, 2301 (2022).

204. Ekmekçi, Ö. B. & Ekmekçi, H. Vitronectin in atherosclerotic disease. *Clinica Chimica Acta* **368**, 77–83 (2006).

205. Yaghoubi, A., Ghojazadeh, M., Abolhasani, S., Alikhah, H. & Khaki-Khatibi, F. Correlation of Serum Levels of Vitronectin, Malondialdehyde and Hs- CRP With Disease Severity in Coronary Artery Disease. *J Cardiovasc Thorac Res* **7**, 113–117 (2015).

206. Wang, Y. I. & Shuler, M. L. UniChip enables long-term recirculating unidirectional perfusion with gravity-driven flow for microphysiological systems. *Lab Chip* **18**, 2563–2574 (2018).

207. Da Silva Xavier, G. The Cells of the Islets of Langerhans. *J Clin Med* **7**, 54 (2018).

208. Almaça, J., Caicedo, A. & Landsman, L. Beta cell dysfunction in diabetes: the islet microenvironment as an unusual suspect. *Diabetologia 2020 63:10* **63**, 2076–2085 (2020).

209. Brissova, M. *et al.* Human Islets Have Fewer Blood Vessels than Mouse Islets and the Density of Islet Vascular Structures Is Increased in Type 2 Diabetes. *Journal of Histochemistry and Cytochemistry* **63**, 637–645 (2015).

210. Jonsson, A., Hedin, A., Müller, M., Skog, O. & Korsgren, O. Transcriptional profiles of human islet and exocrine endothelial cells in subjects with or without impaired glucose metabolism. *Sci Rep* **10**, 1–11 (2020).

211. Johansson, M., Mattsson, G., Andersson, A., Jansson, L. & Carlsson, P. O. Islet Endothelial Cells and Pancreatic β-Cell Proliferation: Studies in Vitro and during Pregnancy in Adult Rats. *Endocrinology* **147**, 2315–2324 (2006).

212. Staels, W., Heremans, Y., Heimberg, H. & De Leu, N. VEGF-A and blood vessels: a beta cell perspective. *Diabetologia* **62**, 1961–1968 (2019).

213. Cayabyab, F., Nih, L. R. & Yoshihara, E. Advances in Pancreatic Islet Transplantation Sites for the Treatment of Diabetes. *Front Endocrinol (Lausanne)* **12**, 732431 (2021).

214. Schauer, P. R. *et al.* Bariatric Surgery versus Intensive Medical Therapy in Obese Patients with Diabetes. *New England Journal of Medicine* **366**, 1567–1576 (2012).

215. Sachs, S. *et al.* Targeted pharmacological therapy restores β-cell function for diabetes remission. *Nature Metabolism 2020 2:2* **2**, 192–209 (2020).

216. Shapiro, A. M. J. & Verhoeff, K. A spectacular year for islet and stem cell transplantation. *Nat Rev Endocrinol* **19**, 2022–2023 (2022).

217. Jin, W. & Jiang, W. Stepwise differentiation of functional pancreatic β cells from human pluripotent stem cells. *Cell Regeneration* **11**, 24 (2022).

218. Cayabyab, F., Nih, L. R. & Yoshihara, E. Advances in Pancreatic Islet Transplantation Sites for the Treatment of Diabetes. *Front Endocrinol (Lausanne)* **12**, 732431 (2021).

219. Arzouni, A. A. *et al.* Characterization of the Effects of Mesenchymal Stromal Cells on Mouse and Human Islet Function. *Stem Cells Transl Med* **8**, 935–944 (2019).

220. Wang, K. *et al.* The paracrine effects of adipose-derived stem cells on neovascularization and biocompatibility of a macroencapsulation device. *Acta Biomater* **15**, 65–76 (2015).

221. Gesmundo, I. *et al.* Adipocyte-derived extracellular vesicles regulate survival and function of pancreatic β cells. *JCI Insight* **6**, 1–17 (2021).

222. Peterson, Q. P. *et al.* A method for the generation of human stem cell-derived alpha cells. *Nat Commun* **11**, 1–14 (2020).

223. Siehler, J. *et al.* Generation of a heterozygous C-peptide-mCherry reporter human iPSC line (HMGUi001-A-8). *Stem Cell Res* **50**, (2021).

224. Patsch, C. *et al.* Generation of vascular endothelial and smooth muscle cells from human pluripotent stem cells. *Nat Cell Biol* **17**, 994–1003 (2015).

225. McGinnis, C. S., Murrow, L. M. & Gartner, Z. J. DoubletFinder: Doublet Detection in Single-Cell RNA Sequencing Data Using Artificial Nearest Neighbors. *Cell Syst* **8**, 329-337.e4 (2019).

226. Korsunsky, I. *et al.* Fast, sensitive and accurate integration of single-cell data with Harmony. *Nature Methods 2019 16:12* **16**, 1289–1296 (2019).

227. La Manno, G. *et al.* RNA velocity of single cells. *Nature 2018 560:7719* **560**, 494–498 (2018).

228. KEGG PATHWAY Database. https://www.genome.jp/kegg/pathway.html.

229. Fang, Z., Liu, X. & Peltz, G. GSEApy: a comprehensive package for performing gene set enrichment analysis in Python. *Bioinformatics* **39**, (2023).

230. Gene Ontology Resource. https://geneontology.org/.

231. Jin, S., Plikus, M. V. & Nie, Q. CellChat for systematic analysis of cell-cell communication from single-cell and spatially resolved transcriptomics. *bioRxiv* 2023.11.05.565674 (2023) doi:10.1101/2023.11.05.565674.

232. GitHub - jinworks/CellChat: R toolkit for inference, visualization and analysis of cell-cell communication from single-cell and spatially resolved transcriptomics. https://github.com/jinworks/CellChat?tab=readme-ov-file.

233. Hao, Y. *et al.* Dictionary learning for integrative, multimodal and scalable single-cell analysis. *Nat Biotechnol* **42**, 293–304 (2024).

234. GitHub - mojaveazure/seurat-disk: Interfaces for HDF5-based Single Cell File Formats. https://github.com/mojaveazure/seurat-disk.

235. Augsornworawat, P. *et al.* Single-nucleus multi-omics of human stem cell-derived islets identifies deficiencies in lineage specification. (2023) doi:10.1038/s41556-023-01150-8.

236. Veres, A. *et al.* Charting cellular identity during human in vitro β-cell differentiation. *Nature* **569**, 368–373 (2019).

237. Qadir, M. M. F. *et al.* Single-cell resolution analysis of the human pancreatic ductal progenitor cell niche. *Proc Natl Acad Sci U S A* **117**, 10876–10887 (2020).

238. Qadir, M. M. F. *et al.* Single-cell resolution analysis of the human pancreatic ductal progenitor cell niche. *Proc Natl Acad Sci U S A* **117**, 10876–10887 (2020).

239. Zeve, D. *et al.* Robust differentiation of human enteroendocrine cells from intestinal stem cells. *Nature Communications 2022 13:1* **13**, 1–20 (2022).

240. Veres, A. *et al.* Charting cellular identity during human in vitro β-cell differentiation. *Nature* **569**, 368–373 (2019).

241. Augsornworawat, P. *et al.* Single-nucleus multi-omics of human stem cell-derived islets identifies deficiencies in lineage specification. (2023) doi:10.1038/s41556-023-01150-8.

242. Mahaddalkar, P. U. *et al.* Generation of pancreatic β cells from CD177+ anterior definitive endoderm. *Nat Biotechnol* **38**, 1061–1072 (2020).

243. Kelly, O. G. *et al.* Cell-surface markers for the isolation of pancreatic cell types derived from human embryonic stem cells. *Nature Biotechnology 2011 29:8* **29**, 750–756 (2011).

244. Veres, A. *et al.* Charting cellular identity during human in vitro β-cell differentiation. *Nature* **569**, 368–373 (2019).

245. Hogan, M. F. & Hull, R. L. The islet endothelial cell: a novel contributor to beta cell secretory dysfunction in diabetes. *Diabetologia* **60**, 952–959 (2017).

246. Jin, S., Plikus, M. V. & Nie, Q. CellChat for systematic analysis of cell-cell communication from single-cell and spatially resolved transcriptomics. *bioRxiv* 2023.11.05.565674 (2023) doi:10.1101/2023.11.05.565674.

247. Sakhneny, L., Epshtein, A. & Landsman, L. Pericytes contribute to the islet basement membranes to promote beta-cell gene expression. *Sci Rep* **11**, 1–10 (2021).

248. Wieland, F. C., van Blitterswijk, C. A., van Apeldoorn, A. & LaPointe, V. L. S. The functional importance of the cellular and extracellular composition of the islets of Langerhans. *J Immunol Regen Med* **13**, 100048 (2021).

249. Schiesser, J. V., Loudovaris, T., Thomas, H. E., Elefanty, A. G. & Stanley, E. G. Integrin αvβ5 heterodimer is a specific marker of human pancreatic beta cells. *Scientific Reports 2021 11:1* **11**, 1–8 (2021).

250. Krishnamurthy, M., Li, J., Al-Masri, M. & Wang, R. Expression and function of αβ1 integrins in pancretic beta (INS-1) cells. *J Cell Commun Signal* **2**, 67 (2008).

251. Aamodt, K. I. & Powers, A. C. Signals in the pancreatic islet microenvironment influence β-cell proliferation. *Diabetes Obes Metab* **19**, 124–136 (2017).

252. Dunér, P. *et al.* Adhesion G protein-coupled receptor G1 (ADGRG1/GPR56) and pancreatic β-cell function. *Journal of Clinical Endocrinology and Metabolism* **101**, 4637–4645 (2016).

253. Sakhneny, L., Epshtein, A. & Landsman, L. Pericytes contribute to the islet basement membranes to promote beta-cell gene expression. *Sci Rep* **11**, 2378 (2021).

254. Brissova, M. *et al.* Pancreatic Islet Production of Vascular Endothelial Growth Factor-A Is Essential for Islet Vascularization, Revascularization, and Function. *Diabetes* **55**, 2974–2985 (2006).

255. Muramatsu, H. *et al.* α4β1- and α6β1-integrins are functional receptors for midkine, a heparin-binding growth factor. *J Cell Sci* **117**, 5405–5415 (2004).

256. Crouch, E. E. *et al.* Ensembles of endothelial and mural cells promote angiogenesis in prenatal human brain. (2022) doi:10.1016/j.cell.2022.09.004.

257. Huang, C.-C., Gung, C. & Hospital, M. Soluble delta-like 1 homolog (DLK1) stimulates angiogenesis through Notch1/Akt/eNOS signaling in endothelial cells. *Angiogenesis* (2018) doi:10.1007/s10456-018-9596-7.

258. Abdallah, B. M., Ditzel, N., Laborda, J., Karsenty, G. & Kassem, M. DLK1 Regulates Whole-Body Glucose Metabolism: A Negative Feedback Regulation of the Osteocalcin-Insulin Loop. *Diabetes* **64**, 3069–3080 (2015).

259. Ye, Z. *et al.* Wnt5a uses CD146 as a receptor to regulate cell motility and convergent extension. *Nature Communications 2013 4:1* **4**, 1–11 (2013).

260. Zielonka, M., Xia, J., Friedel, R. H., Offermanns, S. & Worzfeld, T. A systematic expression analysis implicates Plexin-B2 and its ligand Sema4C in the regulation of the vascular and endocrine system. *Exp Cell Res* **316**, 2477–2486 (2010).

261. Sadanandam, A., Rosenbaugh, E. G., Singh, S., Varney, M. & Singh, R. K. Semaphorin 5A promotes angiogenesis by increasing endothelial cell proliferation, migration, and decreasing apoptosis. *Microvasc Res* **79**, 1–9 (2010).

262. Waeber, G. *et al.* Insulin secretion is regulated by the glucose-dependent production of islet β cell macrophage migration inhibitory factor. *Proc Natl Acad Sci U S A* **94**, 4782 (1997).

263. Xu, W. *et al.* Islet Stellate Cells Regulate Insulin Secretion via Wnt5a in Min6 Cells. *Int J Endocrinol* **2020**, (2020).

264. Blondeau, N., Béraud-Dufour, S., Lebrun, P., Hivelin, C. & Coppola, T. Sortilin in glucose homeostasis: From accessory protein to key player? *Front Pharmacol* **9**, (2019).

265. Yang, Y. H. C., Manning Fox, J. E., Zhang, K. L., MacDonald, P. E. & Johnson, J. D. Intraislet SLIT-ROBO signaling is required for beta-cell survival and potentiates insulin secretion. *Proc Natl Acad Sci U S A* **110**, 16480–16485 (2013).

266. Nica, A. C. *et al.* Cell-type, allelic, and genetic signatures in the human pancreatic beta cell transcriptome. *Genome Res* **23**, 1554 (2013).

267. Chmielowiec, J. *et al.* Human pancreatic microenvironment promotes β-cell differentiation via non-canonical WNT5A/JNK and BMP signaling. *Nat Commun* **13**, (2022).

268. Duval, V., Alayrac, P., Silvestre, J. S. & Levoye, A. Emerging Roles of the Atypical Chemokine Receptor 3 (ACKR3) in Cardiovascular Diseases. *Front Endocrinol (Lausanne)* **13**, (2022).

269. Hay, D. L., Chen, S., Lutz, T. A., Parkes, D. G. & Roth, J. D. Amylin: Pharmacology, Physiology, and Clinical Potential. *Pharmacol Rev* **67**, 564–600 (2015).

270. Martínez, A., Kapas, S., Miller, M. J., Ward, Y. & Cuttitta, F. Coexpression of Receptors for Adrenomedullin, Calcitonin Gene-Related Peptide, and Amylin in Pancreatic β-Cells. *Endocrinology* **141**, 406–411 (2000).

271. Johansson, J. K. *et al.* N-cadherin is dispensable for pancreas development but required for β-cell granule turnover. *Genesis* **48**, 374 (2010).

272. Martínez, M. S. *et al.* The Role of the α Cell in the Pathogenesis of Diabetes: A World beyond the Mirror. *International Journal of Molecular Sciences 2021, Vol. 22, Page 9504* **22**, 9504 (2021).

273. Jain, R. & Lammert, E. Cell–cell interactions in the endocrine pancreas. *Diabetes Obes Metab* **11**, 159–167 (2009).

274. Bosi, E. *et al.* A single-cell human islet interactome atlas identifies disrupted autocrine and paracrine communications in type 2 diabetes. *NAR Genom Bioinform* **4**, (2022).

275. Francavilla, C. *et al.* The binding of NCAM to FGFR1 induces a specific cellular response mediated by receptor trafficking. *J Cell Biol* **187**, 1101 (2009).

276. Richards, M. *et al.* Claudin5 protects the peripheral endothelial barrier in an organ and vessel-type-specific manner. *Elife* **11**, (2022).

277. Kouklis, P., Konstantoulaki, M., Vogel, S., Broman, M. & Malik, A. B. Cdc42 Regulates the Restoration of Endothelial Barrier Function. *Circ Res* **94**, 159–166 (2004).

278. Lin, Z. *et al.* KLF2 regulates endothelial barrier function. *Arterioscler Thromb Vasc Biol* **30**, 1952 (2010).

279. Haasdijk, R. A. *et al.* THSD1 preserves vascular integrity and protects against intraplaque haemorrhaging in ApoE-/- mice. *Cardiovasc Res* **110**, 129–139 (2016).

280. Llacua, A., De Haan, B. J., Smink, A. M. & De Vos, P. Extracellular matrix components supporting human islet function in alginate-based immunoprotective microcapsules for treatment of diabetes. (2016) doi:10.1002/jbm.a.35706.

281. Yu, H. *et al.* LOXL1 confers antiapoptosis and promotes gliomagenesis through stabilizing BAG2. *Cell Death & Differentiation 2020 27:11* **27**, 3021–3036 (2020).

282. Santini-González, J. *et al.* In vitro generation of peri-islet basement membrane-like structures. *Biomaterials* **273**, 120808 (2021).

283. Papaccio, G., Pedull, M., Ammendola, E. & Todaro, M. Cytokine regulatory effects on α-1 proteinase inhibitor expression in NOD mouse islet endothelial cells. *J Cell Biochem* **85**, 123–130 (2002).

284. García-Ocaña, A. *et al.* Transgenic overexpression of hepatocyte growth factor in the beta-cell markedly improves islet function and islet transplant outcomes in mice. *Diabetes* **50**, 2752–2762 (2001).

285. Zanone, M. M. *et al.* Expression of nephrin by human pancreatic islet endothelial cells. *Diabetologia* **48**, 1789–1797 (2005).

286. Favara, D. M. *et al.* Elevated expression of the adhesion GPCR ADGRL4/ELTD1 promotes endothelial sprouting angiogenesis without activating canonical GPCR signalling. *Scientific Reports 2021 11:1* **11**, 1–13 (2021).

287. Zhu, T., Chen, H., He, C. & Liu, X. Transcription Factor HEY1 Improves Brain Vascular Endothelial Cell Function and Alleviates Ischemic Stroke by Upregulating NOTCH3. *Neurochem Res* **47**, 1442–1458 (2022).

288. Burganova, G., Bridges, C., Thorn, P. & Landsman, L. The Role of Vascular Cells in Pancreatic Beta-Cell Function. *Front Endocrinol (Lausanne)* **12**, 667170 (2021).

289. Zhang, H. hai *et al.* S-nitrosylation of Cofilin-1 Serves as a Novel Pathway for VEGF-Stimulated Endothelial Cell Migration. *J Cell Physiol* **230**, 406 (2015).

290. Leidi, M., Mariotti, M. & Maier, J. A. M. EDF-1 contributes to the regulation of nitric oxide release in VEGF-treated human endothelial cells. *Eur J Cell Biol* **89**, 654–660 (2010).

291. Okuda, K. S. & Hogan, B. M. Endothelial Cell Dynamics in Vascular Development: Insights From Live-Imaging in Zebrafish. *Front Physiol* **11**, 842 (2020).

292. Santiago-Sim, T. *et al.* THSD1 (Thrombospondin Type 1 Domain Containing Protein 1) Mutation in the Pathogenesis of Intracranial Aneurysm and Subarachnoid Hemorrhage. *Stroke* **47**, 3005–3013 (2016).

293. Ramracheya, R. *et al.* Membrane Potential-Dependent Inactivation of Voltage-Gated Ion Channels in α-Cells Inhibits Glucagon Secretion From Human Islets. *Diabetes* **59**, 2198–2208 (2010).

294. Zhang, B. *et al.* Role and mechanism of PI3K/AKT/FoxO1/PDX-1 signaling pathway in functional changes of pancreatic islets in rats after severe burns. *Life Sci* **258**, 118145 (2020).

295. Katsumoto, K. *et al.* Wnt4 is heterogeneously activated in maturing β-cells to control calcium signaling, metabolism and function. *Nat Commun* **13**, (2022).

296. Westenfelder, C. & Gooch, A. 3D Organoids of Mesenchymal Stromal and Pancreatic Islet Cells. *Pluripotent Stem Cell Therapy for Diabetes* 179–193 (2023) doi:10.1007/978-3-031-41943-0_9.

297. Moede, T., Leibiger, I. B. & Berggren, P. O. Alpha cell regulation of beta cell function. *Diabetologia* **63**, 2064–2075 (2020).

298. Jiang, G. & Zhang, B. B. Glucagon and regulation of glucose metabolism. *Am J Physiol Endocrinol Metab* **284**, (2003).

299. Siafarikas, A. *et al.* Early Loss of the Glucagon Response to Hypoglycemia in Adolescents With Type 1 Diabetes. *Diabetes Care* **35**, 1757–1762 (2012).

300. Parent, A. V. *et al.* Development of a scalable method to isolate subsets of stem cell-derived pancreatic islet cells. *Stem Cell Reports* **17**, (2022).

301. Kavand, H. *et al.* 3D-Printed Biohybrid Microstructures Enable Transplantation and Vascularization of Microtissues in the Anterior Chamber of the Eye. *Advanced Materials* **36**, 2306686 (2024).

302. Speier, S. *et al.* Noninvasive in vivo imaging of pancreatic islet cell biology. *Nature Medicine 2008 14:5* **14**, 574–578 (2008).

303. Citro, A. *et al.* Directed self-assembly of a xenogeneic vascularized endocrine pancreas for type 1 diabetes. *Nat Commun* **14**, (2023).

304. Aisenbrey, E. A. & Murphy, W. L. Synthetic alternatives to Matrigel. *Nature Reviews Materials* vol. 5 539–551 Preprint at https://doi.org/10.1038/s41578-020-0199-8 (2020).

305. Russell, R. *et al.* Loss of the transcription factor MAFB limits β-cell derivation from human PSCs. *Nature Communications 2020 11:1* **11**, 1–15 (2020).

306. Rosado-Olivieri, E. A., Aigha, I. I., Kenty, J. H., Melton Correspondence, D. A. & Melton, D. A. Identification of a LIF-Responsive, Replication-Competent Subpopulation of Human b Cells Cell Metabolism Identification of a LIF-Responsive, Replication-Competent Subpopulation of Human b Cells. *Cell Metab* **31**, 327–338 (2020).

307. Millman, J. R. *et al.* Generation of stem cell-derived β-cells from patients with type 1 diabetes. *Nat Commun* **7**, (2016).

308. Sintov, E. *et al.* Whole-genome CRISPR screening identifies genetic manipulations to reduce immune rejection of stem cell-derived islets. *Stem Cell Reports* **17**, 1976–1990 (2022).

309. Shang, L. *et al.* β-cell dysfunction due to increased ER stress in a stem cell model of Wolfram syndrome. *Diabetes* **63**, 923–933 (2014).

310. Amin, S. *et al.* Discovery of a drug candidate for GLIS3-associated diabetes. *Nat Commun* **9**, (2018).

311. Hrvatin, S. *et al.* Differentiated human stem cells resemble fetal, not adult, β cells. *Proc Natl Acad Sci U S A* **111**, 3038–3043 (2014).

312. Zhang, X., Ma, Z., Song, E. & Xu, T. Islet organoid as a promising model for diabetes. *Protein Cell* **13**, 239 (2022).

313. Burns, S. M. *et al.* High-Throughput Luminescent Reporter of Insulin Secretion for Discovering Regulators of Pancreatic Beta-Cell Function. *Cell Metab* **21**, 126–137 (2015).

314. Zitzmann, F. D. *et al.* Multielectrode biosensor chip for spatial resolution screening of 3D cell models based on microcavity arrays. *Biosens Bioelectron* **202**, 114010 (2022).

315. Paniccia, A. & Schulick, R. D. Pancreatic Physiology and Functional Assessment. *Blumgart's Surgery of the Liver, Biliary Tract and Pancreas: Sixth Edition* **1–2**, 66-76.e3 (2017).

316. Song, S. H., Rhodes, C. J., Veldhuis, J. D. & Butler, P. C. Diazoxide Attenuates Glucose-Induced Defects in First-Phase Insulin Release and Pulsatile Insulin Secretion in Human Islets. *Endocrinology* **144**, 3399–3405 (2003).

317. Alcazar, O. & Buchwald, P. Concentration-Dependency and Time Profile of Insulin Secretion: Dynamic Perifusion Studies With Human and Murine Islets. *Front Endocrinol (Lausanne)* **10**, 680 (2019).

318. Wang, M., Li, Y., Li, S. & Lv, J. Endothelial Dysfunction and Diabetic Cardiomyopathy. *Front Endocrinol (Lausanne)* **13**, 851941 (2022).

319. Handa, P. *et al.* Endothelial Dysfunction in Diabetes. *Biomedicines 2020, Vol. 8, Page 182* **8**, 182 (2020).

320. Naderi-Meshkin, H. *et al.* Impaired Function in Diabetic Patient iPSCs-derived Blood Vessel Organoids Stem from a Subpopulation of Vascular Cells. *bioRxiv* 2022.07.18.500478 (2022) doi:10.1101/2022.07.18.500478.

321. Warmke, N., Griffin, K. J. & Cubbon, R. M. Pericytes in diabetes-associated vascular disease. *J Diabetes Complications* **30**, 1643–1650 (2016).

322. Srinivasan, B. *et al.* TEER measurement techniques for in vitro barrier model systems. *J Lab Autom* **20**, 107 (2015).